FLUID GELS:
FORMATION, PRODUCTION AND LUBRICATION

By
Andrea Gabriele

A thesis submitted to
The University of Birmingham
for the degree of
DOCTOR OF PHILOSOPHY

Microstructure Group
Department of Chemical Engineering
College of Engineering and Physical Sciences
The University of Birmingham

April 2011

UNIVERSITY OF BIRMINGHAM

University of Birmingham Research Archive

e-theses repository

This unpublished thesis/dissertation is copyright of the author and/or third parties. The intellectual property rights of the author or third parties in respect of this work are as defined by The Copyright Designs and Patents Act 1988 or as modified by any successor legislation.

Any use made of information contained in this thesis/dissertation must be in accordance with that legislation and must be properly acknowledged. Further distribution or reproduction in any format is prohibited without the permission of the copyright holder.

Abstract

Gelation of hydrocolloids under shear conditions results in a weak gel which is capable of sustaining elastic mechanical deformation at small strains but which flows if subjected to higher deformations (fluid gels). I have investigated the formation, production and lubrication properties of fluid gels from the gelation of agarose and κ-carrageenan. The formation of fluid gels in a rheometer, using well-defined, flow patterns and cooling rates have been described. Under these conditions narrow particle size distributions were achieved by inducing spinodal decomposition. The increase in viscosity due to particles formation was found to be inversely proportional to the shear rate. The power law exponents describing this relationship are provided for several hydrocolloid concentrations. The studies on the formation of fluid gels from κ-carrageenan, showed that it was possible to form homogeneous particle size fluid gels with mean diameter smaller than 5 μm. The fluid gels produced showed strong and highly recoverable particle bridging. A model is presented for the kinetics of aggregation of these particles, providing information on the mechanisms involved.

The use of the pin stirrer heat exchanger was previously reported as the large-scale method for the production of agar fluid gels. However little work has been done in describing fluid dynamics, and specifically the shear rates. Positron Emission Particle Tracking (*PEPT*) was used to characterise flow phenomena occurring in a pin stirrer heat exchanger for a 1 *Pa s* glycerol solution and a 2% agar fluid gel. Internal recirculation paths and *axial*-occupancy show a compartmental behaviour, with the tracer selectively occupying specific areas. Analysis of particle paths revealed that for a rotational speed of 900 *rpm* the average shear rate experienced by a particle was approximately 200 s^{-1}. Areas of poor mixing in dead-zones

were also identified. These findings can contribute to a rational design of equipment and processes for industrial scale fluid gel production.

Bulk rheological properties of fluid gels are similar to emulsions used in a large number of applications in everyday food products and cosmetics (Brown, Cuttler *et al.*, 1990; Bialek, Jones *et al.*, 2000), in order to replace emulsions their lubrication behaviour should also be fully understood. In the proposed lubrication mechanism the agarose fluid gel micro particles under specific conditions of entrainment velocity U, normal load W and elasticity E, interact with the lubricating surfaces, resulting in a localised increase in friction. A wide range of agarose concentration was studied (1% to 4%) resulting in fluid gel particles having different values of elasticity E, ranging from 5 kPa to 140 kPa, which were shown to alter their tribological behaviour, modifying the critical velocity required to induce entrainment of the particles, U_{entr}. For an identical particle's elasticity, the critical velocity was found to decrease by 50% when the normal load was increased by 30%, while the opposite trend was observed when the normal load maintained constant. Fluid gel systems of the same elasticity E but of different particles sizes were also investigated. The maximum friction measured upon entrainment of the particles decreased from 0.3 to 0.2 when the average Sauter mean diameter of the particles passed from 102 μm to 83 μm.

In Memoria di Nonna Pia,

‘πάντα χωρεῖ καὶ οὐδὲν μένει’ | *‘Panta chōrei kai ouden menei’*

Everything flows, nothing stays still

- Heraclitus (535 BC - 475 BC)

Acknowledgements

I wish to acknowledge both my supervisors Professor Ian Norton and Doctor Fotis Spyropoulos for their invaluable support in the course of my research. In particular Ian for all his encouragements in perusing my aspirations and Fotis for his patience and friendship during these years.

A special thank also to Doctor Serafim Bakalis, for his assistance and help throughout the course of this project, but also for all the time spend discussing fluid dynamics, music and bicycle maintenance.

I am deeply grateful for the financial assistance of Unilever whom without this thesis would have not been possible. I am also grateful to the amazing people I met in the Unilever Research Centre in Trumbull, CT (USA), but especially Doctor Teanoosh Moaddel for his help and support.

My father, my mother for always pushing me to do what I believed I liked most and special thank you to my sister Eleonora, for her long distance cheering, and her too few visits. Marjan for her outstanding patience and invaluable presence, Nima and Hamza, for their friendship and for all the stimulating conversations. But also Fabio, Sarah, Dave, Giacomo, Antonio, Crea, Ciccio, Giorgio, Antonio, Walter, Luca and many more. The list of the friends that helped me in this journey is long, and I do apologise for those that have been unintentionally left out.

Table of Contents

LIST OF FIGURES ..... **III**

LIST OF TABLES ..... **VII**

CHAPTER 1. INTRODUCTION **1**
1.1. BACKGROUND 2
1.2. OBJECTIVES 4
1.3. THESIS STRUCTURE 5

CHAPTER 2. LITERATURE REVIEW **8**
2.1. INTRODUCTION 9
2.2. HYDROCOLLOIDS 9
2.2.1. Spinodal decomposition of metastable solutions *12*
2.2.2. Gelation induced by ionic activity: Carrageenans *13*
2.2.3. Biopolymers undergoing thermal gelation *20*
2.3. SHEARED GELATION OF BIOPOLYMERS SOLUTIONS: FLUID GELS 24
2.4. RHEOLOGICAL PROPERTIES AND THE SENSORY ATTRIBUTES PERCEIVED BY THE SKIN 29
2.4.1. Food Texture and Palatability *30*
2.4.2. Skin feeling and cosmetics *32*
2.5. FLUID DYNAMICS OF THE PIN STIRRER HEAT EXCHANGER 34
2.6. EXPERIMENTAL INVESTIGATIONS AND FLOW TECHNIQUES 35
2.6.1. Positron Emission Particle Tracking (PEPT) *36*
2.7. TRIBOLOGY 38
2.7.1. Elastohydrodynamic lubrication *39*
2.7.2. The lubricant properties *41*
2.7.3. Film thickness calculation *42*
2.7.4. The dynamic friction coefficient: Stribeck Curve *45*
2.7.5. Skin Lubrication and Tribology *46*

CHAPTER 3. EXPERIMENTAL **50**
3.1. INTRODUCTION 51
3.2. MATERIALS 51
3.2.1. Biopolymer solutions *51*
3.2.2. Glycerol *52*
3.2.3. Potassium Cloride *52*
3.3. METHODOLOGY 52
3.3.1. Kinetic studies of bio-polyelectrolyte fluid gels *53*
3.3.2. Positron Emitting Particle Tracking Experiment *58*
3.3.3. Tribology of agarose fluid gels *78*

CHAPTER 4. κ-CARRAGEENAN FLUID GELS **83**
4.1. INTRODUCTION 84
4.2. RESULTS AND DISCUSSION 84
4.3. EFFECT OF SHEAR RATE DURING FLUID GEL PRODUCTION 84
4.3.1. Effect of cooling rate during fluid gel production *92*
4.3.2. Particle interactions during and after production *94*
4.4. CONCLUSIONS 101

CHAPTER 5. A FLUID DYNAMIC INVESTIGATION OF FLUID GEL PRODUCTION 102
5.1. INTRODUCTION 103
5.2. RHEOLOGY OF PEPT FLUIDS 103
5.3. FLUID DYNAMIC INVESTIGATIONS 105
5.3.1. Particle Paths 105
5.3.2. Return Time Distributions 109
5.3.3. Azimuthally averaged velocity contour plots 116
5.3.4. Shear rates 126
5.3.5. Occupancy 130
5.3.6. Particle Shear Rate History 134
5.4. CONCLUSIONS 137

CHAPTER 6. A MODEL FOR FLUID GEL LUBRICATION 139
6.1. INTRODUCTION 140
6.2. FLUID GEL PARTICLE SIZES 140
6.3. FLUID GEL PARTICLE ELASTICITY AND RHEOLOGY 142
6.4. TRIBOLOGY OF FLUID GELS 144
6.4.1. Film thickness 146
6.4.2. The entrainment mechanism and entrainment velocity U_{entr} 148
6.5. PARTICLE SIZE EFFECT ON THE LUBRICATION 153
6.6. CONCLUSIONS 155

CHAPTER 7. CONCLUSIONS AND FUTURE RECOMMENDATIONS 156
7.1. CONCLUSIONS 157
7.1.1. Fluid gels from Bio-Polyelectrolytes 157
7.1.2. Fluid dynamic study of large scale fluid gel formation 159
7.1.3. Fluid gels Tribology 160

CHAPTER 8.REFERENCES: 162

APPENDIX I. MATLAB® SCRIPTS 179
AI.1 PEPT.M 178
AI.2. PLOAD.M 179
AI.3. ARRAYCREATOR.M 181
AI.4. MANCLEAN.M 181
AI.5. AUTO_CLEAN.M 182
AI.6. DIGITALCLEAN.M 183
AI.7. INTERP3PEPT.M 184
AI.8. EULO.M 186
AI.9. SHER_CALC.M 189

APPENDIX II. JOURNAL PUBLICATIONS 191

List of Figures

Figure 2.1: Primary $(A-B)_n$ structure of carrageenan. Adapted from Anderson, Dolan et al. (1968) 11

Figure 2.2: The two models for the conformational transition and aggregation in κ-carrageenan. In (a) the double helix conformation while in (b) is shown the single helix. (Paoletti, Smidsrod et al., 1984)..... 14

Figure 2.3: Variation of the melting temperature with the free potassium concentration C_T. (x) heating curve and (o) for the cooling curve (Rochas and Rinaudo 1980)..... 15

Figure 2.4: Variation of T_m obtained from optical rotation with the partial ionic volume of monovalent counter ions in excess of external salt ($[Cl^-]$ = 0.1 N). (Rochas and Rinaudo 1980) 17

Figure 2.5: The chemical structure of Agarose (Araki, 1956) 20

Figure 2.6: (a) Gelation of the chains of agarose (Armisen, Galatas et al., 2000) with the step $A \rightarrow B_1 \rightarrow C$ suggested by (Morris, Rees et al., 1980). While in (b), courtesy of (San Biagio, Bulone et al., 1996) the phase diagram of agarose with description of the different phenomena leading to gelation. (1) is a thermodynamically stable solution. (2)Freely drifting gelled regions, sample remains macroscopically liquid. (3) Spinodal promoted gel with mechanism described in the text. (4) Gel formed because of kinetic competition between demixing, conformational transition and cross-linking. 21

Figure 2.7: Storage modulus for agar fluid gel, prepared under different shear fields. (Norton, Frith et al., 2006)..... 26

Figure 2.8: Range of morphology and dimension of particles obtained by shearing mixtures of different biopolymers in solution and cooled below the gelation temperature (Wolf, Scirocco et al., 2000). 27

Figure 2.9: Set up of the C-unit within the detectors. In the extract, the nucleolus emits a positron, β^+, annihilated by an electron e^- present in the surrounding, producing the two back-to-back γ rays. 37

Figure 2.10: In the above sketch is shown the particular case of an elastic ball pressed with a load W against an un-deformable plane. The circular contact surface has radius a while δ, describes the deformation. ... 39

Figure 2.11: Subdivision of the EHL in 4 different regimes. IVR described by the line ACDB; PVE described by MLCQR, PVR described by ACLM and the remaining portion of the graph is IVE (Johnson, 1970). ... 43

Figure 2.12: Typical stribeck curve, where on the friction coefficient μ_F is represents a function of the Sommerfeld Number (see text). In the graph, three zones can be clearly identified. Zone I shows the boundary lubrication regime, for sliding surfaces in direct contact, lubrication is given by the surface properties. Zone II is known as mixed regime, in this zone, the hydraulic pressure separates the two surfaces, and the friction decreases. In Zone III, the sliding walls are fully separates, by the hydrodynamic pressure. The friction increases due to viscosity of the fluid. 45

Figure 2.13: Stribeck Curve obtained by sliding a glass probe on the inner skin of the arm. Normal load applied was 0.2 N. The different data sets represent the various liquid viscosities tested. All fluids were Newtonian (Adams, Briscoe et al., 2007)..... 47

Figure 3.1: Cone plate geometry with humidity trap limiting the evaporation..... 53

Figure 3.2: Raw rheological data and linear regressions to calculate the viscosity increase (Δη) between ordering initiation and completion during fluid gel production. 55

Figure 3.3: Mechanical drawing of the pin stirrer. Units are expressed in mm 58

Figure 3.4: Experimental set-up for the production of fluid gels with the pin stirrer heat exchanger.'TI' are the temperature indicator, while with 'FI' is indicated the flowmeter. 59

Figure 3.5: The pin stirrer within the PEPT cameras 62

Figure 3.6: Experimental activity of the tracer through-out the glycerol experiment. The continuous line refers to the theoretical decay described by Eq. 3.1 64

Figure 3.7: Location error map function of the changes in f_{opt} and Number of Events. The over imposed isocurves describe the final number of events used for the calculation of the location. The error is expressed in mm. 66

Figure 3.8: Histogram of the locations for the entire PEPT experiment for glycerol. Respectively, (a) shows the x coordinate and (b) the y coordinate. 68

Figure 3.9: Digital centering of the locations. In (a) the result of the projection is a 1/0 map of the entire locations. The sketch in (b) shows the method followed by the algorithm to create the mask. 69

Figure 3.10: First order interpolation over 5 points in (a) for point t(i) and x(i) and 3 points in t(i-1), x(i-1) and t(i+1), x(i+1) in (b) 72

Figure 3.11: Cylindrical coordinate θ vs. time for the 1st run of glycerol. Only 1 every 500 location is shown... 73

Figure 3.12: Distance expressed in cell number, between consecutive locations that fall in non consecutive cells. 75

Figure 3.13: (a) Schematic representation of the Mini Traction Machine (MTM). W is the load on the disk, T_F is the traction force exerted by the disk on the ball. (b) Speed ramp profile used to obtain the Stribeck curve. 80

Figure 4.1: Shear rate dependence of the Fluid gel. Cooling rate of 0.5 °C min^{-1}. In (a)shear rates from 0.5 s^{-1} and 100 s^{-1} while in (b) shear rates from 200 s^{-1} and 700 s^{-1}. 84

Figure 4.2:Double logarithmic plot of the increase in viscosity due to the formations of particles. 85

Figure 4.3: Micrographs of fluid gel particles as produced under different shear rates. Particles were diluted using 0.1% w/w KCl aqueous solution for the clearer observation of their structure 88

Figure 4.4 Shear thinning behaviour of 0.5% κ-carrageenan (0.1% KCl) fluid gels, produced under the different applied shear rates of 0.5 s^{-1}, 5 s^{-1} and 700 s^{-1}. The cooling rate during the formation process was 3 °C min^{-1}. 90

Figure 4.5: Viscosity of fluid gels, during their production process, as a function of the applied cooling rate. All systems are subjected to a constant shear rate of (a) 50 s^{-1}, (b) 100 s^{-1} and (c) 300 s^{-1}. 93

Figure 4.6: Response of fluid gels, produced at a constant shear rate of 100 s^{-1} and under different applied cooling rates, to a shear stress ramp of 4 Pa min^{-1}, measured as described in the text. Insert figure shows the observed yield stress dependence of the systems as a function of cooling rate. 94

Figure 4.7 Storage modulus for 0.5% κ-carrageenan and 0.1% KCl fluid gels produced at different shear rates and cooling rate of 0.5 °C min^{-1} immediately after production. 95

Figure 4.8: Kinetic growth rate ratio between fluid gel and quiescently cooled gel 98

Figure 4.9: Storage (G') and loss (G") moduli from stress sweep measurements for Systems A (a) and B (b) performed at 1 Hz. The 1st Sweep was carried out immediately after the production of the fluid gels and, after a "resting" stage of 15 min, it was followed by a 2nd sweep. Both systems produced from a 0.5% κ-carrageenan and 0.1% KCl "primary" solution; information on the process parameters during the production of each system is given in the main text. 99

Figure 5.1: Rheology of the 2% agar fluid gel after the PEPT experiment. The sample was measured at 25 °C. In (a) the viscosity is plotted versus the rate of shear while (b) shows the relationship between the shear stress and shear rate. 104

Figure 5.2: Tracer position in time for the glycerol during the experiment labeled "run 7". The figures in (a), (b) and (c) are respectively relative to the time progression of the Cartesian coordinates x,y and z. Meanwhile (d) is a 2 seconds extract from (a) (b), showing the rotational behavior of the tracer in the column and the number of acquired points per second. 106

Figure 5.3: 3D particle paths for run 4 of glycerol. Clockwise from the top left: (a) shows the z locations in time with the highlighted portion expanded in (b) to show the 3D plot of the locations and in (c) for the relative z-occupancy..... 107

Figure 5.4: Schematic of the position of the reference plane in the Return Time calculations. The two points indicate the initial (A) and the first consecutive crossing from the tracer of the plane (B)...... 109

Figure 5.5: Return time distributions for glycerol (a) and fluid gel (b) for different axial positions. 110

Figure 5.6: Schematic representation of the constrain imposed on the flow by the bottom wall of the pin stirrer. The arrows are inspired by the PEPT result. All the grey shaded areas are rotating, including the bottom wall. 111

Figure 5.7: Four characteristic particle paths for different return times, as specified in the labels. The circular markers identify the two crossing points of the reference plane. The 8 disks describe the volume interested by the pin rotation. 112

Figure 5.8: In (a), is proposed a schematic of the pin stirrer as a tank in series model. The following graphs show in (b) for glycerol and than for fluid gel in (c), the probability of a tracer leaving the surrounding of each pin to move either to an above compartment or below. 115

Figure 5.9: Eulerian azimuthally averaged contour plots for glycerol. On the left hand side the three components v_θ, v_z *and* v_r, *while on the right hand side the modulus v.* 116

Figure 5.10: Eulerian azimuthally averaged contour plots for 2% agar fluid gel. Similarly to glycerol, on the left hand side the three components v_θ, v_z *and* v_r, *while on the right hand side the modulus v.*..... 118

Figure 5.11: Velocity Vectors over imposed on contours of the magnitude of the velocity. (a) and (b) are the velocity vectors relative to the 6th pin of the stirrer meanwhile figures (c) and (d) show the vector plot near the inlet. Figure (a) and (c) are relative to glycerol and figure (b) and (d) to fluid gel...... 119

Figure 5.12: Velocity Profile along z, for r = 10 mm. From left to right are illustrated the comparison between tangential, axial and radial component of the velocity. The last graph shows the modulus of the velocity. 121

Figure 5.13: Glycerol azimuthally radial velocity plot. In (a) is shown the contour plots for each rotating pin with the velocity expressed as normalized by U_{tip}. *The remaining figures are the velocity profiles at for the given coordinates.* 123

Figure 5.14: Glycerol and 2% Agar fluid gel azimuthally averaged radial velocity profiles. All the velocities are normalized by U_{tip}..... 125

Figure 5.15: The azimuthally averaged contour plots of the shear rates measurements relative to glycerol in (a) and fluid gel in (b) and the relative volume distribution..... 127

Figure 5.16: Enhanced accuracy occupancy algorithm developed for fast moving tracer. 130

Figure 5.17: The contour plots in (a) and (b) are relative to the number of passes normalized by the maximum number of passes in the azimuthally averaged cells and the occupancy shown as sum of all the azimuthal values. In (c) the histogram of the occupancy for glycerol subdivided in to 2 mm bins. 132

Figure 5.18: The contour plots in (a) and (b) are relative to the number of passes normalized by the maximum number of passes in the azimuthally averaged cells and the occupancy shown as sum of all the azimuthal values. In (c) the histogram of the occupancy for the 2% agar fluid gel subdivided in to 2 mm bins. 133

Figure 5.19: Distributions of the shear rates encountered along 4 particle paths. In (a) for glycerol, (b) for fluid gel along the full particle path length, while only along the initial 60 seconds in (c) for glycerol and (d) for fluid gel. 135

Figure 6.1:Particle size distributions of fluid gels (a) with varying agarose concentrations (1% - 4%), produced at a constant shaft speed of 1450 rpm, and fluid gels (b) with the same 2% agarose concentration, produced at variable shaft speeds. 141

Figure 6.2:Texture analysis of the investigated fluid gels. (a) True stress versus true strain curves as a function of agarose concentration. (b) Young's elastic modulus E as a function of agarose concentration..... 142

Figure 6.3:Rheological behaviour (flow curves) of fluid gels as a function of agarose concentration..... 143

Figure 6.4:Stribeck curves, for increasing (open symbols) and decreasing (filled symbols) disk velocity ramps, displaying the tribological behaviour of fluid gels with agarose concentrations of (a) 1%, (b) 2%, (c) 3% and (d) 4%. For all the tests shown the applied normal load W was kept constant at 4N. Friction coefficient data points are average values of at least three repetitions while the solid lines only serve to guide the reader's eye. 144

Figure 6.5: Minimum film thickness h^R_{min} function of the disk speed obtained from Eq. 6.4 148

Figure 6.6: Schematic representation of the proposed mechanism of fluid gel lubrication. Zone A: the disk speed U is not high enough to induce entrainment of the particles; under these velocity conditions, only the fluid medium can access the gap between the ball and disk (a and b). Zone B: U is high enough to induce the onset of the entrainment of the particles, which results in an increase in the values of the friction coefficient μ; the gap between the ball and disk is similar to the size of the particles (c). Zone C: further increase in U allows for more particles to be entrained, which increases the gap between the surfaces above the dimensions of the particles and as a result μ again decreases with U (d)..... 149

Figure 6.7: Effect of variations of the applied normal load W on the tribological behaviour of fluid gels. Stribeck curves for a 4% agarose concentration fluid gel with W of (a) 6 N and (b) 8 N, and (c) for a 1% agarose concentration fluid gel with W of 1 N..... 152

Figure 6.8: Effect of particle size on the lubrication properties of a 2% agarose fluid gel. Stribeck curves shown are for a normal load of 4.5 N. 154

List of Tables

Table 2.1: Gel–Sol and Sol–Gel transition temperatures (T_{gs} and T_{sg}) and Activation Energies (ΔE_{gs} and ΔE_{sg}) for the Various Types of Cations Kara, Arda et al. (2007). Atomic and Ionic Radii for the same species. (C_T=3.6 10^{-2}eq l^{-1}). 16

Table 3.1: Concentration of κ–carrageenan and KCl in the fluid gels. 52

Table 3.2: Set up parameters for the PEPT experiment. 60

Table 3.3: Details relative to the runs constituting each experiment. 63

Table 3.4: Standard deviations of the velocity computed for different number of locations with 3 polynomials. . 71

Table 3.5: Formulation parameters for the production of agarose fluid gels. 78

Table 4.1: Power law coefficients B and c calculated from the data shown in Figure 4.2. 86

Table 4.2: Model parameters from Eq. 4.2 calculated by fit to the data of Figure 4.7. 96

Table 5.1: Details about the Shear rate distributions presented in Figure 5.15. 129

Table 5.2: Time weighted average shear rates relative to the full shear history described in Figure 5.19. The shear rates were calculated according to Eq. 5.2 136

Table 6.1:Power-law dependency of the rheological behaviour of agarose fluid gels and the corresponding zero yield stress, τ_0, calculated by extrapolating to zero shear stress. K and n are the consistency constant and power-law index, respectively. 143

Chapter 1.

INTRODUCTION

1.1. Background

Biopolymers have an important role in the food industry as structuring materials and/or as stabilizers in emulsion-based products. Their role in foods is often mirrored by their use in the cosmetics industry and personal care products. Nonetheless what is increasingly becoming evident is that the use of hydrocolloids only as simple gelling and thickening agents doesn't fully satisfy the industry and consumer-driven need for healthy, convenient but still high quality formulated products. This has led to the development of fluid (or sheared) gels, which can be formulated to meet a much wider range of structural requirements (Cassin, Appelqvist *et al.,* 2000; Norton, Smith *et al.,* 2000). Several neutrally charged hydrocolloids have been shown to form fluid gels upon shear cooling. A clear opportunity exists in producing fluid gels with controllable particle-particle interactions, based on the electro chemical activity of the solution.

The molecular structure of the hydrocolloid κ-carrageenan has been studied with extreme interest in the past (Rees, 1963; Rees, 1969). The strong ionic interactions between chains and their stereo specificity are responsible for the formation of an infinite network structure when κ-carrageenan undergoes gelation (Anderson, Campbell *et al.*, 1969). The gelation is kinetically favoured by the presence of salts, which act as bridges between the helices (Norton, Goodall *et al.*, 1979; Norton, Goodall *et al.*, 1983), and control the brittleness of the microstructure. The molecular model for the formation of fluid gels (Norton, Jarvis *et al.*, 1999) is valid for any biopolymer capable of gelling (Brown, Cuttler *et al.*, 1990), however no previous describes the *κ*-carrageenans chain-to-chain interactions in a fluid gel system.

The sensibility of the fluid gels to the process conditions such as shear and cooling rate (Norton, Jarvis *et al.*, 1999), require accurate knowledge of the fluid dynamic properties of

the process equipment used to move from the rheometer to a more industrially relevant bench scale production. The only reported study describing a bench scale production of fluid gel using a pin stirrer heat exchanger was published by Norton, Smith, *et al.,* (2000). They described accurately the production of agar fluid gel, without providing information on the fluid dynamic conditions used. But although the pin stirrer is commonly used in the production of margarine, and similar processes involving high shear and accurate cooling, there is a lack of quantitative measurements of its flow field. This is mainly due to the limitations of common measurement techniques. However, the use of positron emission particle tracking (*PEPT*) may prove an effective tool in studying the complex flow within the unit, with experiments focused in characterising the fluid velocity and shear.

In the use of fluid gels as structuring materials for food and cosmetics, a prerequisite is the microstructure response to be deformed into a thin film, upon spreading or during oral processing. For this reason fluid tribology, or thin film rheology is directly correlated to mouth and skin feel (Malone, Appelqvist *et al.*, 2003). An increasing number of researchers are focusing their attention on the lubrication between soft surfaces (Adams, Briscoe *et al.*, 2007; Dresselhuis, de Hoog *et al.*, 2008), however very few studies have been reported, describing lubricating role of particles suspended in fluids (de Wijk and Prinz, 2005).

1.2. Objectives

The three main objectives of this study are to investigate the mechanism of fluid gel formation from hydrocolloids, whose repeating units bear an electrolyte group; then to explore the efficiency of processing within a pin stirrer to provide fluid gels at larger volumes and finally to investigate the thin-film-rheology/tribology of fluid gels as produced by the pin stirrer.

To work towards these goals, experiments will aim at characterizing the phase transition of the polyelectrolyte κ-carrageenan into fluid gels. The effect of shear rate on the segregation of the biopolymer in fluid domains during gelation will be controlled within a rheometer in order to investigate the final microstructure and flow properties of the fluid gels. The relationship between particle shape and size with the applied shear rates during the gelation in laminar flow will be examined with particular interest to the kinetic of structuring during the shear process.

The reported large-scale production technology for fluid gels is the pin stirrer heat exchanger. Nevertheless due to the limited access to the enclosed flow in this unit, knowledge on the nature of its fluid dynamic is limited. Positron emission particle tracking will be employed to overcome this barrier and characterise the flow. Note that the flow structures in the pin stirrer for a gelling, shear thinning fluid have never been examined before, so the results presented herein aim to provide a deeper understanding of particle paths, velocity and shear rates.

The lubrication properties of the fluid gels produced in the pin stirrer will be characterized using a Mini Traction Machine. The scope is to describe the role of the fluid gel particles in

lubrication. Proposing a model for the friction coefficient, that includes the effect of biopolymer concentration, normal load, sliding velocity.

1.3. Thesis structure

Chapter 2 describes the developments in the knowledge on biopolymers gelation in relation to the formation of fluid gels. A particular focus is given to the underlying gelation mechanism, of the different hydrocolloids and to the known mechanism of formation of the fluid gels. The reviewed articles cover the physical chemistry of the hydrocolloids used in this work and arguments their use in improving current formulations in food and cosmetics. Chapter 2 concludes, with a review of the lubrication properties of dense suspensions of particles and a review of the Position Emission Particle Tracking technique used to characterise the Pin Stirrer Heat Exchanger.

Chapter 3 is divided into two main sections. The initial "*Materials*" section includes a description of the chemical compounds used in the experiments and their preparation. The second section includes the "*Method*s" followed in carrying out the experimental work basis of this thesis. The methodology includes also a description of the programming codes developed to analyse the *PEPT* data. The innovative algorithms developed to characterise specific flow properties, are discussed in conjunction with the *PEPT* result in Chapter 6.

Chapter 4 describes the results of the microstructure investigations on κ−carrageenan fluid gels. After initial considerations on the effect of concentration on the gelation, the chapter develops around an exemplifying concentration. Focusing on parameters that control the mechanisms of formation. The competing mechanisms responsible for the formation of the particles are fully described, including the limiting shear rate for the formation of spinodally decomposed particles. The rate of removal of heat is introduced are an engineering parameter

to produce high yielding microstructures and discussed on the basis of kinetic arguments. The electrolytic nature of the monomers of κ−carrageenan persists in the fluid gel, with the cooling rate controlling the final kinetic of aggregation of the particles. The latter controls finally the reversibility upon cycles of stress ramps of structuring parameter *G'*.

Chapter 5 describes the fluid dynamic conditions within a model pin stirrer heat exchanger; obtained by using Positron Emitting Particle Tracking (*PEPT*). This chapter opens with the description of the flow patterns during the gelation process. The consecutive data analysis builds throughout the chapter, leading to the Eulerian maps of the shear rate presented in conclusion. The study is carried out in parallel between a reference Newtonian solution (99% in weight of glycerol) and the fluid gel (2% in weight of agar). The critical parameter of shear rate, important for the particle formation, is quantified upon concluding the chapter with a description of the shear history experienced by a fluid element. This chapter concludes with recommendations for future design of equipment aimed at the production of large-scale fluid gels.

Chapter 6 presents in detail the result on the lubrication of the fluid gels. The presence of the particle is accurately captured by the tribometer, providing information for the understanding of the role of particle size and particle elasticity in the lubrication mechanism. The behaviour of the fluid gels is then carefully discussed focusing the considerations on the Stribeck curves. The concluding model for particle entrainment considers all the experimental evidence discussed.

Chapter 7 forms the final contribution to this thesis. It summarises the main conclusions drawn from this research, and puts forward recommendations for future studies based on the author own experience.

The results obtained during this study have been published as follows:

- *Gabriele, A., F. Spyropoulos and I. T. Norton (2009).* Kinetic study of fluid gel formation and viscoelastic response with kappa-carrageenan. *Food Hydrocolloids 23(8): 2054-2061.*

- *Gabriele, A., F. Spyropoulos and I. T. Norton (2010).* A conceptual model for fluid gel lubrication. *Soft Matter 6(17): 4205-4213.*

Finally, the results obtained during this study have been presented as follows:

- *Gabriele, A., F. Spyropoulos and I. T. Norton (2009).* Rheology of microstructures based on spinodally decomposed polysaccharides fluid gels. *5th International Symposium on Food Rheology and Structure, Zurich.*

- *Gabriele, A. S. Bakalis, D. J. Parker and P. J. Fryer (2009).* Investigation of momentum transport and mixing using PEPT and MuPEPT. *5th International Symposium on Food Rheology and Structure, Zurich.*

- *Gabriele, A., F. Spyropoulos and I.T. Norton (2010).* Lubrication and Tribology of food pastes. *Formula VI, Stockholm.*

- *Gabriele, A., F. Spyropoulos and I.T. Norton (2010).* Soft Pastes Tribology: Agarose Fluid Gel. *10th International Hydrocolloids Conference, Shanghai*

Chapter 2.

LITERATURE REVIEW

2.1. Introduction

This chapter reviews the most relevant literature and illustrates the research carried out on fluid gels. Particular focus is given to the underlying gelation mechanism, of the different hydrocolloids and to the known mechanism of formation of the fluid gels.

This review covers the physical chemistry of the hydrocolloids used in this work and describes their role in current formulations in food and cosmetics.

The current chapter concludes, with a review of the lubrication properties of dense suspensions of particles and a review of the Position Emission Particle Tracking technique used to characterise the Pin Stirrer Heat Exchanger, employed for the production of fluid gels.

2.2. Hydrocolloids

Hydrocolloids are granted a presence in most food formulations and a constant interest, due to their multi-functionality. As a matter of a fact, hydrocolloids alone have the potential to constitute the base structure of food, but are commonly used as emulsion stabilizers by modifying the viscosity (thickening and gelling) at typically low concentrations, less than 2% (Dickinson, 1989; Smewing, 1999). Other than stabilizing emulsion, they have been extensively used in ice creams as inhibitors of ice and sugar crystal formation (Buyong and Fennema, 1988), and as flavour release controllers during mastication. In the latter, the degree in which the hydrocolloid solutions mix with saliva, is controlled at a molecular level by the degree of chain entanglement, which determines flavour perception (Morris, 1993; Ferry, Hort *et al.*, 2006).

Hydrocolloids are indeed a vast family of macromolecules, they can be divided for clarity into two main groups, polysaccharides and polypeptides (proteins). Polysaccharides are

complex carbohydrates. They are made up of chains of monosaccharaides (*i.e.* sugars), which are linked together by glycosidic bonds, formed by a condensation reaction (Harden and Young, 1913). The linkage of monosaccharaides into chains creates macromolecules of greatly varying molecular weight ranging from chains of just two monosaccharaides, disaccharide (*i.e.* sucrose) to the polysaccharides consisting of many thousands sugar monomers.

Proteins are conceptually similar to polysaccharides. They are large macro molecules formed of repeating monomeric units, the amino acids. Proteins are assembled using information encoded in genes. Each protein has its own unique amino acid sequence that is specified by the nucleotide sequence of the gene encoding this protein. Although similarly to the polysaccharides, it is possible to identify a base unit, it is impossible for proteins to be described simply by a singular repeating pattern.

The origins of hydrocolloids are various. Starch, the most common, derives from plants but hydrocolloids can be derived form a variety of different sources. In everyday products, hydrocolloids derived from animals include for instance casein and whey protein from milk; gelatine from collagen which is the primary constituent of white fibrous connective tissue, skin and bones (Ledward, 2000). Less common but slowly increasing in their importance are hydrocolloids such as gellan, deriving from microbial fermentation.

Certain hydrocolloids belonging to any of these classes are capable of rearranging their molecular conformation, for increasing activity; this change in molecular conformation is referred to as gelation. Gel to solution, is a thermodynamic phase transition representing a balance between polymer-polymer interactions, as in the solid state, and polymer-solvent interactions in solution. In other words, the loss of conformational freedom and hydration energy, is compensated by energetically favourable chain-chain interactions (Morris and

Rees, 1978). In polysaccharide systems the bonds between the macromolecules, are usually not covalent, with few exceptions (*i.e.* gellan gel), and therefore the exact nature of the inter-chain binding varies from one polysaccharide system to another. Both carrageenans (Anderson, Campbell *et al.*, 1969; Rees, 1969) and agar (Arnott, Fulmer *et al.*, 1974) families of algal polysaccharides employed in this work, form a double-helix structure with an embedded inter-chain hydrogen bond (Morris, 1998). The hydrocolloids used in this work, have algal origin and are in specific sourced from the family of red seaweed, κ-carrageenan and agarose. The gelation process of these hydrocolloids is triggered by different conditions.

(a) *κ-carrageenan*

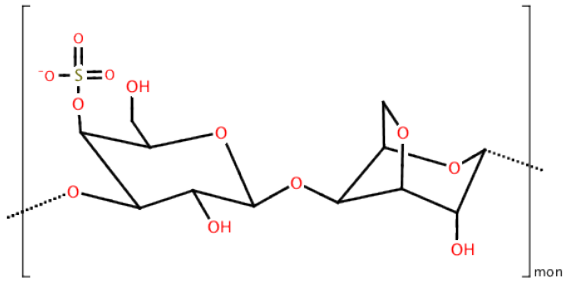

(b) *ι-carrageenan*

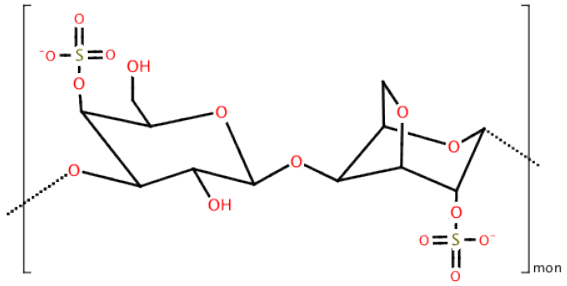

(c) *λ-carrageenan*

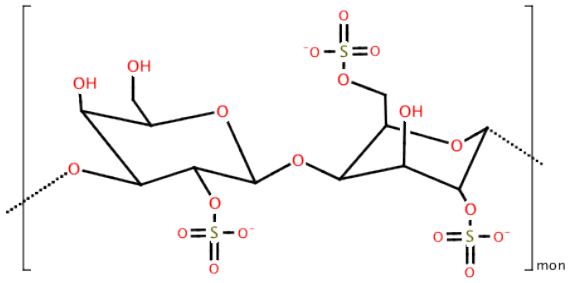

Figure 2.1: Primary $(A-B)_n$ *structure of carrageenan. Adapted from Anderson, Dolan et al. (1968)*

2.2.1. Spinodal decomposition of metastable solutions

During every phase transformation of a thermodynamic system, represented in this work by the gelation of a polysaccharide solution, finds itself in to a metastable condition, which may be perturbed by two different infinitesimal changes in the conditions. One cause of these perturbations is the infinitesimal change in local compositions of the solution. Gibbs formulated the general principles for this kind of instability and also described the second cause of perturbation of a solution. These other changes are those induced by the presence of an infinitesimal droplet of material with properties approaching those of the more stable phase (Gibbs, 1957). The first perturbation results in the solutions to decompose spinodally into two thermodynamically more stable phases. The second perturbation is also known as nucleation and growth. In spinodal decomposition, the solution is not unstable to fluctuations which form small droplets, but it is unstable to high amplitude fluctuations which form droplets of which surface tension contributions are larger than the volume energy contributions. This cutoff amplitude can be shown to prohibit the system to decompose on too small scale (Cahn, 1961).

The process of catastrophic decomposition by spinodal mechanism can be pictured as a ball in equilibrium on the summit of a hill, where only by providing a sufficiently large amount of energy is possible to tilt the ball down hill.

2.2.2. Gelation induced by ionic activity

Carrageenans are a group of sulphated galactans extracted for commercial production from the Rhoophycae family of red seaweed. Different species have different yields in different types of carrageenans, mostly of genus *Chondrus*, *Eucheuma*, *Gigartina* and *Iridaea*.

Euchema cottonii for instance, is the species from which κ-carrageenan (kappa) is principally derived (Imeson, 2000). κ-carrageenan and ι-carrageenan (iota) are the two biopolymers of the carrageenan group able to form a gel. κ-carrageenan, is out of the two, the biopolymer with the least number of sulphated units, and therefore its gel is the most resilient (Thomas, 1997). The family of the carrageenan hydrocolloids include beside κ-carrageenan, also ι-carrageenan (iota) and λ-carrageenan (lambda), all represented in Figure 2.1. λ-carrageenan has the highest number of sulphated groups and is consequently non gelling. The lack of the $^{1}C_{4}$ 3,6-anhydro-link, as opposed to the ι and κ allows the galactose residues to revert to their $^{4}C_{1}$ conformation do not allowing for the initial double helix formation required for gelling (Yuguchi, Thu Thuy *et al.*, 2002). Although it will not be discussed further, it is interesting to note that λ-carrageenan, is believed to be the biological precursor of both κ and ι (Rees, 1963).

2.2.2.1. κ- carrageenan

κ- carrageenan is an $(A-B)_n$ copolymer of O-β-D-galactopyranosyl-4-sulfate-$(1-4)$-O-3,6-anhydro-α-D-glactopyranosyl- $(1-3)$ (Anderson, Dolan *et al.*, 1968). The particular dimensional arrangement of the molecular groups bond to the polysaccharide backbone allows, under specific thermodynamic conditions, for the gelation to occur. κ-carrageenan, similarly to others polysaccharides, gels under specific ionic activity of the solution. The process of gelation is best defined using the thermodynamic concept of dynamic equilibrium

between polymer-polymer interactions, against polymer-solvent interactions; this important consideration reduces the gelation process to a phase transition. During the past two decades, the chemical reaction associated with this transition has been a source of debate among researchers. The dispute regarded the number of polymeric chains involved into the formation of the helices.

Although Anderson, Campbell *et al.,* in 1969 proposed first the double helix ordering based on x-ray diffraction, this was never fully accepted, and later Smidsrød, Andresen *et al.,* (1980) and Paoletti, Smidsrød *et al.,* (1984) studied the ordered-disordered transition of κ-carrageenan, the latter purely from considerations of theoretical thermodynamic, suggesting a coil ordering of single helices joined by the salt cations, Figure 2.2(b).

Finally only with the work of Morris, Rees *et al.,* (1980) and Norton, Goodall *et al.,* (1979), the double helix conformation was established as the gelled structure of carrageenans, following the mechanism described by Figure 2.2(a). The role of the cations such as K^+, Na^+, was found to be of bridging between the double helices, creating the gelled infinite network. More evidence was later found, by kinetic studies done using optical rotation technique (Bryce, Clark *et al*., 1982). Their theories have been confirmed using small-angle X-ray scattering (Yuguchi, Thu Thuy *et al.*, 2002). But all agree on two separate phases constituting the mechanism of gelation, the coil-double helix transition and the following association of the helices to form a cross linked structure by ionic bridges by cations. Both the conformations are described in Figure 2.2.

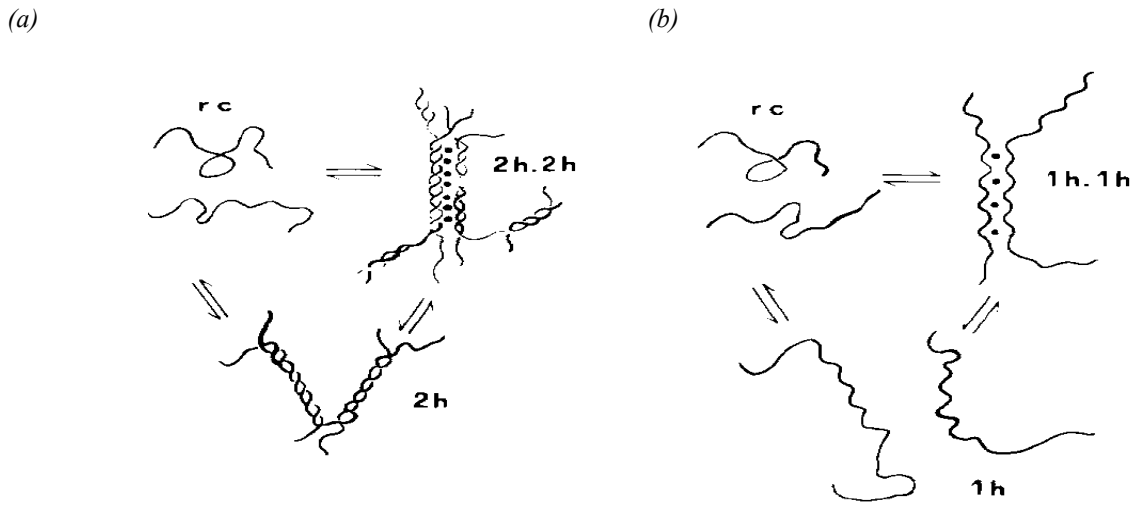

Figure 2.2: The two models for the conformational transition and aggregation in κ-carrageenan. In (a) the double helix conformation while in (b) is shown the single helix. (Paoletti, Smidsrod et al., 1984)

The gel is thus formed when the strength of the repulsion between the helices is lowered, for example, by introducing a counter-ion (K^+), which binds to the negatively charged helix. Rees in 1969, first described mechanism for the sol-gel transition of carrageenan and later Morris, Rees *et al*. (1980) in a solution of KCl, and Rochas and Rinaudo (1980) described the order-disorder transition in terms of ionic strength, temperature and chemical nature of the counter-ions. Observing a change in conformation identified as specific rotation of the molecules observed with optical rotation and conductivity of the carrageenan solution. They reported the melting temperature to be independent of the total ionic concentration (C_T) as defined by Eq. 2.1.

$$C_T = \bar{\gamma}\, C_P + C_S \qquad \text{Eq. 2.1}$$

Where, C_S and C_P are respectively the added salt and polymer concentrations and $\bar{\gamma}$ the mean activity coefficient evaluated as the arithmetic mean of the activity of the solution between the helix structure and the random coil organization in the solution at a gelation temperature, T_m. These values were measured with conductivity over a range of values of $\sqrt{C_P}$ from 0.025 to 0.2 $eq^{0.5}\ l^{-0.5}$ for sodium and potassium as counter ion (Rochas and

Rinaudo, 1980). The mean K^+ activity coefficient for the helix configuration for T_m ranging from 15 to 25°C was 0.4. These values resulted in good agreement with those obtained by the equations proposed by Manning (1969). They also showed through conductivity measurements, the existence of linear relationship between $\log(C_T)$ *vs* T_m^{-1} and constructed a phase diagram for the ordered-disordered transition. With distinct curves for the heating or cooling process that is taking place, highlighting the presence of a hysteresis cycle, Figure 2.3.

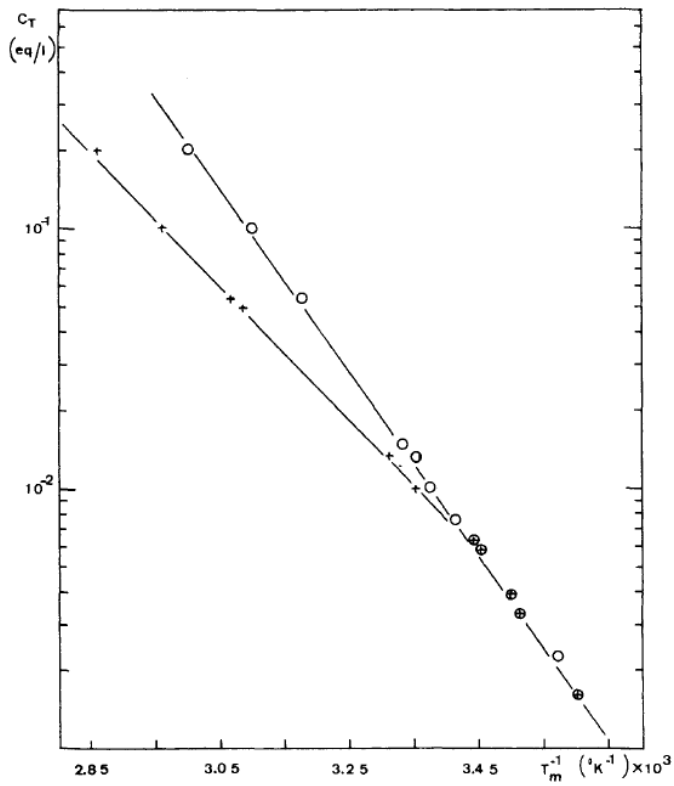

Figure 2.3: Variation of the melting temperature with the free potassium concentration C_T. (x) heating curve and (o) for the cooling curve (Rochas and Rinaudo 1980).

2.2.2.2. Role of cations

The cations play a fundamental role in the gelation process of carrageenan (Norton, Goodall *et al.*, 1983). Cations in solution are able to stabilize the anionic monomers of the polyelectrolyte chain, by site binding forming an ionic bond or otherwise by proximity

binding, where the cation neutralizes by vicinity the anionic charge of the monomer. This bond is often referred as atmospheric bond and by its nature the ions have high mobility.

Norton, Goodall *et al*. (1983), suggested that ions such as tetramethylammonium (Me_4N^+) with high ionic radius are able to interact with the sulphate groups only by atmospheric interaction, thus pointing out the possibility by the biopolymer to form an ordered structure only at high concentrations of Me_4N^+ compared to ions capable of ionic bonding, as shown in Figure 2.4. From their work also emerged that more sulphated groups in kappa-carrageenan participate to ion-pair formation with K^+ that iota-carrageenan for the same K^+ concentration.

Ions	Electronegativity	T_{gs} [°C]	T_{sg} [°C]	ΔE_{gs} [$kJ\ mol^{-1}$]	ΔE_{sg} [$kJ\ mol^{-1}$]	Atomic Radius [*pm*]	Ionic Radius [*pm*]
-	-	49.3	37.5	21.4	29.8	-	-
Li^+	0.98	51.2	37.5	36.4	50.0	145	76
Na^+	0.93	52	38.3	35.7	63.8	180	102
K^+	0.82	62	47.9	21.6	36.1	220	138
Mg^{2+}	1.31	55	39.1	39.5	49.8	150	72
Ca^{2+}	1	58.8	40.4	36.5	56.3	180	100
Sr^{2+}	0.95	58.5	39.4	33.2	55.1	200	118

Table 2.1: Gel–Sol and Sol–Gel transition temperatures (T_{gs} and T_{sg}) and Activation Energies (ΔE_{gs} and ΔE_{sg}) for the Various Types of Cations Kara, Arda et al. (2007). Atomic and Ionic Radii for the same species. (C_T=3.6 10^{-2}eq l^{-1}).

Recently, the effect of different cations on the binding energy to the polyelectrolyte was studied by Kara, Arda *et al.*, (2007), extending the work carried out earlier by Rochas and Rinaudo (1980), as shown in Figure 2.4. The concentration salt on the gelation of κ-carrageenan was studied by the use of photon transmission technique. They quantified the effect of different chloride salts on the gelation temperatures and energies of activation, their results are reported in Table 2.1 (Kara, Arda *et al.*, 2007). The additional two columns have been added to show additional information on the incumbency of the atoms, bound to the helices.

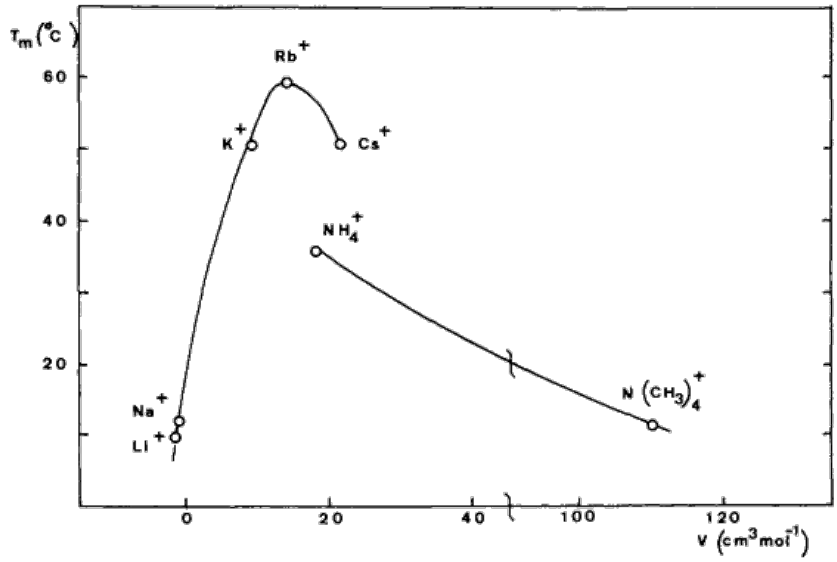

Figure 2.4: Variation of T_m obtained from optical rotation with the partial ionic volume of monovalent counter ions in excess of external salt ([Cl^-] = 0.1 N). (Rochas and Rinaudo 1980)

2.2.2.3. Role of anions

Within the last few years, contrasting evidence on the role of anions has been produced; Rochas and Rinaudo (1980) first excluded the effect of the anions on the conformation of carrageenan as proved by the invariance of the T_m, with different potassium salts. Evidence of the interaction between anions and the carrageenan polysaccharides was later investigated by NMR spectroscopy, proving that anions play an active role in the ordered gelled structure by Grasdalen and Smidsrøed (1981). Further work carried out by Norton, Morris *et al.* (1984), proved that the equilibrium stability of the κ-carrageenan in the presence of a constant concentration of any cataion depends on the anions, and more quantitatively it can be described as a direct relation between the value of the Hofmeister number and the value of enthalpy of coil-helix transition.

The role of anions in the κ-carrageenan helix conformation was later studied, differentiating between the effect that they produce in the equilibrium between helix-coil, in other words the T_m, and their effect on the kinetic of gel formation (Austen, Goodall *et al.*,

1988). This was achieved by measuring the number of disaccharide pairs actually participating to the gelation (η_{app}) and the ratio between the apparent enthalpy of formation at the coil-helix transitions (ΔH_{app}) and the apparent enthalpy of gelation for each disaccharide residue pair (ΔH_f) for different halogens. Austen, Goodall *et al.*, (1988) observed that by moving thought the halogen series from I^- to F^- the portion of the coil in helix conformation reduces.

To conclude, the resulting reduction in charge density of the polymer in the presence of K^+ has the effect of promoting both conformational ordering and aggregation. However, despite this net displacement in the direction of order and packing, the result for the potassium salt form show the same systematic variations through the anion lyotropic series as those obtained with Me_4N^+ as cation.

2.2.2.4. Kinetic studies

The kinetic of the κ-carrageenan gelation is divided into primary ordering where the random coils in solution form helices and the secondary conformation during which the double helices aggregate building ionic bridges (Austen, Goodall *et al.*, 1985; Austen, Goodall *et al.*, 1988). The primary conformational follows the reaction scheme proposed in Eq. 2.2:

$$2Coil \underset{k_{-1}}{\overset{k_2}{\rightleftarrows}} Helix \qquad \text{Eq. 2.2}$$

The model for the reaction rate that gives the best fit is a second order forward and first order back reaction (Austen, Goodall *et al.*, 1985; Austen, Goodall *et al.*, 1988), which integrating over time leads to:

$$\frac{x_e}{\left(a_0^2 - x_e^2\right)} \ln\left(\frac{x_e\left(a_0^2 - xx_e\right)}{a_0^2\left(x_e - x\right)}\right) = k_2 t \qquad \text{Eq. 2.3}$$

Where x and a are the residue concentration in the disordered and ordered form. This reaction scheme gives a very good fit with the experimental values, confirming the double helix ordered structure of κ-carrageenan.

The secondary conformational mechanism is a second order irreversible reaction scheme.

$$\frac{x}{x_f\left(x_f - x\right)} = k_2^{'} t \qquad \text{Eq. 2.4}$$

2.2.3. Biopolymers undergoing thermal gelation

2.2.3.1. Agarose / agar

Agar is mixture of two polysaccharide components: agarose and agaropectin (Araki, 1937), in proportions depending on the original raw material and manufacturing process (Armisen, Galatas *et al.*, 2000). They are extracted from specific red seaweeds, traditionally Rodophyta gelidum amansii, but other species from the same family are also commonly used (Falshaw, Furneaux *et al.*, 1998). The commercial value of agar is determined by its yield and physical properties. The gel strength and gelling temperature are function of the quality. The gelling properties of agar have extended its use to processed foods as a gelling agent, cosmetics and pharmaceutical products, besides applications in medicine and biotechnology (Marinho-Soriano and Bourret, 2005).

Agaropectin is a polysaccharide containing sulphate ester, pyruvic acid and D-glucuronic acid in addition to agarobiose, and because of these groups, agaropectins are not able to gel. Nevertheless, experiments done with optical rotation proved that they do have a reversible random coil – double helix transition (Norton, Goodall *et al.*, 1986) confirming that the

sulphated groups present on the polysaccharide backbone prevent further ordering. Due to the lack of practical applications, agaropectins have been studied less than agarose, but they are known to be precursors in the formation of agarose by enzymatic polymerization and de-sulphation consequence of the cellular metabolism of the algae.

Agarose, as mentioned earlier, is one of the two main biopolymers present in agar, and responsible for its gelation. Molecularly agarose, is a polymer consisting of the monomer agarobiose formed by alternating 3-linked β-d-galactopyranosyl and 4-linked 3, 6-anhydro-α-l-galactopyranosyl units (Araki, 1956). In addition, the transition temperature of agarose depends also to the polymeric chain length and the irregular presence on the chain of sulphated groups, depending on the different cell metabolisms (Dea and Morrison, 1975). Agarobiose, is therefore the basic disaccharide structural unit of agarose (Figure 2.5), and its helix conformation confers agarose the greatest gelling capacity between all the neutrally charged polysaccharides.

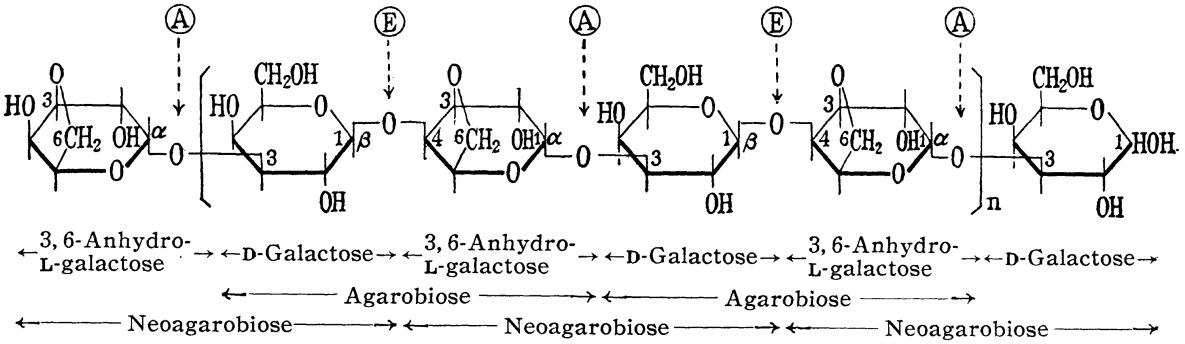

Figure 2.5: The chemical structure of Agarose (Araki, 1956)

Studies done on optical rotation of various solutions of pure agarose, have clarified the mechanism behind the abovementioned gelling capacity. Tako and Nakamura in 1988 proposed a detailed model for the agarose gelation, based on intra-molecular hydrogen bonding between the –OH group on the 4th carbon of the D-galactose and the adjacent hemiacetal oxygen atom of the 3,6-anhydro-L-galactose (Figure 2.5). This bond occurs below

the transition temperature of approximately 60 °*C* and is followed by a more rigid inter-molecular hydrogen bond between two distinct polymers chains.

The gelling capacity of agarose is entirely due to these intra- and inter- molecular bonds that take place as the temperature of the solution is lowered below the phase transition point. By means of X-ray diffraction Arnott *et al* (1974) characterized the new molecular ordering. They proposed the double helix structure model, as shown in Figure 2.6(a). In this model each chain is considered to forms a left handed 3-fold double helix with pitch of 1.90 *nm*. The two biopolymers molecules constituting a double helix are shifted alongside each other by exactly 0.95 *nm*. The quiescent gel has a strong network structure and is capable to sustain mechanical deformation up to a critical strain when it fractures (Normand, Lootens *et al.*, 2000).

(a) *(b)*

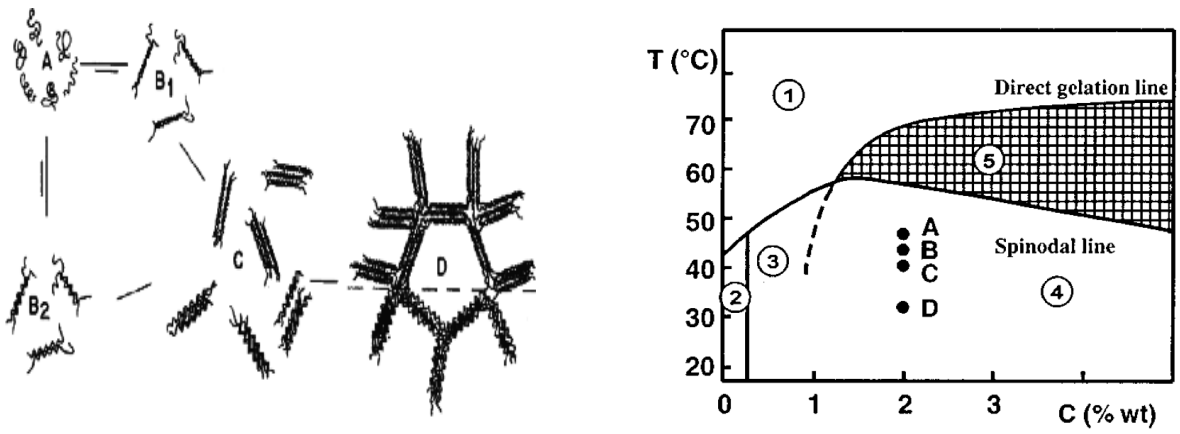

Figure 2.6: (a) Gelation of the chains of agarose (Armisen, Galatas et al., 2000) with the step A→B₁→C suggested by (Morris, Rees et al., 1980). While in (b), courtesy of (San Biagio, Bulone et al., 1996) the phase diagram of agarose with description of the different phenomena leading to gelation. (1) is a thermodynamically stable solution. (2) Freely drifting gelled regions, sample remains macroscopically liquid. (3) Spinodal promoted gel with mechanism described in the text. (4) Gel formed because of kinetic competition between demixing, conformational transition and cross-linking (5) Direct gelation of the solution.

Consequently, the agarose gel molecules are only hydrated back in solution, at temperatures above 85 °*C* (Armisen, Galatas *et al.*, 2000), for which the polymeric helices

dissociate due to an increase of the energy of the Brownian motion of both the polymer and the water molecules. Slight differences in the gel to solution transition temperature is to be related to the degree of sulphatation of the polymeric chains of agarose extracted from different seaweed species (Dea, Morrison *et al.*, 1975; Armisen, Galatas *et al.*, 2000). Gelation of agarose is therefore thermo-reversible and can only be achieved through cooling, because of the neutral nature of the agarose biopolymer.

Once in solution, the agarose biopolymers assume a random coil conformation and are homogeneously distributed throughout the solution (Armisen, Galatas *et al.*, 2000).

As just introduced the apparent gelation of agarose occurs at 40 °*C*, but the gelation process becomes thermodynamically favourable at a temperature approximately of 70 °*C*, however kinetically un-favoured. San Biagio, Madonia *et al*. (1986) discussed their observations of the gelation of a solution of 0.5% in weight of agarose. Leone, Sciortino *et al*. (1987), for instance, show experimentally that an isothermal gelation of a 3% in weight agarose solution will occur after 1000 hours at 51.5 °*C*. Proving that, the gelation process is already thermodynamically favoured above 38 °*C*.

Later San Biagio, Bulone *et al*. (1996) by means of optical rotation techniques produced the more complete phase diagram reproduced in the illustration in Figure 2.6(b).

The mechanism of helix-helix association was elegantly described by Feke and Prins (1974). They related measures of the light scattering intensity to molecular ordering of a solution of 1% agarose. They asserted that under quenching conditions the solution of agarose, is capable of spinodally decompose into agarose rich domains and areas were a depleted concentration could be found. Only subsequently to this phenomena, after further cooling, these domains can network to create a three dimensional structure by establishing extra domain junction zones. This ramification further leads to the final infinite network

characteristic for quiescently cooled biopolymer solutions. Further work has added more insight in the process of quiescent spinodal decomposition, describing the process as one undergoing both gelation and phase separation.

More recently San Biagio, Bulone *et al*. (1996) found for agarose concentrations below 2% in weight, spinodal demix into polymer rich and polymer poor regions takes place before coil-double helix transition whereas at higher concentrations gelation appears to proceed directly from the homogeneous solution state (see Figure 2.6(b)). In their study, they identified the kinetic sequence behind the mechanism of gelation, beginning with the initial spontaneous generation of polymer-rich and solvent-rich regions, followed by cross-linking of the polymer chains within the polymer-rich regions through the sample, still in the sol state. The final step was found to be the further polymerization leading to cross-links between the domains, along pathways of polymer-rich regions.

Work describing the spinodal decomposition of solutions of biopolymer has only been done for agarose-water solutions, and similarities between agarose and similar biopolymers such as κ−carrageenan of furcellan, have only recently been speculated (Tuvikene, Truus *et al.*, 2008)

2.3. Sheared gelation of biopolymers solutions: Fluid gels

Fluid gels are defined as suspensions of gel particles obtained by the systematic application of a shear field during the gelation of a biopolymer solution (Brown, Cuttler *et al.*, 1990). The final properties of the microstructure vary greatly function of the formulation parameters, and process conditions such as shear. During the past years, “fluid gels” were also referred to as “sheared gels” and both these terminologies are currently employed. For clarity only the former will be used throughout this thesis.

Fluid gels can be distinguished in two main categories, fluid gels obtained by spinodal decomposition and fluid gels obtained through mechanical break up of clusters of forming gel, disrupting the networking process of the biopolymer chains.

Stable solutions of biopolymers can be made thermodynamically unstable by thermal quenching or by increasing the ionic activity of the solution. The thermodynamic instability triggers the onset of the phase transition referred to as the process of gelation. Under specific conditions of shear rate and biopolymer concentration, the gelation can occur either via nucleation and growth (Norton, Jarvis *et al.*, 1999) or through a catastrophic decomposition into biopolymer rich and biopolymer poor domains (*See section 2.3.1*). The mechanism of this separation is known as spinodal decomposition. The complete gelled structure is therefore achieved when the domains, under quiescently conditions, branch into an infinite network (Bulone, Giacomazza *et al.*, 2004).

The existence of these domains was also described by Onuki in 1987. Onuki stated, and described mathematically that the presence of these domains produced a measurable increase in viscosity, somehow proportional to their surface area, whilst applying shear. Biopolymer rich areas following spinodal decomposition were first experimentally observed by San Biagio, Madonia *et al*. in 1986 by dynamic light scattering. The domains were initially observed while forming, and subsequently Chan, Perrot *et al*. (1988) proved that the growth of the domains could be distorted by externally applied shear, determining also the size (Emanuele, Di Stefano *et al.*, 1991; Norton, Jarvis *et al.*, 1999).

$$\tau_M = \frac{6\pi\eta L_M^3}{k_B T}\,;\ \dot{\gamma}\tau_M > 1 \qquad \text{Eq. 2.5}$$

The remarkable relationship between the characteristic length scale, L_M of the domains and the applied shear during gelation is defined by Eq. 2.5. Where τ_M, is the Stokes-Einstein time scale for a particle diffusing though a liquid with low Reynolds number. η and k_B are respectively the viscosity and the Boltzman constant, while $\dot{\gamma}$ is the shear rate applied and during the gelation process.

Emanuele, Di Stefano *et al*. (1991), following the suggestions given by Onuki performed light scattering measurements of agarose solutions quenched under shear. Their measurements proved Onuki's theories and the presence of domains, of the size depending on the agarose concentration. The formation of the polymer rich regions corresponded to an increase of the viscosity of the solution inversely proportional to the shear rate $\dot{\gamma}$, according to $\dot{\gamma}^{-1.86}$ for a shear rate of ≈0.016 s^{-1} and a temperature of ≈43 *°C*. Emanuele, Di Stefano *et al*. (1991) later confirmed these findings and admitted that the surge in viscosity due to the formation of the domains falls below detectability for $\dot{\gamma}$>0.2 s^{-1}. Nonetheless, in their measurements the average domain size was found to vary from 0.3 μm to 3 μm, and function of the shear.

Summarizing, fluid gels obtained by the sheared gelation of agarose/agar and similar biopolymers such as κ−carrageenans (Chen, Hu *et al.*, 1998) follow a two step mechanism:

- *Liquid - liquid phase separation of the solution occourring via spinodal decomposition, resulting in two regions that have, respectively higher and lower than average concentrations.*

- *Subsequently the two coil to double helix transition is followed by crosslinking and therefore, gelation.*

In this framework, the systematic application of shear during the gelation process leads to two very distinct types of fluid gel, depending on the intensity of shear. In the case of a strong shear, the gelling biopolymer macromolecules present in different domains, are kept separate and the final fluid gel will have a narrow particle size distribution (Carvalho and Djabourov,

1997). On the contrary, a lower shear will only tear apart already formed clusters resulting in large and irregular particles (Gabriele, Spyropoulos *et al.*, 2009).

A wide range of material properties can be obtained changing the concentration, as shown in Figure 2.7, where for different agar concentration, it is shown the storage modulus (*G'*), varies by an order of magnitude over the range of concentration proposed. The fluid gel maintains a similar trend as the quiescently cooled agar gel.

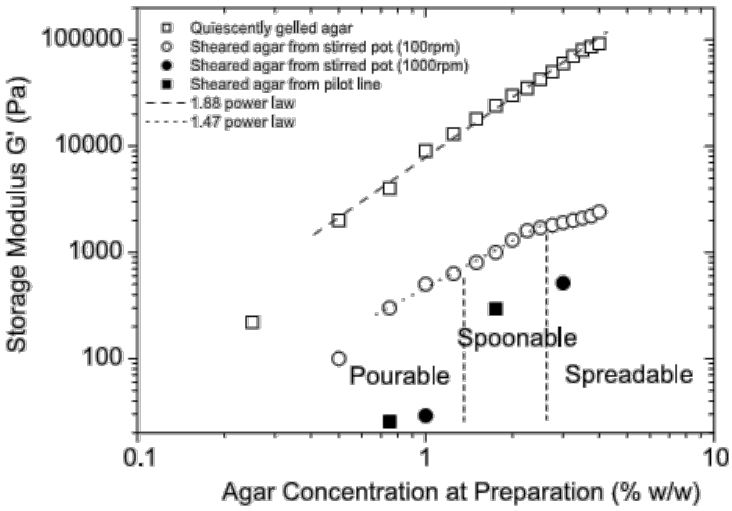

Figure 2.7: Storage modulus for agar fluid gel, prepared under different shear fields. (Norton, Frith et al., 2006).

An extension to what just described, includes the formation of mixed biopolymers fluid gels. Wolf, Scirocco *et al.*, (2000) have done a first approach to the study of these systems using three biopolymer mixtures, gelatin – guar, gellan – κ-carrageenan and gellan–sodium alginate, and different shear condition, they obtained morphologies ranging from elongated gel particles, ellipsoidal and spherical particles; obviously to such a variety of structures, correspond an as wide response to externally applied stress. The process is rather different to that employed for the single biopolymer sheared gel systems, primarily because the biopolymer mixtures exist in two phases in both the gelled and un-gelled states.

As a result a much lower level of energy input is required to produce shear-defined structures in biopolymer mixtures than is required to form a sheared gel, Figure 2.8. In a

recent work Norton, Frith *et al*. (2006), explained how this particularity can be of advantages in engineering food materials with similar or identical ingredients but with very different textures, by simply controlling the process conditions under which they are produced (Norton, Frith *et al.*, 2006).

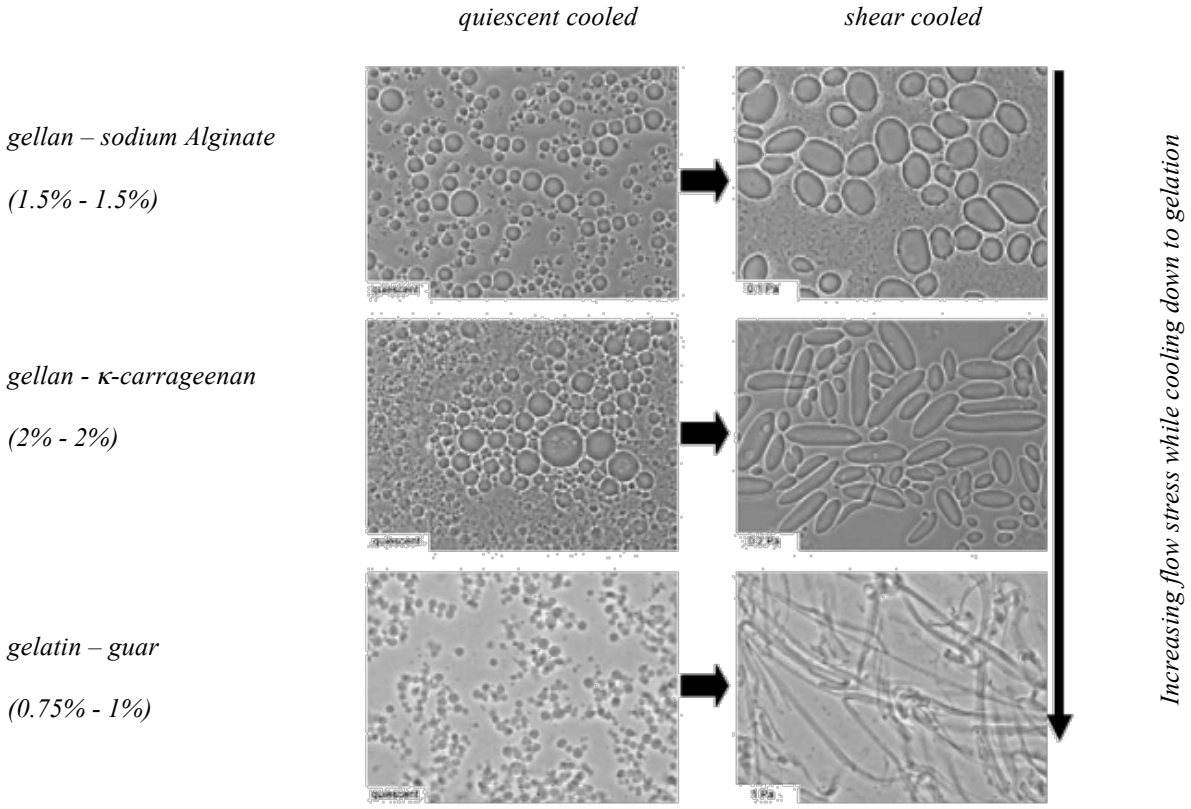

Figure 2.8: Range of morphology and dimension of particles obtained by shearing mixtures of different biopolymers in solution and cooled below the gelation temperature (Wolf, Scirocco et al., 2000).

2.4. Rheological properties and the sensory attributes perceived by the skin

The similarities between the flow properties in the oral processing and skin cream spreadability have been known for a long time (Shama and Sherman, 1973). The mechanism of perception and sensitivity of the skin present on the hands is extremely similar to those found in the oral cavity. To explain this similarity, it is important to consider that, the skin sensory perception depends on the information delivered from the receptors present on the skin to neighbouring cells that act as neurological relays. In this way each bit of information in each relay is associated with activity in a specific point on the body. Consequently, the sensitivity is a function of the number of receptors present on the skin. Kandel (1991) reported a diagram representing, the various parts of the body capable of tactile perception scaled by their sensitivity. The tip of the tongue, the fingers, and the hand, in this diagram has disproportionately large representations, reflecting greater degrees of innervation compared to the rest of the skin. They are however, extremely similar to each other and therefore they posses similar skin perception.

Nonetheless, as a consequence of the diversified function that the skin recovers, surface properties such as roughness and elasticity are extremely variable in different areas of the body. This calls for certain specificity in the non-sensory experiments to predict the consumer acceptance. Although the basic principles are similar, in literature, the two have been kept separate. The following paragraphs will summarize the significant aspects of both fields.

2.4.1. Food Texture and Palatability

Novel food products are currently engineered to satisfy consumer expectations in taste, and texture. The taste is determined by a combination of the action of volatile components detected by the receptors in the nasal cavity, and by non-volatile compounds sensed by the tongue inside the mouth. Understating the food acceptability is currently, a great challenge, because taste perception depends on a combination of biological, physiological and transport phenomena. Biopolymers for the matter have been shown to control the flavour release, by modifying the mass transport within the mouth (Morris, Richardson *et al.*, 1984). This work, is directly linked to taste perception, recent studies have shown that random coil polymeric solutions as opposed to granular structures, mix less efficiently as a result of entanglements between chains leading to different mouthfeel attributes and reduced release of compounds to the receptors (Ferry, Mitchell *et al.*, 2006; Ferry, Hort *et al.*, 2006) therefore suggesting a potential for biopolymers present in food as micro particles.

Although it is correct to affirm that texture is linked to taste perception, De Wijk and Prinz in 2003, investigating the effect of the addition of vanilla flavour to a model dessert concluded that the addition did not affect the perceived creaminess.

Texture properties of foods are an important component of food quality perception and acceptability. Texture evaluation of food products is a complex and dynamic process because physical properties of foods change continuously throughout the sensory experience. Texture assessment begins from the initial sight of a food product, and continues through touch, initial ingestion, mastication and swallowing. Food product developers and manufacturers are challenged to formulate specific textures and mouthfeel, largely due to a limited understanding of the relationships between texture perception and food structures. In order to have a complete understanding of food texture, a multi-disciplinary approach must be taken,

combining research from sensory studies, physiological studies, and physical and chemical properties of foods (Wilkinson, Dijksterhuis *et al.*, 2000).

Szczesniak identified and named the texture characteristics of food products in 1963 and subdivided them into three main classes (Szczesniak, 1963):

- *Mechanical Characteristics: the reaction of the food to stress*
- *Geometrical Characteristics: the arrangement of constituents of the food*
- *Other Characteristics: including moisture and fat content and other mouthfeel factors*

Since this classification of contributions to the food texture properties was proposed, much effort was produced to relate them to sensory evaluation in semisolid food. These efforts are effective if associated to consumer perception. In this review, are described selected studies that propose both results regarding non-oral measurement techniques in association with consumer panel tests. This approach has proved effective in drawing conclusions and advancing the understanding of oral and skin perception.

Initial studies on the reaction of food to externally applied stress, has begun with the study of large strain deformation (viscosity) to oral perception introduced by Shama and Sherman (1973). They explained that more the materials was viscous and lower would be the evaluated in the mouth at shear rate, *de facto* suggesting the need for small strain measurements of the viscosity, later introduced by other authors (Richardson, Morris *et al.*, 1989). As new measuring techniques were introduced, it was possible to quantify different aspects of the oral perception. It is possible to discriminate for instance between creaminess, slipperiness and grittiness (Tyle, 1993) (a review is provided by Kilcast and Clegg (2002)). Creaminess is often used by consumers to describe the appearance, taste or texture of food product (Elmore, Heymann *et al.*, 1999). For instance, although the importance of lubrication within the oral cavity during mastication is known to be fundamental (Hutchings and Lillford, 1988), only

recently creaminess was found to correlate experimentally to the food lubricating attributes (Malone, Appelqvist *et al.*, 2003; Malone, Appelqvist *et al.*, 2003).

During these years, the role of various different food constituents has been identified, fat content (Mela, 1988) rather than droplet size distribution when dealing with emulsified fat (Richardson, Booth *et al.*, 1993). Nonetheless only recently, awareness is rising around the importance of the lubricating properties of particles present in food, or created due to mastication.

Fluid gels are a suspension of biopolymeric particles, and although the active role of biopolymers in controlling of the rheological properties of food stuff, and perceived sensory qualities has been possibly first investigate by Morris, Richardson *et al*. in 1984, knowledge and publications regarding particles/oral cavity interactions are rare and recent.

2.4.2. Skin feeling and cosmetics

Everyone desires healthy and beautiful skin. The maintenance of the skin is for most people a daily procedure, therefore the demand for skin care products has created a vast industry, with an increasing investments in organic and natural skin creams (Hill, 2007).

As a commonly used skin care product, skin cream creates a smooth, soft, and moist perception for the consumer by altering the tribological properties, surface roughness, friction, and adhesion of the skin surface, but also the rheological properties, thickness and viscoelasticity. The way in which the skin cream changes the skin's tribological properties is of interest in beauty care science, as these tribological properties are closely tied to product performance and ultimately guide consumer like or dislike of that product.

In formulating a skin cream, it is important from a consumer point of view, to develop a carrying microstructure, able to deliver enhanced tactile sensory qualities. The role of the microstructure is to produce upon spreading, a feel soft feeling and smooth application. At the

same time it is necessary that the cosmetic product, possesses a certain chemical stability, and homogeneity. The quality factors of a skin cream are:

- *Sensorial,*
- *Rheological*
- *Mechanical*
- *Physicochemical*

These properties, extremely similar to those described by Szczesniak in 1963, while characterizing food texture perception, are related to the material properties such as viscosity, dielectric constant as well as how the constituents are assembled to form the microstructure of the product (structural attributes such as particle or droplet size distribution, phase volume fraction, and particle morphology). There is a close relationship between product performance, material properties and structural attributes. The rheology for instance is a dominant attribute, controlling how the product flows upon application, greatly impacting the consumer's perception. The consumer expects a cosmetic cream to spread easily when rubbed to the skin, but does not flow by itself during normal handling. Similarly to the sensory attributes identified for food, when dealing with texture characterization, also in creams it is important to identify qualities such as '*spreadable*', '*sticky*', '*creamy*' with physical models that relate rheological to sensorial attributes. For example, cosmetic emulsions assessed as good by a group of panellists have been found to have associated two distinct skin feelings, the first correlating with shear stress at the onset of the flow at high viscosity as high as 1,000 *Pa s* and a secondary skin feel, correlates well with the value of the stationary viscosity for the rate of shear prevailing at the end of application to the skin, and cream viscosity of 0.025 *Pa s* (Brummer and Godersky, 1999).

The rheological behaviour of creams and pastes is determined by the microstructure and the particle or crystals morphology (Narine and Marangoni, 1999), and as recently Snabre and Mills in 1999, published an elegant mechanistic mathematical model, the rheology of concentrated suspensions of viscoelastic particles; is also a function of particle elasticity and packing fraction. It is possible to obtain different pastes with shear thinning characteristics similar to those described by Brummer and Godersky in 1999, by using fluid gels and carefully controlling both process and formulation (Norton, Frith *et al.*, 2006).

2.5. Fluid dynamics of the Pin Stirrer Heat Exchanger

The chosen equipment for scale up of the production of fluid gels is the Pin Stirrer Heat Exchanger. This choice was based on earlier studies carried out by Norton and Frith, published in 2001. They showed how it is possible to obtain different fluid gels having determined fluid dynamic and viscoelastic properties, by adjusting the rotational velocity of the shaft (Norton and Frith, 2001).

The Pin stirrer used in this work is extremely similar to the common unit equipment used in food process industry. Food applications include the production of yellow fat spreads, which are water in oil emulsions stabilized by fat crystals such as margarine or mayonnaise, it is therefore commonly described as a crystallizer unit (Lund, Parker *et al.*, 1999) present at the end of a series of three units (A, B and C-unit), for this reason it is not uncommon to refer to the Pin stirrer as the C-Unit. More generally, the Pin stirrer is used in all those processes where high shear is needed whilst carefully controlling the temperature.

The high shear generated by the rotating pins, has the draw back of producing within the unit, complex fluid dynamic transport phenomena. A quantification of these phenomena is challenging for a variety of reasons. Firstly, the pin stirrers are typically enclosed in

cooling/heating jackets, which make impossible any conventional intrusive form of fluid dynamic measure. Furthermore, the change in viscosity that occurs within the Pin Stirrer due to heat flow and phase transitions, complicates any computational approach to the numerical simulation of the flow. Other difficulties, commonly involve the presence of multiple phases. The common approach taken by various workers consists in defining semi empirical correlations relating the final droplet diameter, in case of emulsions or bubble size for foams, to macroscopic engineering parameters, such as power drawn by the motor (Kroezen, Groot Wassink *et al.*; Hanselmann and Windhab, 1998). Recent work used computational fluid dynamics (*CFD)* in conjunction with a log normal models to predict the size distribution of low phase volume oil in water emulsions (Agterof, Vaessen *et al.*, 2003), but no experimental information is available in literature describing the localised fluid dynamic characteristics of the flow.

2.6. Experimental Investigations and Flow techniques

The experimental study of the fluid dynamic of process units, has posed during the years many challenges. The developing of a technique where the action of measuring did not affect the quantity measured, was possibly the very first. Techniques that are a clear example of invasive measurement include the widely used, hot wire anemometry (*HW*) (Bertrand, Couderc *et al.*, 1980). *HW* consists in a probe, which measures the rate of cooling of an electrically heated wire with very low heat capacity. The change in fluid velocity past the heated element, leads to changes in the heat loss, which is interpreted as velocity. The most common non-intrusive techniques are laser doppler anemometry (*LDA*) (Wu and Patterson, 1989) and particle image velocimetry (*PIV*) (Gabriele, Nienow *et al.*, 2009). Both consist in measuring the velocity of particles suspended in the flow. If these particles are small enough

they can be assumed to be good tracers, mimicking in their movement the flow. In *LDA*, the Doppler effect caused by particles crossing two coherent coincident laser beams, create a back-scattered light with a frequency proportional to the particle velocity. *LDA* is thus spatially limited to a point in space and requires a transparent wall. The *PIV* is based on the autocorrelation of two consecutive images of the flow tracers illuminated by a laser beam opened through the use of lenses into a sheet. The result of the autocorrelation algorithm is a reconstruction of the entire flow in the section of the equipment. Both techniques have the intrinsic limitation of necessitating transparent surfaces.

Following a completely different approach, Hawkesworth, O'Dwyer *et al*. (1986), developed a technique where the movement of a radioactive particle emitting positrons was traced in any enclosed systems, while placed between two detectors. Although of limited accuracy compared to the previously mentioned methods (Parker, Broadbent *et al.*, 1993), positron emission particle tracking (*PEPT*), is a real mean of understanding the flow patterns and rates of shear within the pin stirrer, overcoming the difficulties described above.

2.6.1. Positron Emission Particle Tracking (PEPT)

PEPT is based on the tracking of a radioactive isotope between to γ-ray detectors (Hawkesworth, O'Dwyer *et al.*, 1986). The technique in itself is a development of the positron emission tomography (*PET*), widely used in medicine and adapted by the department of applied physics of the Birmingham University by Hawkesworth, O'Dwyer *et al*. (1986) to track a single tracer. *PEPT* has been used ever since to investigate a variety of systems (Broadbent, Bridgwater *et al.*, 1995; Fangary, Barigou *et al.*, 2000; Parker, Forster *et al.*, 2002; Cox, Bakalis *et al.*, 2003; Bakalis, Fryer *et al.*, 2004). Because the *γ*-rays can penetrate a considerable thickness of metal, *PEPT* offers several advantages for providing an insight of the flow and mixing processes inside real-plant equipment without disturbing the process.

^{18}F was chosen, as the isotope most suitable for this study and at the present day is the most widely used radioactive tracer for *PEPT*. The half-life of ^{18}F is approximately 109 minutes, this characteristic makes it a perfect candidate for PEPT investigations. ^{18}F is produced on site in the department of physics by irradiation of a beam of ^{3}He ions from the Birmingham Radial Ridge Cyclotron, which converts oxygen to the radionuclide. In this isotope, a proton is converted to a neutron (n), with consecutive emission of a positron (a positive electron, β^{+}) and a neutrino (ν). The γ-rays are produced by the annihilation of the positron (β^{+}) with a near by electron (e^{-}), to produce a pair of 511 *keV* gamma rays emitted in opposite directions, as described in the reaction scheme in Eq. 2.6 and schematically in Figure 2.9.

$$\begin{aligned} p &\rightarrow n + \beta^{+} + \nu \\ \beta^{+} + e^{-} &\rightarrow 2\gamma \end{aligned} \qquad \text{Eq. 2.6}$$

An ideal tracer should therefore, emit only back-to-back gamma radiations of the specific wavelength (or frequency) and posses a reasonably long half-life to allow for the tracer to transit through most of the system.

The locations are reconstructed based on the algorithm developed by Parker, Broadbent *et al*. (1993). The reconstruction process is based on the hypothesis that for a steady tracer, the minimum distance between all the gamma ray trajectories captured by the detectors; identify the position of the tracer with an associated error in Figure 2.9. For a moving tracer, the data set is subdivided into data slices (event number) over which the algorithm is run iteratively. Starting from the complete number of events in the data set, the algorithm is run consecutively for each point considering at each passage only the events closest to the x_{n-1}, y_{n-1} z_{n-1}. Finally only a fraction (f_{opt}) of the original set of events is considered for the final identification of the location. Parker, Broadbent *et al*. (1993), showed that a value f_{opt} equal to

0.2 (20%), minimises the standard deviation, or error, of the localization. The output of this early stage processing gives the tracer position (x, y and z) as a function of time (t).

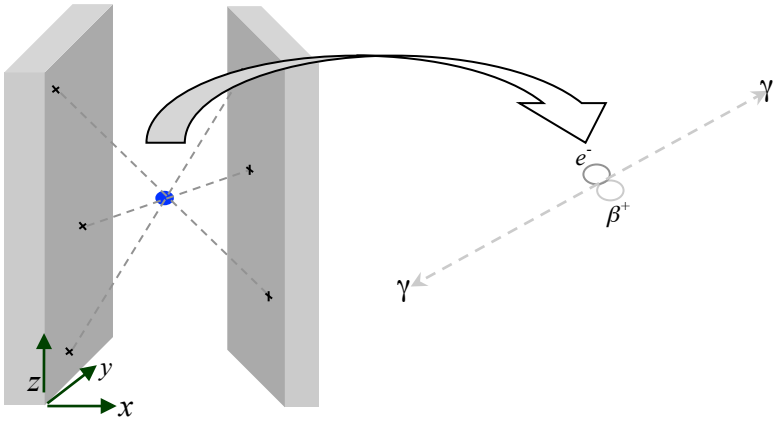

Figure 2.9: Set up of the C-unit within the detectors. In the extract, the nucleolus emits a positron, β^+, annihilated by an electron e^- present in the surrounding, producing the two back-to-back γ rays.

2.7. Tribology

Tribology is the science and technology of interacting surfaces in relative motion.

The first study on friction dates back to the XV century by Leonardo da Vinci. He postulated the first laws of friction as the resistance of motion experienced by one solid sliding over another. Leonardo Da Vinci did not publish his theories, so he never got credit for his ideas. The only evidence of their existence is in his vast collection of journals.

- *"When two bodies are in contact the direction of the forces of friction on one of them at its point of contact, is opposite to the direction in which the point of contact tends to move relative to the other."*

- *"If the bodies are in equilibrium, the force of friction is just sufficient to prevent friction and may therefore be determined by applying the conditions of equilibrium of all the forces acting on the body."*

- *"The ratio between friction force (F_f) to the normal load (W) between two surfaces depends on the substances of which the surfaces are composed and not on the normal load."*

The coefficient of friction μ_F, is defined as the ratio between the friction force and the normal load Eq. 2.7.

$$\mu_F = \frac{F_f}{W} \qquad \text{Eq. 2.7}$$

Lubrication is the process, or technique employed to reduce friction, by means of a lubricant. Various forms of lubrication have been devised during the years in order to reduce wear of the contacting surfaces. For two contacting bodies subjected to large displacements, lubrication may include: *Chemical lubrication,* consisting in adsorbing a chemical onto the contacting surfaces in order to change the material properties; *Lamellar lubrication,* based on the principle of interposing a soft metal or a lamellar solid (*i.e.* graphite) between the two sliding solids or *Magnetic fields*, where possible to drastically reduce the friction.

Nonetheless, the most commonly found form of lubrication is the *pressurized lubricant film* where, as the name suggests, the sliding/rolling solid surfaces are kept separate by a pressurized fluid.

2.7.1. Elastohydrodynamic lubrication

Elastohydrodynamic lubrication (*EHL*) is the mechanism that describes the separation by a lubricant film between two elastic solids loaded against each other in relative motion (Gohar, 2001). Attention to this science, come almost by chance, following observations in early studies on the absence of wear between moving gears under certain conditions of load and relative motion. In this type of lubrication the pressure in the contact region, is sufficient to deforms elastically the surfaces and also modify the viscosity of the fluid.

2.7.1.1. Surface deformation

The mechanism behind this form of lubrication consists of a significant elastic deformation of the lubricated surfaces, and the formation of an entrained fluid film. The effect that the fluid entrained has on the friction coefficient is determined mainly by the loading and geometrical parameters, rather than just by the lubricant properties (*i.e.* viscosity).

Hertz, first quantified the elastic deformation described in the *EHL* theory due to the two surfaces distorting elastically under the hydrodynamic pressure (Hertz, 1826). The assumption in the Hertz contact theory consisted in defining the initial unstressed geometrical condition of two compliant solids and then calculating the resulting contact surface by equalizing the deformation force to the normal load applied on the geometry (W), respecting the first-degree spatial continuity for both contacting bodies. As a result, of the contact between a ball and a disk, a circular area of radius a is formed, with a given by Eq. 2.8, where R is the radious of the ball and E^* is the reduced elastic modulus.

$$a = \left(\frac{3RW}{8E^*} \right)^{1/3} \qquad \text{Eq. 2.8}$$

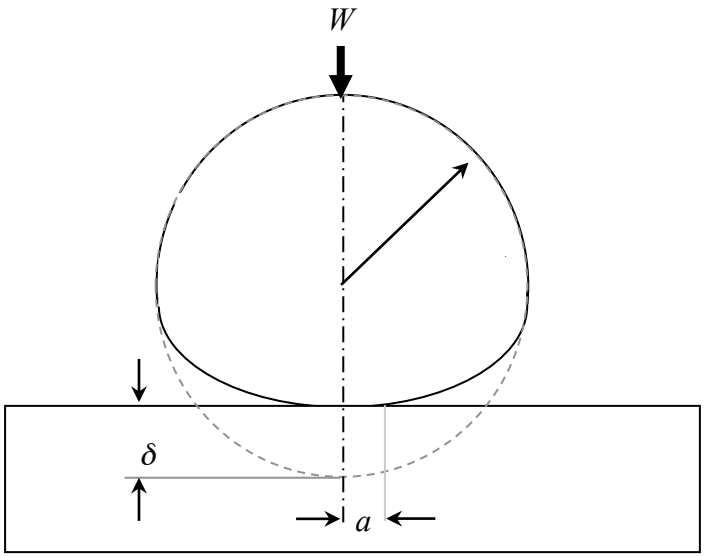

Figure 2.10: In the above sketch is shown the particular case of an elastic ball pressed with a load W against an un-deformable plane. The circular contact surface has radius 'a' while 'δ', describes the deformation.

For any two contacting bodies, the contact area can be calculated knowing the material properties, geometry and load on the system. The radius of the circular contact area between a sphere and a plane, as calculated by Hertz in Eq. 2.8 is shown in Figure 2.10.

The reduced elastic modulus E^*, is calculated considering beside the Elastic modulus of the single materials, also the Poisson coefficient υ, defined as the ratio of the relative contraction (normal to the applied load), divided by the relative extension strain, or axial strain (in the direction of the applied load). Concluding, E^* is defined as follows:

$$E^* = \left(\frac{(1-\upsilon_1)}{E_1} + \frac{(1-\upsilon_2)}{E_2} \right)^{-1} \qquad \text{Eq. 2.9}$$

The deformation δ, shown also in Figure 2.10, in then:

$$\delta = \left(\frac{9W^2}{16E^{*2}R} \right)^{1/3} \qquad \text{Eq. 2.10}$$

leading to an actual contact area of:

$$A = \pi a^2 = \pi R \delta \qquad \text{Eq. 2.11}$$

Where in Eq. 2.10 and Eq. 2.11, the contact area A is directly related to the radius of the ball, elasticity of the two materials constituting the ball and disk and finally to the applied load W.

2.7.2. The lubricant properties

The other side of *EHL* regards the fluid dynamic properties, which together with the equations describing the elastic contact, allow for a complete mathematical description of the lubrication mechanism.

The element of fluid that is enclosed between two moving solids is subject to stresses along the three Cartesian directions. In the specific conditions for which the flow is parallel to the walls, the fluid obeys a simplified mass and force balance that takes into account the symmetry of the system and the preferential direction of movement of the enclosed fluid. The mass flow induced by the pressure drop caused by the moving planes, in conjunction with the

continuity equation describes the flow in the *EHL* regime and is defined by Eq. 2.12, also known as the Reynolds equation, first derived it in 1886.

$$\frac{\partial}{\partial x}\left[\frac{h^3}{\eta}\frac{\partial p}{\partial x}\right]+\frac{\partial}{\partial y}\left[\frac{h^3}{\eta}\frac{\partial p}{\partial y}\right]=6h\frac{\partial}{\partial x}\left(U_1+U_2\right)h+6\left(U_1+U_2\right)\frac{\partial h}{\partial x}+12\frac{\partial h}{\partial t} \qquad \text{Eq. 2.12}$$

In Eq. 2.12, h is the film height, η and ρ are respectively the dynamic viscosity and the density. The right hand side of the Reynolds equation presents the terms relative to the squeeze and the wedge, in the latter the velocities U_1 and U_2 are relative to the planes. The left hand side term represents the flow due to pressure drop caused by the sliding of the surfaces.

2.7.3. Film thickness calculation

The *EHL* problems consists in resolving an elastic term, due to the deformation of the surfaces under stress, and the hydrodynamic term responsible for the behaviour of the entrapped flow under the elastic bodies.

Depending on the conditions, one effect can become predominant over the other, for instance in systems with very rigid surfaces the elastic deformations can be neglected. Johnson (1970), pioneered the field using semi empirical correlations of the entrained film thickness. Since then, the *EHL* was divided into 4 main regimes, described recently by Guo, Fu *et al*. (2008). The four lubrication regimes, show in Figure 2.11, are:

- *Piezoviscous rigid (PVR): Rigid surfaces / Viscosity rise due to pressure*
- *Isoviscous rigid (IVR): Rigid surfaces / Constant Viscosity vs pressure*
- *Isoviscous Elastic (IVE): Elastic deformation / Constant Viscosity vs pressure*
- *Piezoviscous Elastic (PVE): Elastic deformation / Viscosity rise due to pressure*

It has to be noted that the change in viscosity mentioned above, is not related to non-Newtonian flow behaviour, but to changes of viscosity as a function of pressure. Several orders of magnitude more than the atmospheric pressure are usually necessary, (Bett and Cappi, 1965) and with exception for mechanical applications such as metal bearings, these conditions are hardly established.

These different regimes of lubrication have drastically different film thicknesses, for instance in the *PVE* where the elastic deformation and the pressure-viscosity effects are equally important, (relevant for metal bearings that operate under typical stresses of 3 *GPa*) the minimum lubricant film thickness hardly exceeds 0.1 μm (Hamrock, 1994). *IVE* (also called *Soft-EHL*) relates to materials with low elastic modulus, such as rubber and no viscosity change due to pressure, in these conditions the semi empirical correlations all agree on a film thickness of the order of few micrometres.

The most important criteria for determining the success of the lubrication of a contact is the size of the minimum film thickness. Dowson and Higginson (1959), were the first to derive numerically the equation to describe the film thickness by differentiating the Reynolds equation, proposed in Eq. 2.12. Based on their work Johnson (1970), refined a semi-empirical dimensionless correlation, using three dimensionless groups. Eq. 2.13 is a modified formula for calculating the minimum film thickness as proposed by Halling (1975).

$$h \Big/ \frac{4.9\eta UR}{W} = B\left[\frac{1}{\alpha} \Big/ \frac{0.2W^{3/2}}{(\eta U)^{1/2}R}\right]^{a}\left[\left(\frac{WE^{*}}{\pi R}\right)^{1/2} \Big/ \frac{0.2W^{3/2}}{(\eta U)^{1/2}R}\right]^{b}$$

$$\frac{ehl\ film\ thickness}{rigid\ isoviscous\ film\ thickness} = B\left[\frac{pressure\ increase\ by\ viscosity}{\max imum\ rigid\ isoviscous\ pressure}\right]^{a} \qquad \text{Eq. 2.13}$$

$$\left[\frac{\max imum\ herzian\ pressure}{\max imum\ rigid\ isoviscous\ pressure}\right]^{b}$$

Eq. 2.13, is applied to all the four regimes identified by Figure 2.11, by modifying the exponents in function of the physical of the conditions of pressure and deformation considered.

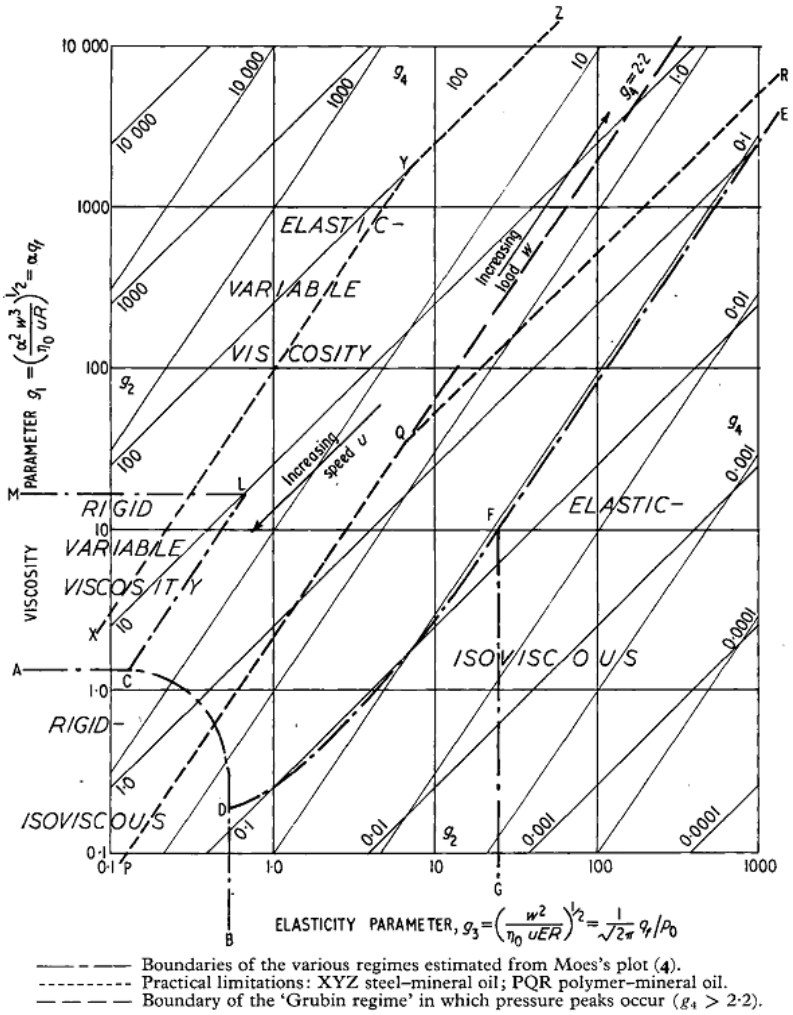

Figure 2.11: Subdivision of the EHL in 4 different regimes. IVR described by the line ACDB; PVE described by MLCQR, PVR described by ACLM and the remaining portion of the graph is IVE (Johnson, 1970).

2.7.4. The dynamic friction coefficient: Stribeck Curve

Richard Stribeck in 1908, while studying the lubrication mechanisms in metal bearing, observed that the friction coefficient is not linear with velocity, but decreased to a relative minimum, to only increase again for high velocities.

These findings were summarised by Stribeck in a diagram, the Stribeck curve, used to explain rubbing phenomena occurring in lubricated contacts. In this diagram, the friction is plotted against a dimensionless group known as the Sommerfeld Number or bearing characteristic number, N_{So}, shown in Eq. 2.14. In this group, η represents the fluid viscosity, U is the relative speed and W is the normal load.

$$N_{So} = \frac{\eta U}{W} \qquad \text{Eq. 2.14}$$

For high values of N_{So}, the friction coefficient increases linearly on a double logarithmic plot with increasing N_{So} (Figure 2.12, Zone III). A change in the Sommerfeld number, either as a result of an increase in W, or a decrease in U results in a decrease in the friction coefficient. According to the Reynolds equation proposed in Eq. 2.12, the build up of the pressure in the gap, decreases and the fluid film becomes thinner, limiting the viscous dragging forces created by the fluid, consequently resulting in a decrease friction coefficient. For even smaller values of $\eta U/W$, fluid film thickness is further reduced, and increasing contact areas between the asperities of the two surfaces increase, due to the high load and low velocity. This contact becomes more pronounced as the fluid abandons the gap with a consequent rise in friction. This can be seen in Zone II of Figure 2.12 known as the mixed lubrication regime, where the friction coefficient increases as the N_{So} decreases. Further reduction in the $\eta U/W$ factor, completely depletes the gap from the lubricant, allowing for the

only surface-to-surface contact to occur (Figure 2.12, Zone I). This zone, is often referred to as boundary lubrication, since the friction coefficient is predominantly a function of the surface properties of the two contacting bodies.

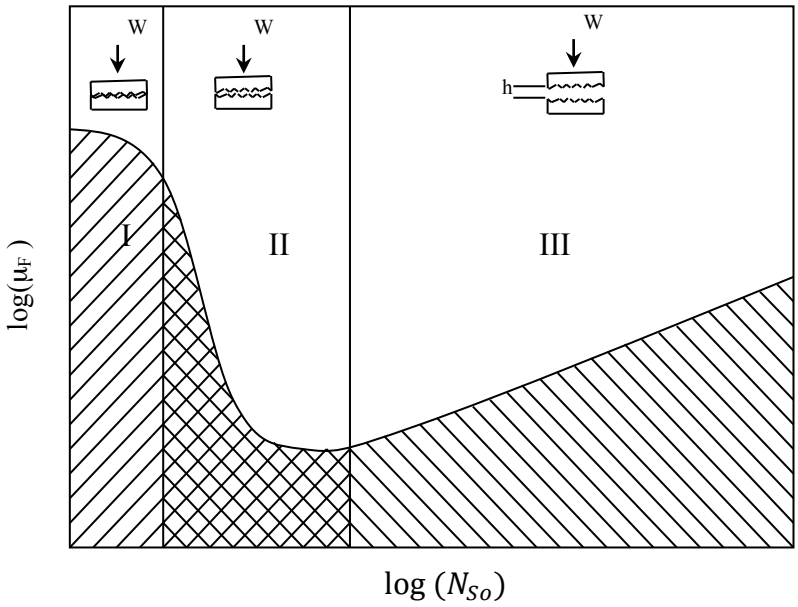

Figure 2.12: Typical stribeck curve, where the friction coefficient μ_F is a function of the Sommerfeld Number (see text). In the graph, three zones can be clearly identified. Zone I shows the boundary lubrication regime, for sliding surfaces in direct contact, lubrication is given by the surface properties. Zone II is known as mixed regime, in this zone, the hydraulic pressure separates the two surfaces, and the friction decreases. In Zone III, the sliding walls are fully separates, by the hydrodynamic pressure. The friction increases due to viscosity of the fluid.

2.7.5. Skin Lubrication and Tribology

A wide range of products from the food and health care industries, consist of highly packed suspensions of particles with characteristic dimensions that range from the micro to the milli-scale. For instance, in a variety of food products, the morphology of these particles and their size distribution can be significantly altered during the mastication process, where the bolus is created and, squeezed and deformed between the tongue and the palate generating a friction force. The lubrication offered by particle pastes is poorly studied, and lubrication in general has only recently entered in the group of the physical properties that relate to sensory

perception. Malone, Appelqvist *et al*. in 2003, using a modified Mini Traction Machine and a trained sensory panel, were the first to correlate mixed regime of lubrication to the complex sensory oral perception (Malone, Appelqvist *et al.*, 2003). Since then, several authors have looked at extending the classical tribological understanding of lubrication to the relevant in mouth processes, involving the rubbing and squeezing of the product between tongue and palate. The initial fluids tested were Newtonian (de Vicente, Stokes *et al.*, 2005) and later shear thinning solutions (de Vicente, Stokes *et al.*, 2005). However, because of the heterogenousity of the fluids in the mouth during mastication, due of their particulate nature, other authors have looked at the lubrication of particle suspensions to understand the friction upon swallowing, where interaction between the particles and the oral surfaces is further promoted. These particles interactions have been reported in specific conditions to relate to the perception of creaminess (Guinard and Mazzucchelli, 1996; de Wijk and Prinz, 2005).

More in the general, in the case of a compliant contact considered to be isoviscous elasto-hydrodynamic lubrication with the skin, becomes apparent the importance of understanding how the body interprets the lubrication induced by the particles in the system and also how these affect lubrication phenomena (de Wijk and Prinz, 2005)

Particularly for a food product formulation with desired characteristics, this involves also the understanding of how food breaks down in the mouth due to mastication, or particle contact with the oral tract. Prinz and Lucas (2000) studied the effects of tannin–proline–rich proteins interactions on the lubricating properties of saliva, concluding that the precipitation of proteins by tannins reduce the ability of saliva to act as a lubricant and decrease its viscosity, with a direct effect on the in-mouth feeling perceived as grittiness (Prinz and Lucas, 2000; Engelen, Schipper *et al.*, 2005). Also extensively reported by Imai, Hatae *et al*. in 1995 and Imai, Shimichi *et al*. in 1996, in which they addressed as one of the predominant factor,

the particle size in contributing to the perceived grittiness. The importance of understating soft particle lubrication phenomena in relation to mouth-feel was recently strongly stressed by Engelen, Schipper *et al*. (2005). The authors underlined a strong dependence between particle size and texture perception, but also noted that the main mechanism leading to an increased sensation of roughness and decreased sensations of, for example, fattiness and creaminess was an overall increase in friction.

The scientific principles behind skin lubrication are identical to those controlling the in-mouth tribology. However the friction offered by the skin differs from the one earlier described for the mouth. The differences are purely related to attributes of the surface of the skin such as the skin elasticity and roughness. The skin elasticity is different due to the presence of bones, which will play an important role by changing the deformability of the epidermis as well as the skin roughness. It is nonetheless fairly simple to measure an average friction coefficient for the human skin, and it is typically 0.7 (Adams, Briscoe *et al.*, 2007).

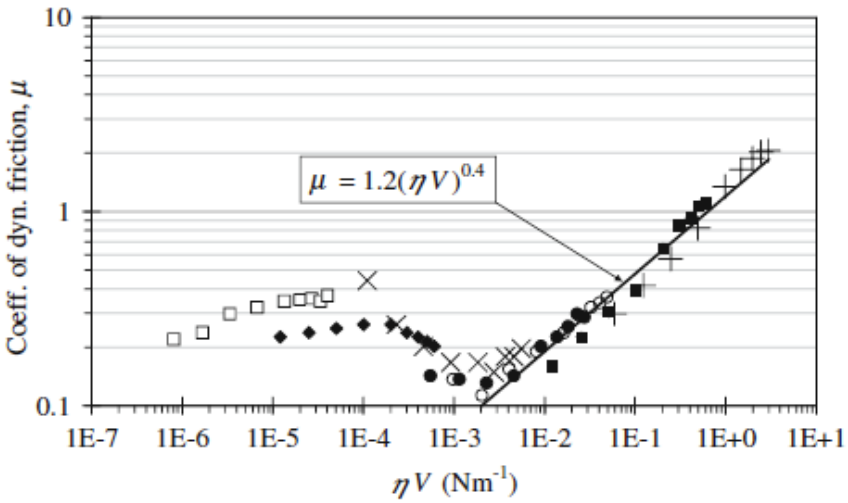

Figure 2.13: Stribeck Curve obtained by sliding a glass probe on the inner skin of the arm. Normal load applied was 0.2 N. The different data sets represent the various liquid viscosities tested. All fluids were Newtonian (Adams, Briscoe et al., 2007).

The skin friction under lubricated conditions, complies with the soft – EHL regime because of the deformability of the surfaces. Many studies have tried to capture, the friction

profile of the skin lubricated by different fluids, in different load conditions. The classic representation of such study is the Stribeck curve, in Figure 2.13.

The use of the Stribeck curves with semi empirical correlations provide a good set of information on the lubrication mechanism. A master curve can be obtained by normalizing the disk velocity by the friction coefficient as shown in Figure 2.13. As mentioned earlier this is possible because the mechanism behind the lubrication in this regime are purely hydrodynamic, and therefore controlled solely by the fluid viscosity. The friction in the boundary regime is however always very similar to the one of dry skin. More complex fluids, such as shear thinning biopolymer solutions, only show the same master curve behaviour at very high relative entrainment speeds, for which the shear forces in the gap are high enough to produce a constant viscosity, sometimes referred to as infinite shear viscosity, η_∞ (de Vicente, Stokes *et al.*, 2005).

Chapter 3.

EXPERIMENTAL

3.1. Introduction

This chapter has an underlying subdivision into two main sections. The initial "*Materials*" section includes a description of the chemical compounds used in the experiments and their preparation. The second section includes the methodology followed in this thesis. An accurate description of the programming codes written to analyse the *PEPT* data and their aim is also included.

To facilitate the reader, the layout of the paragraphs in this chapter mimics, where possible, the order in which the results are later on presented.

3.2. Materials

3.2.1. Biopolymer solutions

The aqueous phase for the preparation of all the aqueous solutions was distilled water.

3.2.1.1. K -carrageenan

κ-carrageenan obtained from Sigma-Aldrich (UK) was used with no further purification or modification of its properties.

3.2.1.2. Agar

The fluid gel produced and tested during the study of the fluid dynamics of the Pin Stirrer was formulated from Agar obtained from Sigma-Aldrich (UK). This biopolymer was diluted into an aqueous solution with concentration of 2% in weight in agar with no further purification or modification of its properties.

3.2.1.3. Agarose

The Agarose fluid gel was prepared from solutions was Agarose type I-A, with low EEO; supplied by Sigma Aldrich (UK). The agarose provided was used with no further purification or modification of its properties. All agarose solutions were prepared using distilled water.

3.2.2. Glycerol

The glycerol was purchased by Sigma Aldrich (UK), with purity > 99% and used as it was supplied with no further purification. The glycerol/water solution for the *PEPT* experiment was prepared from distilled water. The solution was stirred for 24*hr* before the use in a hermetic vessel at a temperature of 25 ℃ to allow complete dispersion.

3.2.3. Potassium Cloride

The potassium chloride (KCl) was purchased by Sigma Aldrich (UK), with purity > 99.99% and used as it was supplied with no further purification.

3.3. Methodology

The paragraphs in this section are organized according to the order in which they are discussed in this work. All the biopolymer solutions used throughout this work were produced on the day of the experiment. The solutions were produced by firstly heating distilled water to approximately 50°*C* on a magnetic hot-plate stirrer; the addition of the biopolymer powder to distilled water was followed by a magnetic agitation. The use of any preservative was considered unnecessary due to the short life of the samples.

3.3.1. Kinetic studies of bio-polyelectrolyte fluid gels

3.3.1.1. κ-carrageenan fluid gel production

The solutions for the production of carrageenan fluid gels were prepared by dissolving the required amounts of κ-carrageenan and KCl in distilled water at 70 °*C* (≈40 °*C* above the gelation temperature, Figure 2.3); solutions were continuously mixed by a magnetic stirrer in a sealed-top flask to avoid evaporation. Details of the concentration of κ-carrageenan and KCl in the fluid gels are given in Table 3.1.

	γC_p [meq l^{-1}]	C_s [meq l^{-1}]	C_T [meq l^{-1}]
0.5 $\%_{w/w}$ κ–carrageenan	6.3	13.6	20
1 $\%_{w/w}$ κ–carrageenan	12.6	7.0	20
2 $\%_{w/w}$ κ–carrageenan	25.2	-	25.2
3 $\%_{w/w}$ κ–carrageenan	37.8	-	37.8

Table 3.1: Concentration of κ–carrageenan and KCl in the fluid gels.

All investigated κ-carrageenan fluid gel systems were produced, from their respected "primary" solutions, in a rheometer under controlled conditions of torque (refer to section 3.3.1.2, for rheometer configuration and set-up). This approach allows for the precise control of the rate of cooling as well as the applied rate of shear, which determines the structure of the produced systems. Both process variables were varied during experimentation, with the applied cooling rate ranging from 0.5 to 6 °*C* min^{-1} while the applied shear rate was varied from 0.5 s^{-1} to 700 s^{-1}.

3.3.1.2. Rheometer configuration and set-up

κ-carrageenan fluid gel production and rheological measurements (both during and after fluid gel production) were carried out in a Gemini HR nano stress-controlled rheometer using a 4° truncated (truncation of 150 *μm*) cone (40 *mm* in diameter) and plate geometry.

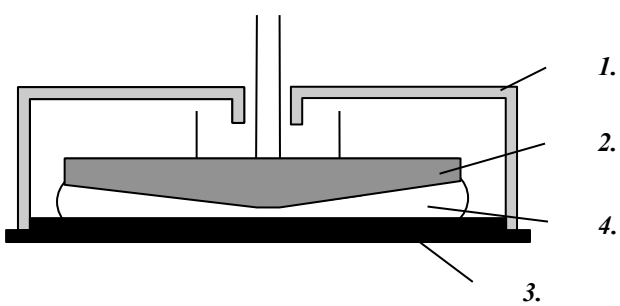

1. ***Humidity Trap***
2. ***4° Cone 150 μm Truncation***
3. ***Temperature Controlled Plate***
4. ***Fluid Gel***

Figure 3.1: Cone plate geometry with humidity trap limiting the evaporation.

The used cone and plate geometry was chosen since it provides a well-defined and uniform shear field during experimentation. All experiments were carried within a "humidity trap", illustrated in Figure 3.1, to reduce evaporation, while the volume of the samples used for all the measurements was kept constant at 1.25 *ml* in order to be consistent and obtain reproducible data. The fact that the measured samples form a very thin layer that is in contact with the heated plate of the rheometer, ensures that the temperature or temperature change (for the cooling rates used in this study) induced by the instrument is promptly "experienced" by the sample itself.

The rheology of the fluid gels produced via gelation in the pin stirrer, namely agar and agarose, were tested using the vane geometry. This was necessary in order, to prevent the slip of the fluid against the geometry caused by the higher viscosity. Although the temperature during testing was maintained constant at 30 *°C*, 4 *°C* higher than the room temperature; nevertheless a humidity trap was used to prevent evaporation.

3.3.1.3. Particle size determination

Accurate measurement of the size of the produced fluid gel particles was very difficult due to the small dimensions of the particles and also because of the similarity between their refractive index and that of the suspending medium. For these reasons the size of the particles was determined from images obtained using an optical microscope (Leica DMRBE, Leica Microsystems Imaging Solution LTD) equipped with a camera (3CCD, Colour Vision Camera Module, Donpisha) for micrograph acquisition. Length scales on the obtained micrographs were calibrated using micrometer-scale graticules, which gave a conversion factor of 7.33 $pix\ \mu m^{-1}$. The dimensions of the particles in the micrographs were then measured in pixels using public software ImageJ (NIH, *Maryland*, *USA*) and using the calibration these were then converted into μm units. Samples were taken from the fluid gel systems under investigation and these were diluted in 0.1% in weight of KCl solution (by a factor of 2:1) in order to clearly observe individual particles and therefore obtain a good estimate of their size. To increase the contrast of the obtained micrographs, 200 *ppm* of the cationic dye methilen blue was added to each of the sample.

3.3.1.4. Viscosity increase during fluid gel production

The rheological data, obtained during the production of the fluid gel systems, were used to calculate the increase in viscosity ($\Delta\eta$) between ordering initiation and completion of the fluid gel structure. Figure 3.2 shows an example of the obtained raw data (viscosity against temperature) were three regions can be clearly identified; these are the stage before the onset of ordering (region A), the stage between ordering initiation and ordering completion (region B) and finally the stage after ordering has been completed (region C). Linear regression on the data in each region gives three straight lines (Figure 3.2).

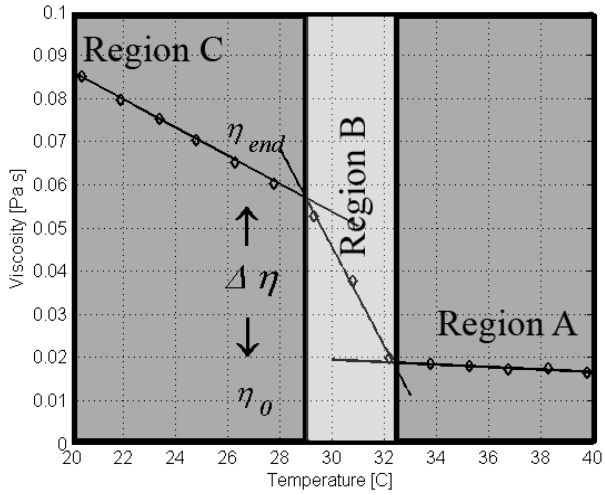

Figure 3.2 Raw rheological data and linear regressions to calculate the viscosity increase ($\Delta\eta$) between ordering initiation and completion during fluid gel production.

The two points at which these lines intersect were calculated and each represents a single value of viscosity for the onset (η_o) and end (η_{end}) in the ordering process (Figure 3.2). The viscosity increase ($\Delta\eta$), during the ordering process, is then calculated as the difference between the values of these two points; $\Delta\eta = \eta_{end} - \eta_o$.

3.3.1.5. Study of the microstructure recovery

Two different tests were done, in order to explore the nature of the interactions between particles occurring during fluid gel production, and in the immediate instants after particles are formed. Both the investigations on the aging of the microstructure of the produced fluid gels were dynamic in nature in order to quantify the extent of structuring in time.

3.3.1.5.1. Microstructure ripening

The fluid gels tested were produced under controlled conditions of shear and temperature in the rheometer; according to the method described earlier. The ripening test begun in the immediate instants after the fluid gel formation; once the shear was stopped and the temperature reached 20 *°C*. The structural ripening was measured from this point onward, by monitoring the profile in time of the elastic modulus *G'*, when a sinusoidal stress with amplitude of 10 *mPa* and frequency of 1 *Hz* was applied. The viscoelastic modules measured represent the changes in the structure under the assumption that a stress of 10 *mPa* does not affect the structure's aging process.

3.3.1.5.2. Strain – recovery test

The elastic (*G'*) and viscous modulus (*G''*) were measured before and after a stress ramp applied in order to fully "break" the bonds between the particles by plastically deforming the structure. The two fluid gels examined have the following characteristics:

- *0.5% κ–carrageenan cooled at 1 °C* min^{-1} *with an imposed shear rate of 5* s^{-1}
- *0.5% κ–carrageenan cooled at 6 °C* min^{-1} *with an imposed shear rate of 100* s^{-1}

The recovery was allowed to occur over a "rest" time of 15 minutes and immediately afterwards a second stress sweep was performed. Both stress sweeps reached amplitude of 12 *Pa*, with constant frequency of 1 *Hz*.

3.3.2. Positron Emitting Particle Tracking Experiment

3.3.2.1. The pin-stirrer

The mechanical drawing of the model pin stirrer used in this work is shown in Figure 3.3. The pin stirrer operates as a continuous unit, with inlet on the bottom side, while the outlet in centred on the top wall aligned with the shaft. The rotating shaft has a diameter of 15 *mm* with 16 pins mounted as shown in Figure 3.3. The stationary frame possesses 16 stationary pins with 180 degrees symmetry mounted inwards, to break the flow against the rotating pins and increase the anisotropy of the flow field. The smallest gap between the stationary pins and the rotational pins is approximately 3 *mm* and is found when the rotating pins pass between the stationary pins. In this specific position the shear rate can be estimated for a rotating velocity of 900 *rpm* to be approximately ~600 s^{-1}, meanwhile the highest shear is expected to be found in the small region of swept volume between the rotating pins and the outer wall, the shear in this region can be estimated to be ~1200 s^{-1}. This indicative value of shear rate can be used to verify further calculations on the shear field.

The free volume within the pin stirrer is an important parameter for the characterisation of the system and it has been measured by flooding the pin stirrer with water. The internal free volume, measured was 158 *ml*, while the free volume of the heating jacket calculated from the dimensions in Figure 3.3 is equal to 181.40 *ml*.

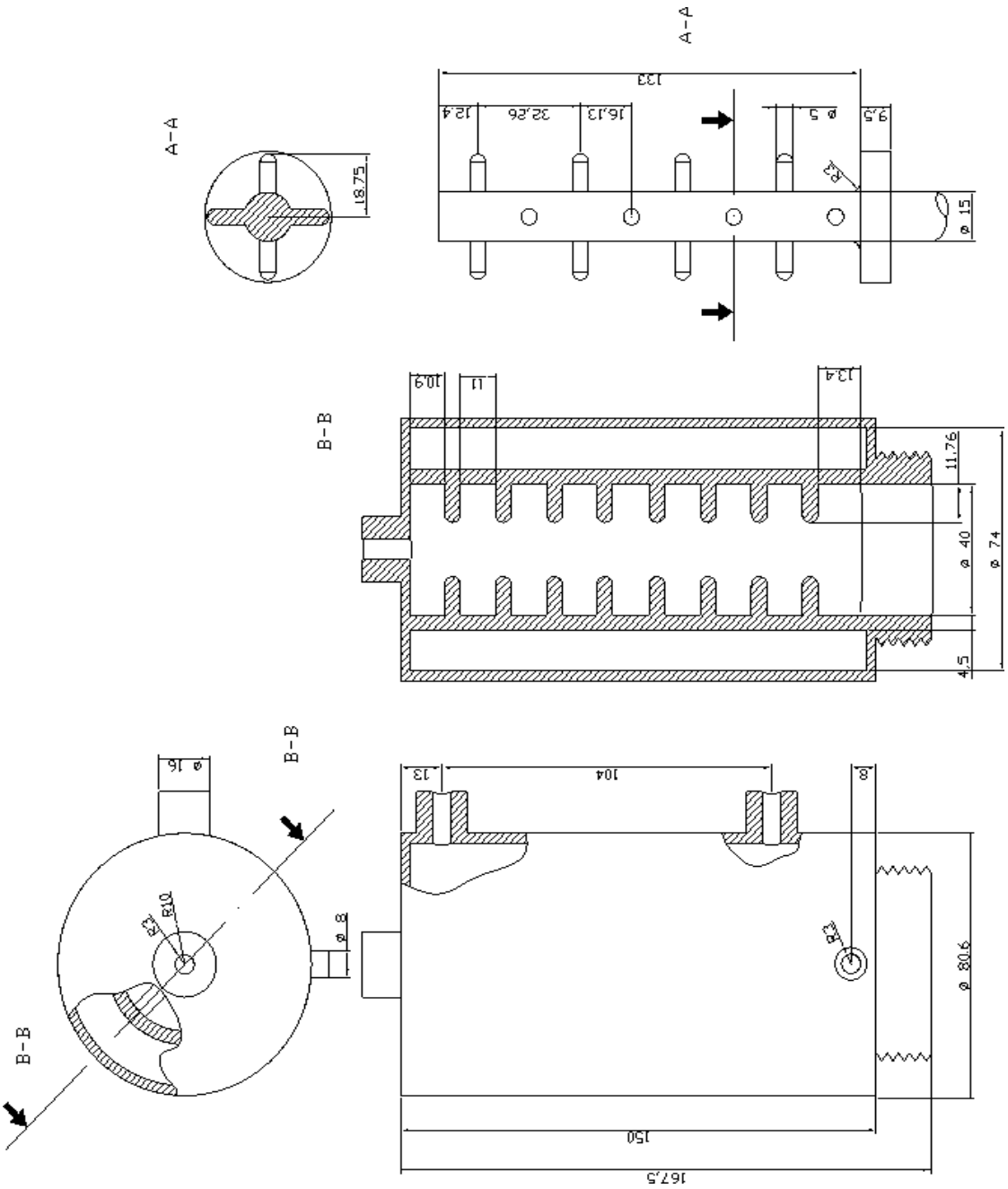

Figure 3.3: Mechanical drawing of the pin stirrer. Units are expressed in mm

3.3.2.2. Set-up

For comparison throughout all the experiments carried out in this work, the same experimental set up was consistently used. The set-up and all its components are described in the schematic of Figure 3.4.

The biopolymers are dissolved in distilled water on the hot plate magnetic stirrer, maintaining the temperature of the biopolymer solution above the melting point of any of the biopolymers investigated (approximately at 95±5 *°C*) for 20 minutes, under continuous agitation. The use of a lid prevented the water evaporation from the flask at this stage and for the whole experiment.

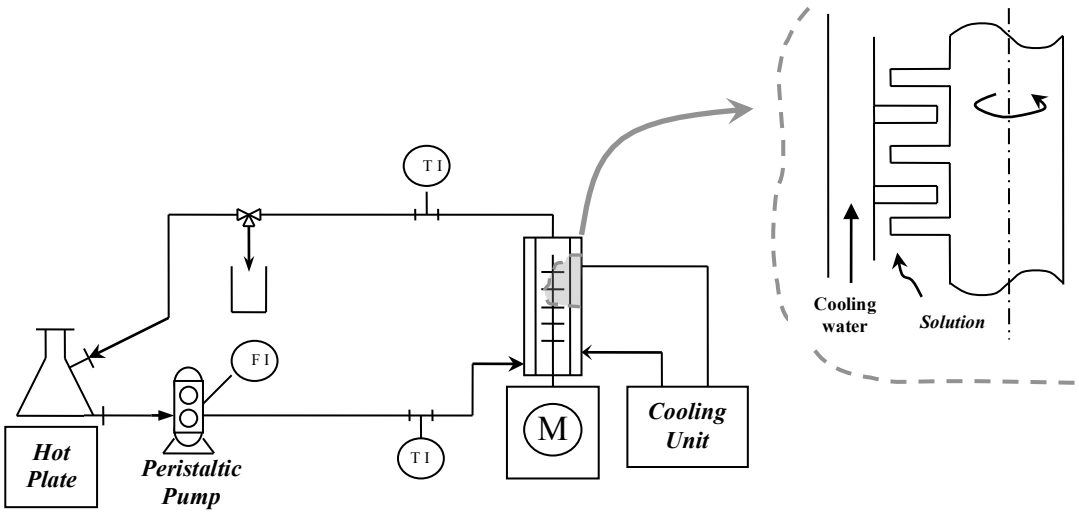

Figure 3.4: Experimental set-up for the production of fluid gels with the pin stirrer heat exchanger.'TI' are the temperature indicator, while with 'FI' is indicated the flowmeter.

Consequently, after the biopolymer completely dissolved on the hot plate stirrer, the solution was pumped thought the system with the aid of a peristaltic pump, as shown in the schematic of Figure 3.4. The pump used was a Master Flex L/S purchased from Cole-Parmer Instruments Ltd (UK). The flow rate was set at 10 $ml\ min^{-1}$.

The reduction in temperature, necessary to induce the gelation of the biopolymers under shear, was obtained by connecting the cooling jacket which covers the pin-stirrer (extract in

Figure 3.4 and Figure 3.3) to a cooling unit set at the constant temperature of 25 °*C*. The temperature at the inlet and outlet of the pin-stirrer was measured by thermocouples (in Figure 3.4 indicated as *TI*).

The internal volume of the pin-stirrer measured in the previous section and approximately equal to 158 *ml*, for a constant flow rate of 10 $ml\ min^{-1}$ guarantees an average residence time of 16 *min*. This average residence time proved sufficient to nullify the effect of the internal fluid dynamic conditions, on the outlet temperature. In other words, changing the shaft rotational speed has no effect on the outlet temperature for the range of velocities considered in this work (*i.e.* see Table 3.2).

Immediately after the start of the pump, the system is in non-steady state condition. The temperatures of the inlet biopolymer and outlet fluid gel require time to stabilise. In order to improve the reproducibility of the results and compare across different samples, any time dependencies had to be reduced to a minimum. For this reason prior to opening the valve for the collection of the sample, the solutions from the hot plate were pumped into the pin-stirrer and initially circulated in a closed loop (hot-plate → pin-stirrer inlet→ pin-stirrer outlet → hot-plate) until the temperatures at the pin-stirrer inlet and outlet were equilibrated at the required temperatures (*i.e.* see Table 2.1). Re-circulating the system for a time equal to three times the average residence time was found to be an adequate period for equilibrium to occur.

Material	T_{in} *[°C]*	T_{out} *[°C]*	*Cooling Unit Temperature [°C]*	*Flow Rate [ml min^{-1}]*	*Shaft Speed [rpm]*
Glycerol	*25*	*25*	*25*	*10*	*900*
2% Agar	*46*	*26*	*25*	*10*	*900*

Table 3.2: Set up parameters for the PEPT experiment.

3.3.2.3. Radioactive Tracer in PEPT experiments

The tracer used in this study was ^{18}F-labelled. A solution of ^{18}F was obtained by irradiation using the 33*MeV* ^{3}He beam from the University of Birmingham Radial Ridge Cyclotron by the reactions $^{16}O(He, p)^{18}F$ and $^{16}O(^{3}He, n)^{18}F$. A water solution of radioactive ^{18}F was allowed to diffuse through a 400μm inactive tracer made of porous resin by immersion (Parker, Broadbent *et al.*, 1993). The molecules of ^{18}F are chemically very similar to their stable isotope and soluble in water (1.69 $mg\ l^{-1}$). The use of a tracer containing a solution of ^{18}F in any polar medium would inevitably lead to a leakage of the radioactive solution from the tracer, invalidating the measure. For this reason, its use in water and more generally in any polar solvent is precluded unless coated with paint.

Various tests have been done experimenting on different coating thickness. The tests were aimed to assess if the rigidity of the paint coating was sufficient to withstand the stresses within the pin stirrer. The final tracer diameter including the coated layer used in both the experiments was 700 μm. The tracer original activity was slightly different for each tracer but approximately 0.4 *Cu*.

3.3.2.4. γ − ray detectors

The detectors, as shown by Figure 3.5 consist of ADAC Forte with MCD coincidence option to side γ-detectors, able to move and rotate along the y-axis. The detection system consists of two gamma camera heads on a motorised gantry, which permits rotation about a horizontal axis, and adjustment of the face-to-face separation of the detectors from 250 *mm* to 800 *mm* (Parker, Forster *et al.*, 2002).

Figure 3.5: The pin stirrer within the PEPT cameras

3.3.2.5. Initial PEPT Data analysis and Centring

The pin-stirrer is a continuous unit, where the solution of the biopolymer is constantly driven by the pump in the bottom inlet and collected form the top exit. The tracer is injected 1cm before the inlet at the bottom of the pin stirrer and collected without stopping the pump. In order to have a comprehensive and accurate measurement it is important that the tracer covers the largest possible volume within the Pin-stirrer. For this reason multiple runs were necessary for each experiment.

Two *PEPT* experiments were done with the fluid gel and glycerol. The tracer resulted active over enough time to allow for several passes for each fluid. Table 3.3 contains the detail of the length of the runs of glycerol and fluid gel. Particular attention should be paid to the 4th column denominated *locations/seconds.* In this column the ratio between the number of

location in each run over the relative *run length* expressed in the *3rd* column defines an average time resolution for each run.

Fluid	*Run Number*	*Run Length*	*Locations/ Second [Hz]*	*Total Test Time*
	1	*4min:27s*	*143*	
	2	*6min:27s*	*129*	
	3	*25min:16s*	*126*	
Glycerol	*4*	*11min:34s*	*121*	*1hr:12min:54s*
	5	*1min:59s*	*109*	
	6	*5min:34s*	*112*	
	7	*14min:38s*	*113*	
	1	*11min:49s*	*152*	
	2	*9min:12s*	*137*	
	3	*3min:6s*	*135*	
	4	*11min:39s*	*135*	
	5	*23min:54s*	*123*	
	6	*27min:53s*	*99*	
Fluid Gel	*7*	*20min:33s*	*97*	*5hr:28min:40s*
	8	*38min:14s*	*80*	
	9	*52min:37s*	*65*	
	10	*43min:20s*	*50*	
	11	*9min:41s*	*40*	
	12	*1hr:9min:30s*	*32*	

Table 3.3: Details relative to the runs constituting each experiment.

The time resolution, expressed as *locations/seconds,* diminishes after each run, according to the theoretical half-life of the radioactive isotope constituting the tracer. Over the total test time needed for the experiment, the decreasing radioactivity of the tracer produces a lower time resolution. In order to maintain an acceptable number of locations and a high temporal resolution, only the first 7 runs were considered.

During each of the runs the tracer looses its original activity according the following exponential law:

$$A = A_0 \exp(-\lambda t)$$
$$\lambda = \frac{\ln(2)}{t_{1/2}} \qquad \text{Eq. 3.1}$$

Where A is the activity function of time t, A_0 is the initial activity, and the tracer half-time life is $t_{1/2}$ (109min for ^{18}F). The time used to plot the experimental points in Figure 3.6, is the cumulative sum of the values reported in Table 3.3 for glycerol. The time as calculated this way does not take into account the experimental time needed to collect the tracer form the outlet of the pin stirrer and repeat the injection in the inlet for the following run (*see Section 3.3.2.3*). The slight discrepancy between the theoretical decay curve in Figure 3.6 and the experimental points is thus minimum.

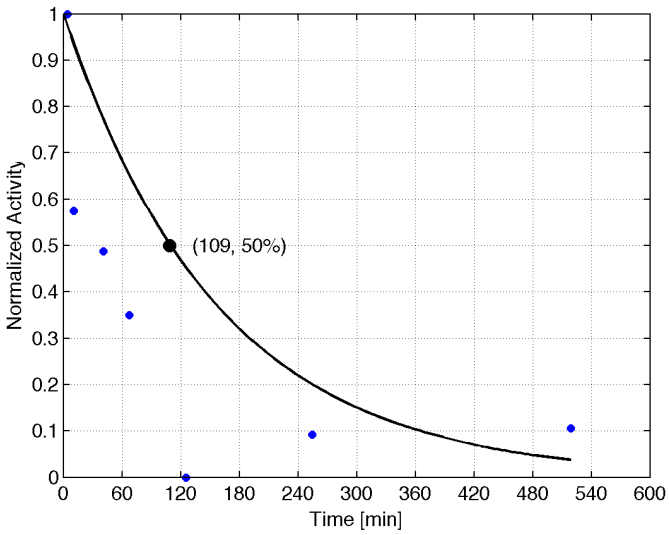

Figure 3.6: Experimental activity of the tracer through-out the glycerol experiment. The continuous line refers to the theoretical decay described by Eq. 3.1

3.3.2.6. Error minimization

The algorithm developed by the Department of Physics of the University of Birmingham and described in Chapter 2, localizes the position of the tracer over subsets of events. The process of extrapolating a single *x,y,z,t*-location from a set of events measured experimentally implies that an error is produced. The error is described by the standard deviation and is reported as a result of this early processing in the final file. The error can be interpreted to be the size of the cloud of uncertainty in which the tracer is situated.

The error is function of many experimental parameters, including the tracer activity, distance between the detector cameras, velocity of the tracer, thickness and density of walls and up to some extent, the unavoidable background radiation. The effect of these sources of inaccuracy on the measure has been adequately addressed and described in the experimental section. Once all these necessary precautions concerning data acquisition have been taken, the issues regarding the error minimization only concerns the early stage of the data analysis. At this point, producing higher quality data depends solely on the two main parameters, the percentage of the original set of events considered for the final identification of the location (f_{opt}) and the Number of Events (N_{events}). The algorithm developed by the department of Physics of the University of Birmingham, divides the complete set of events recorded by the cameras, into *"Data slices"*. The algorithm iteratively calculates the minimum of the trajectories within each *"slice"* and at the end of each iteration disregards the worst trajectories, until only a portion, f_{opt} of the original set is retained. The final location is thus calculated over $f_{opt}\, x\, N_{events}$ trajectories.

Subdividing the data set into smaller slices has the advantage of producing more *x,y,z*-locations, meaning a higher temporal resolution, but without an adequate choice of f_{opt}, the spatial error, given as said by the standard deviation of the events, would rise. Ideally, and only secondarily to the reduction of the error, is important to have the minimum number of events per slice, but keeping a statistically significant final value of actual trajectories over which to reconstruct the location. These general considerations apply to any *PEPT* experiment, but the values of f_{opt} and *Number of Events* vary from system to system. Figure 3.7 shows the result of the trial and error system adopted to quantify the error resulting from changing these two parameters, the over imposed curves describe the number of final trajectories actually used for the reconstruction of the location.

The error varies from 7*mm* for f_{opt} equal to 0.4 and 350 events; to 0.37mm for the same group of events when only the best 0.025 of the total events (f_{opt}=*2.5*) are considered, resulting in 9 trajectories per location. The final number of trajectories per location was also considered and selected to be no smaller than 10, in order to guarantee a reasonable statistical significance. The entire data set was processed setting as a limiting condition an error of 1 *mm* calculated over 10 events. From Figure 3.7,this corresponds to a value of f_{opt} of 6.0 and 170 *Events*.

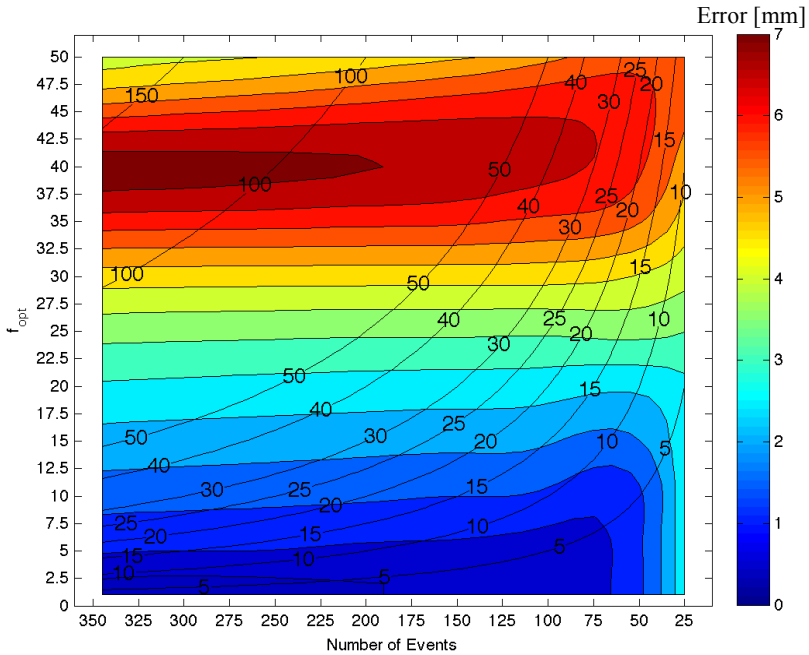

Figure 3.7: Location error map function of the changes in f_{opt} and Number of Events. The over imposed isocurves describe the final number of events used for the calculation of the location. The error is expressed in mm.

3.3.2.7. Digital data centring

The origin of the *PEPT* coordinate system, as described by the Figure 2.9, is situated in a corner of the left hand side detector. The coordinates will therefore need to be centred before proceeding with any further calculations.

The successful recording of an event depends on the trajectory of the back-to-back γ-rays. The detectors need to be hit by both the γ-rays produced by a single annihilated positron. Since the γ-rays are emitted randomly in every direction, but the detectors only cover a small portion of the space surrounding the system, it's possible to described with a three dimensional probability density function the likelihood of an annihilation to be recorded hypothesising no impediments to the γ-rays (Guida, Fan *et al.*, 2009). Guida, Fan *et al*. (2009) found that for a separation of 400 *mm* between the detectors, the maximum theoretical probability to localize a tracer is equal to 0.45. For instance, the probability drastically decreases to 0.25 by moving away from the centre of the cameras to a distance of 100*mm* from the closest detector.

The probability of recording the trajectory, also defined as geometrical efficiency, is purely calculated from theoretical considerations and will be lower during the experiments. Ideally, assuming the system is perfectly positioned between the two cameras and the stainless steel forming the pin stirrer is of equal thickness, the histogram of distributions of the number of locations of a predominantly rotating tracer over the Cartesian coordinate axis x or y, are described by a bimodal distribution. This circumstance rightfully reduces the centring operation to an arithmetical mean. This is not always the case. The γ-rays emitted by the tracer within the pin stirrer were shielded by two concentric steel walls (inner wall and the external jacketed wall in Figure 3.3), reducing the above-mentioned probability and also the symmetry of the histogram. Furthermore, the discontinuous characteristic of the pin stirrer, with locations recorded also when the tracer is flowing through the pipes, and not only rotating in the pin stirrer, renders the symmetry condition necessary for an arithmetic mean un-applicable. The histograms shown in Figure 3.8, represent a single run, of non-centred raw

data. There are small differences in the two peaks of the bimodal of *xy*-locations, suggesting the introduction of an error by a simple arithmetic mean.

(a) *(b)*

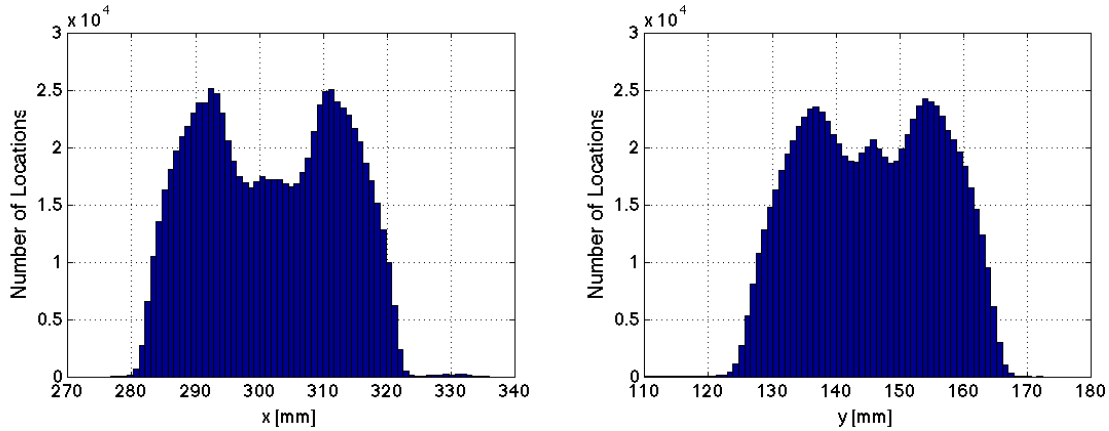

Figure 3.8: Histogram of the locations for the entire PEPT experiment for glycerol. Respectively, (a) shows the x coordinate and (b) the y coordinate.

A rigorous approach to the centring of the coordinate system implies the use of a digital centring algorithm. The code developed (*DigitalCentr.m*) and given in APPENDIX I, divides the *xy*-plane into a fine grid. The tracer path was than over lapped to the grid disregarding the *z*-coordinate. Each time the tracer passed from a cell, the cell value changed from 0 to 1, with the important property of being non-variable over multiple passages. This is equivalent to project the location onto a plane, also suggested by the projection lines shown in Figure 3.9.

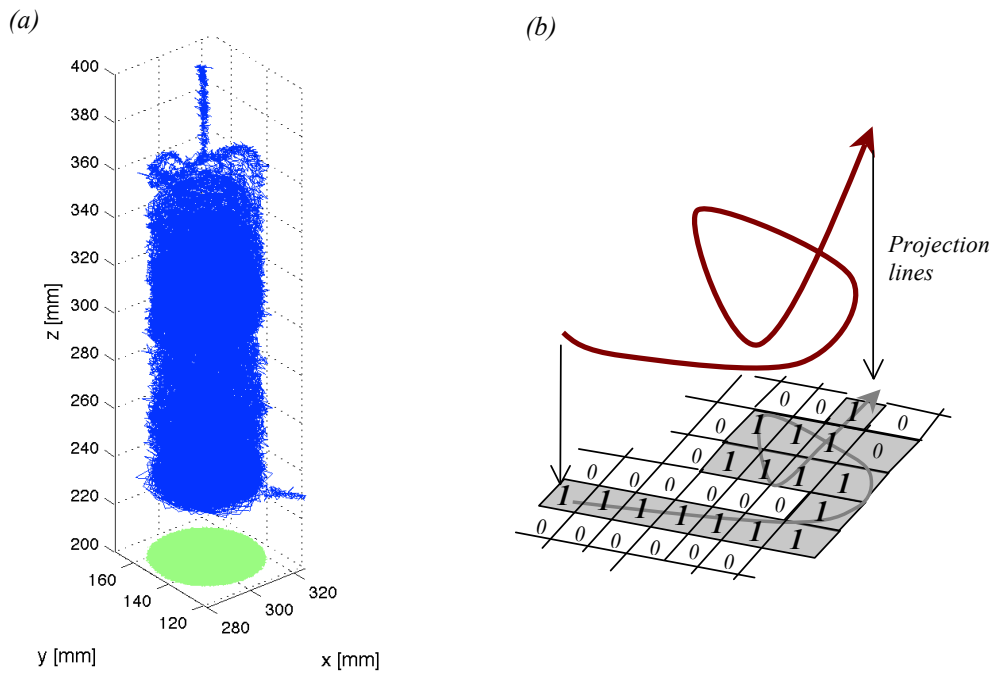

Figure 3.9: Digital centering of the locations. In (a) the result of the projection is a 1/0 map of the entire locations. The sketch in (b) shows the method followed by the algorithm to create the mask.

The centre of the system is taken to be equal to the centre of the circle inscribing all the points of the digital map shown in Figure 3.9. This allows for a computationally light and geometry independent centring. The centring was done independently on each single run of glycerol and fluid gel.

3.3.2.8. Velocity calculation and optimisation

The local velocity can be calculated form *PEPT* data in a variety of ways. The simplest is a two-point differentiation, Eq. 3.2, (Bakalis, Fryer *et al.*, 2004; Bakalis, Cox *et al.*, 2006) carried over the entire data set. A more complex calculation was used by (Fairhurst, Barigou *et al.*, 2001); they used weighted average over 11 points discarding locations with velocity higher than a critical value, both these methods proved effective for slurries of laminar flow. From considerations based on the particle paths, this work adopts a technique proposed for the

first time by Chiti (2007) and further applied by Guida, Nienow *et al*., proved less depend to the *PEPT* localization error for fast moving tracers.

$$v_j(i) = \frac{\left(x_j(i) - x_j(i-1)\right)}{\left(t(i) - t(i-1)\right)} \qquad \text{Eq. 3.2}$$

Where x_j is the *j-th* component of the position vector, and therefore the velocity relative to x_j is v_j. This method is based on finding for each component position the equation of the straight line of 'best fit', which passes across the data set at the location as a function of time, using for the first time the matrix notation of the least square method, Eq. 3.3.

$$\begin{gathered} y = \beta_1 x^{1-1} + \beta_2 x^{2-1} + \ldots + \beta_n x^{n-1} \\ \text{or} \sum_{n=1}^{m} X_{in}\beta_n = y_i \\ \left(X^T X\right)\beta = X^T y \Big| \quad \beta = \left(X^T X\right)^{-1} X^T y \\ v_j(i) = \frac{dy_i}{dt} \end{gathered} \qquad \text{Eq. 3.3}$$

Where β_j are the coefficients of the polynomial of the *n-th* order. The group $\left(X^T X\right)^{-1} X^T$ is also known as Moore-Penrose pseudo inverse, and allows carrying out a computationally expensive operation as inverting the matrix $\left(X^T X\right)$ in a numerically efficient way (*interp3PEPT.m*). From Eq. 3.3 is possible to further derive the average error R^2, for each interpolated point, Figure 3.10.

In order to correctly choose the right approach for the calculation of the velocity, an artificial data set, mimicking the fluid dynamic velocities (ω *=15rps*), the *PEPT* data acquisition rate (*100Hz*) and noise, was used. The mentioned noise or error, was added by using a normal random number generation with zero as the mean and the standard deviation similar to the intrinsic error in the localization ($rand_{x2,y2}$*=1.5 mm* and $rand_{x1,y1}$*=5 ms*). The interpolation methods created by modifying the parameters described by Eq. 3.3, were used to extract an approximation of the velocity from the set of equations proposed in Eq. 3.4.

$$x = R\cos\left(\omega t + randn_{x1}\right) + randn_{x2}$$
$$y = R\cos\left(\omega t + randn_{y1}\right) + randn_{y2} \qquad \text{Eq. 3.4}$$
$$R = 20mm; 0 < t < 1000ms$$

The equations were tested over 3, 5, and 7 consecutive location points with polynomials of the 1st, 2nd and 3rd order. The aim is to further investigate if a higher order polynomial best calculates the velocity for an artificial dataset with similar properties of the current *PEPT* experiment.

The first step is deciding the number of consecutive locations to interpolate, and this means choosing a large enough number of points to reduce the effect of the spatial uncertainty, described in Figure 3.7, source of over estimation of the velocity. This step implies considering a set of date not too large, in order to avoid smoothing out the final velocity. An optimum trade-off in deciding of the number of locations, must consider these two arguments.

The aim is to minimize the difference between the initial velocity (ω) masked by an error ($randn_{yx}$) given by Eq. 3.4, and the velocity obtained by applying Eq. 3.3 For no noise added to Eq. 3.4 all the method produce no error and mean value equal to ω; but because of the noise ($rand_{yx}$) and the introduced localization error, the accuracy of each method can be directly measured by its standard deviation. In Table 3.4 it is reported the standard deviation for each combination of polynomial versus number of locations.

		Order of the Polynomial		
		1st	2nd	3rd
Number of Locations	3	6.9006	6.9006	6.9009
	5	4.3579	4.3579	9.2485
	7	4.1794	4.1794	5.9721

Table 3.4: Standard deviations of the velocity computed for different number of locations with 3 polynomials.

Curiously there seems to be no difference between the 1st and 2nd order interpolating any number of locations. This is an interesting mathematical "loop", called the Cauchy's Mean-Value, possible only because the derivative is carried out for the middle point of the data set.

Because of the trivial difference in error between the 5 point and 7 point 1st order polynomial, and also considering the deteriorating quality of the data as reported in Table 3.3, it was chosen the 5 point-1st order interpolation, Figure 3.10.

The MATLAB® algorithm discussed and developed for this chapter (*Interp3PEPT.m*) is given in APPENDIX I. It allows for the calculation of the velocity over any length of data slice (*i.e.* 4,5,6) and using polynomials up to the 3rd order.

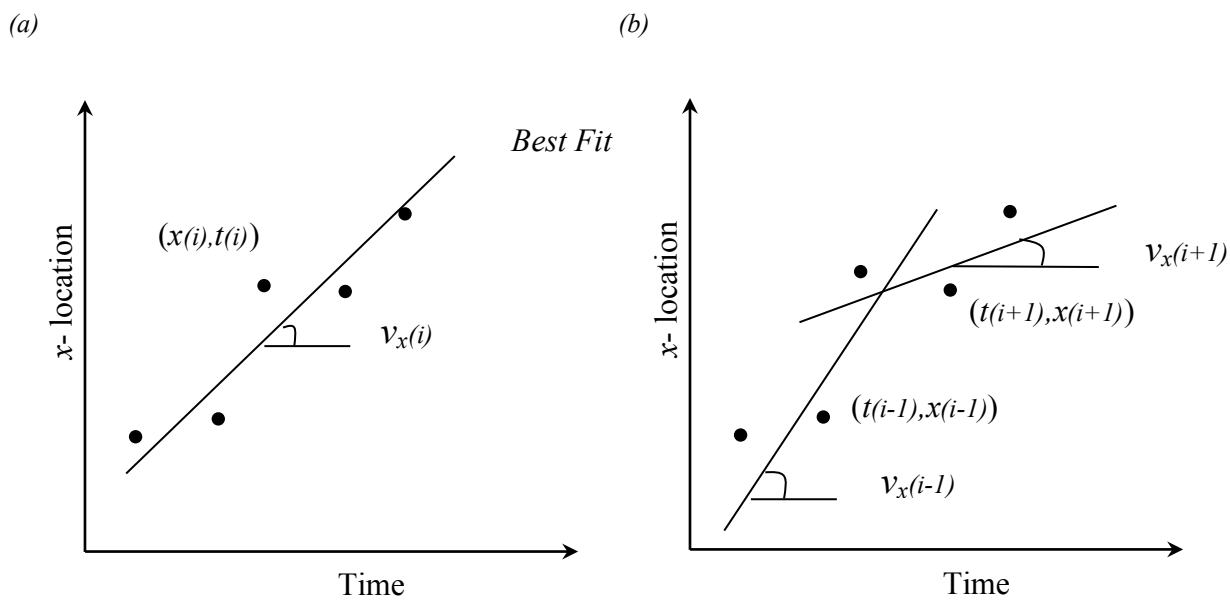

Figure 3.10: first order interpolation over 5 points in (a) for point t(i) and x(i) and 3 points in t(i-1), x(i-1) and t(i+1), x(i+1) in (b)

3.3.2.8.1. Azimuthally averaged velocity over cylindrical coordinates

The central rotating shaft of the pin stirrer produces as discussed, a predominantly rotational flow. The obvious choice of the reference system is cylindrical. From a theoretical point of view using cylindrical coordinates. Bases on the reference system used through out

this chapter, the Cartesian coordinates are converted to cylindrical following the equations given in Eq. 3.5, where the z coordinates remains unchanged.

$$\begin{aligned} z_{cyl} &= z_{cart} \\ \theta &= \arctan\left(\frac{y}{x}\right) \\ r &= \sqrt{\left(x^2 + y^2\right)} \end{aligned} \qquad \text{Eq. 3.5}$$

It is very interesting to note that by plotting θ function of time, for instance for the first run of glycerol as shown in Figure 3.11, an almost linearity. The slope of a best fit curve corresponds to the average tangential velocity, $\overline{v}_\theta$ equal to 5.61 RPS, approximately 0.3 times the shaft speed of 15 *RPS* (900 *RPM*).

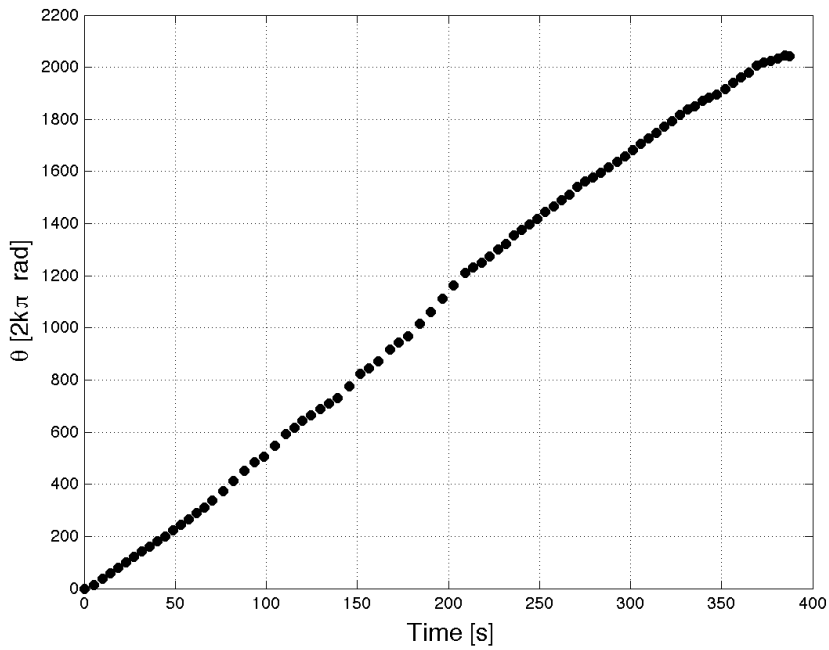

Figure 3.11: Cylindrical coordinate θ vs. time for the 1st run of glycerol. Only 1 every 500 location is shown.

All the runs described in Table 3.3, have been processed accordingly to what just described, and unified in a single file amounting to 0.5 million data points for glycerol and 0.9 for fluid gel. Once all the positions and the velocities are calculated in cylindrical coordinates, they are averaged on an imposed grid. Since the axial symmetric nature of the pin stirrer, azimuthal averages are used from this point on because they are clearly easier to read for analysis.

Azimuthal mean values are obtained by averaging the values of the locations falling within a toroidal volume and neglecting their angular coordinates as if they were on the same plane. Starting from cylindrical coordinates the script *eulo.m* developed in MATLAB® subdivides a cylinder of the same dimension of the dataset into iso-volumetric cells, in order to study the time concept of occupancy, time spent by the tracer in each portion of the system.

To each cell is assigned the value of the velocity of the passing tracer. Cells that represent areas of the pin stirrer characterized by low velocities; often present multiple consecutive locations. These are averaged to produce a single value of velocity.

A disadvantage of analysing *PEPT* data is that because the fairly constant data acquisition rate, of 100 *Hz* a tracer moving at $1 m\ s^{-1}$ will produce a location each 10 *mm*, where in slow moving areas the locations will be consistently closer. Thus in proximity of the pins there are less locations recorded by the *PEPT* cameras than in the rest of the column, where velocities are lower. To overcome this lack of information in some regions, a selective interpolation algorithm was adopted.

The use of the algorithm is only limited to a minor number of the cells, complying with a 3 cell distance separation criteria. Figure 3.12 shows the distribution of the distance between locations expressed in cells-units characteristic for the grid size chosen. This method

developed and proved extremely effective elsewhere (Chiti, 2007), was only limited to a few areas of the column.

The experiments done with glycerol and fluid gel show close to identical distributions in number of cell distance between to consecutive locations, Figure 3.12. The minor differences in the two, find a justification in the different time length of the experiments for the two fluids. The total time of the experiments done with the fluid gel lasted sensibly longer than those done with glycerol, Table 3.3. This means that even if the initial activity of the tracers was identical, the average activity through out the experiments results lower for the 2% agar fluid gel. This reflects on average, in less events being recorded by the cameras per unit of time for the fluid gel and thus its higher standard deviation in Figure 3.12.

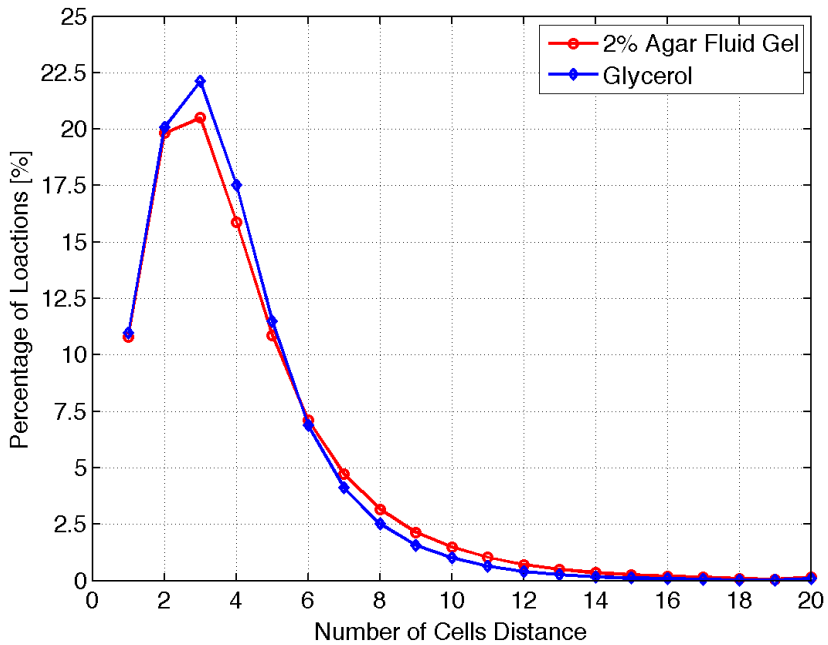

Figure 3.12: Distance expressed in cell number, between consecutive locations that fall in non consecutive cells.

The simple linear interpolation used for the cells constituting the gaps, is explained by Eq. 3.6. Where the missing velocity v_k relative to the cell with index k present between i and $i+1$ is calculated as proportional to the distance d_k between the cell i and k; with L being the distance between the two know locations of velocity v_i and v_{i+1}.

$$v_k = v_i + (v_{i+1} - v_i)\frac{d_k}{L} \qquad \text{Eq. 3.6}$$

The interpolation and, as already mentioned, the subdivision of the volume in iso-volumetric cells is done by the routine, *eulo.m* can be found in APPENDIX I.

3.3.2.9. Shear rates

In two-dimensional flows, shear rate is equal to the gradient of the velocity in a direction perpendicular to the velocity at that point. In three-dimensional flows, the situation is more complex and the shear rate is in general defined by a tensor with six independent components.

The classical rate of strain tensor A_{ij} derived in terms of displacement gradients as a point in a continuous medium relative to Cartesian axes the *i-th* component of the velocity in the *j-th* direction is given by Eq. 3.7 (Ilievski, Rudman *et al.*, 2001; Speetjens, Rudman *et al.*, 2006).

$$A_{ij} = \frac{\partial v_i}{\partial x_j}$$
$$\dot{\varepsilon}_{ij} = \left(A_{ji} + A_{ij}\right) \qquad \text{Eq. 3.7}$$

In cylindrical coordinates (Bird, Stewart *et al.*, 2002), the elements of the strain rate tensor ε_{ij}:

$$\dot{\varepsilon} = \begin{bmatrix} 2\frac{\partial v_r}{\partial r} & \left(\frac{\partial (v_\theta/r)}{\partial r} + \frac{1}{r}\frac{\partial v_r}{\partial \theta}\right) & \frac{\partial v_r}{\partial z} + \frac{\partial v_z}{\partial r} \\ \left(\frac{\partial (v_\theta/r)}{\partial r} + \frac{1}{r}\frac{\partial v_r}{\partial \theta}\right) & \frac{2}{r}\left(\frac{\partial v_\theta}{\partial \theta} + v_r\right) & \frac{\partial v_\theta}{\partial z} + \frac{1}{r}\frac{\partial v_z}{\partial \theta} \\ \frac{\partial v_r}{\partial z} + \frac{\partial v_z}{\partial r} & \frac{\partial v_\theta}{\partial z} + \frac{1}{r}\frac{\partial v_z}{\partial \theta} & 2\frac{\partial v_z}{\partial z} \end{bmatrix} \qquad \text{Eq. 3.8}$$

Each term of the strain rate tensor shown in Eq. 3.8, is calculated from the Eulerian transformation of the *PEPT* data, and consequently, it is time averaged for each coordinate.

Certain real combinations of the components of every symmetric second order tensor, are invariant to transformation of coordinates, and hence are scalar quantities. There are three

such combinations of components, and they are known as the scalar invariant of the tensor. The second invariant of the strain rate tensor Eq. 3.8 is also known as Frobenius norm (computed as described by *ShearCalc.m* in APPENDIX I), and is the shear rate, Eq. 3.9.

$$\dot{\gamma} = \sqrt{\sum_{i=1..3} \sum_{j=1..3} \left(\varepsilon_{ij}\right)^2} \qquad \text{Eq. 3.9}$$

The strain tensor is suitable to describe the rate of deformation in any purely viscous fluid in any state, since by definition; stresses in such materials are a function only of their instantaneous rate of strain.

3.3.3. Tribology of agarose fluid gels

The details of the fluid gels tested are summarized in Table 3.5. The methodology for their production is described in paragraph 3.3.2.2, relative to the set up of the pin stirrer during the *PEPT* experiment with agar.

Agarose Concentration [$\%_{w/w}$]	*T_{in} [°C]*	*T_{out} [°C]*	*Cooling Unit Temperature [°C]*	*Flow Rate [ml min^{-1}]*	*Shaft Speed [rpm]*
1%	*45*	*25*	*25*	*10*	*1450*
2%	*46*	*26*	*25*	*10*	*1450*
	45	*26.2*	*25*	*10*	*750*
	43	*26.1*	*25*	*10*	*350*
3%	*45.5*	*26.2*	*25*	*10*	*1450*
4%	*46*	*26.3*	*25*	*10*	*1450*

Table 3.5: Formulation parameters for the production of agarose fluid gels.

All fluid gel samples collected were allowed to "age" for at least three hours before carrying out the lubrication tests (Mohammed, Hember *et al.*, 1998). The overall set-up used in this study follows the work by Norton and Frith (2001), where the formation of fluid gels was also obtained in a pin-stirrer.

3.3.3.1. Rheometer configuration and set-up

This paragraph covers the rheological measurements relative to the tribology testing. All rheological measurements were carried out in a Gemini HR nano stress-controlled rheometer at 30 °*C* using a 20 *mm* vane geometry. This specific geometry was selected in order to minimise the possibility of slip for the very viscous samples tested. The flow curves were all obtained by allowing the system to reach a steady state under each of the applied shear rates within the range of 0.1 s^{-1} to 500 s^{-1}.

3.3.3.2. Texture analyser

Quiescently cooled agarose gels were left to rest for a period of 3 hours at room temperature, similarly to the fluid gels, thus ensuring that the kinetics of structuring have reached an equilibrium (Mohammed, Hember *et al.*, 1998). The TA.XT.plus, Texture Analyser (Stable Micro Systems Ltd., Godalming, Surrey, UK) was used to measure the stress-deformation relationship for each sample. The compression tests were performed on cylindrical geometries, all with standard dimensions of 10*mm* in height and base of 363.1 mm^2. The true stress σ and the true strain ε were calculated from the (recorded) normal force necessary to cause a certain level of deformation (also recorded) for each sample at a constant deformation rate of 1 $mm\ s^{-1}$ (Normand, Lootens *et al.*, 2000).

3.3.3.3. Particle size measurements

The particle sizes of the produced fluid gels were measured using a High Performance Particle Sizer (Mastersizer, Malvern Instruments, UK) with a refracting index for agarose of 1.42. Prior to particle size determination, fluid gel samples were diluted in distilled water and vigorously agitated, to give a homogeneous dispersion of particles, which could be then

detected in the Mastersizer. The effectiveness of the size measurements was validated by optical microscopy where a total of 50 particles were measured to determine an average diameter for each of the tested samples.

3.3.3.4. Tribometer configuration and set-up

The mini traction machine MTM (PCS Instruments, London, UK) was used to measure the friction coefficient (μ_F) and the traction forces (T_F) induced by the rotation of the disk on the ball (Figure 3.13(a)), while evaporation from the system was prevented by placing a lid at the top of the measuring cell. It is possible with the use of the MTM to map the μ_F over a range of entrained speeds (U) and obtain what is known as a Stribeck curve.

The set up of the apparatus is very similar to that used in previous studies (Guest and Spence, 2003; de Vicente, Stokes *et al.*, 2006). In the work by Guest and Spence (2003) a panel of candidates was interviewed regarding their perception of friction from pressing their stationary finger against a rotating disk. Similarly to this work and to "roughly" simulate the action of the (moving) tongue on the (stationary) palate, during in-mouth processing of food, the ball of the MTM apparatus was locked into a stationary position and only the disk was allowed to rotate (Guest and Spence, 2003).

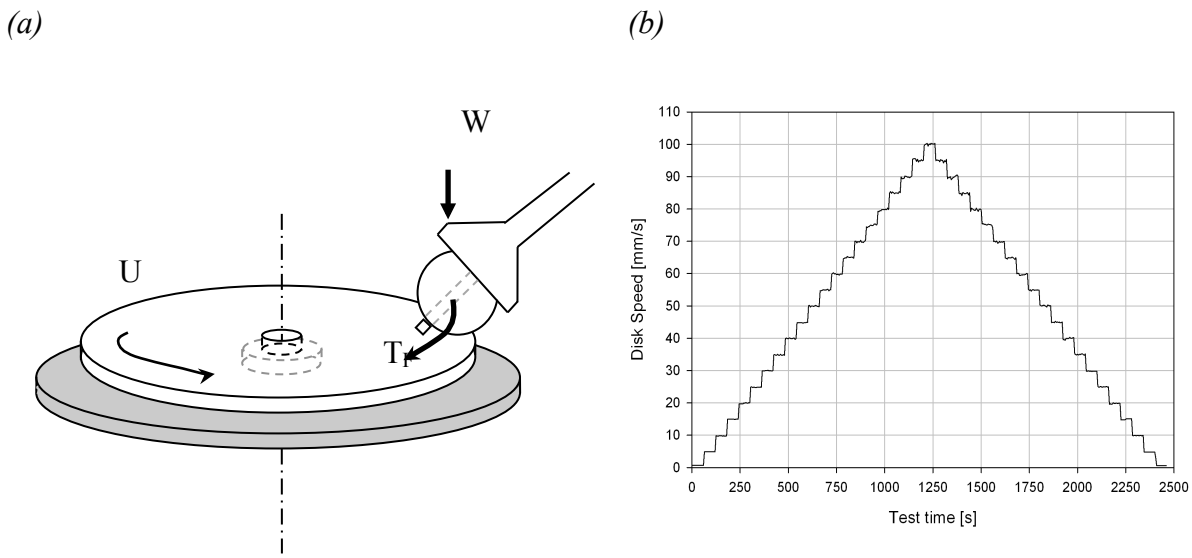

Figure 3.13: (a) Schematic representation of the Mini Traction Machine (MTM). W is the load on the disk, T_F is the traction force exerted by the disk on the ball. (b) Speed ramp profile used to obtain the Stribeck curve

The range of velocities investigated in this study, generally corresponds to what is known as the mixed regime of a Stribeck curve. The speed ramps were performed for disk speeds from 1 to 100 $mm\ s^{-1}$ (within this range speed was incremented in $5mm\ s^{-1}$ steps) followed by a symmetric decrease in disk speed, (Figure 3.13(b)). This range of velocities was chosen to represent the phenomena occurring during in-mouth processing (Malone, Appelqvist *et al.*, 2003). Each time step lasted 1 minute, during which an average statistical significant friction was measured, Figure 3.13(b).

The ball and the disk, after being used, were sonicated in distilled water for 20 minutes to ensure the same surface chemistry (degree of hydrophobicity) properties. (Bongaerts, Fourtouni *et al.*, 2007) During all the performed tests the forces applied on the fixed ball are measured at different velocities of rotation of the disk. The friction coefficient, μ_F, is then calculated as the ratio between the difference between loaded and unloaded traction force T_F and the normal load on the ball, W (Eq. 2.7)

The ball and the disk elements of the tribology apparatus were both purposely built in-house from silicon. The ball element of the tribometer (diameter, R, of 19 mm) was moulded

from a silicon elastomer (SYLGARD® 182) supplied by Dow Corning (elastic modulus of $E_{PDMS} = 2\ MPa$ and poison ratio of $\upsilon_{PDMS} = 0.5$). The tribometer disks used in the study were cut from a silicone foil (elastic modulus of $E_{Syl} = 5\ MPa$) supplied by SAMCO Silicone Products ltd, and had a diameter of 46 *mm*.

Chapter 4.

κ-CARRAGEENAN FLUID GELS

4.1. Introduction

In this chapter are reported the results of the microstructure investigations on κ–carrageenan fluid gels. After initial considerations on the effect of concentration on the gelation, the chapter develops around an exemplifying concentration. Focusing on parameters that control the mechanisms of formation. The competing mechanisms responsible for the formation of the particles are fully described, including the limiting shear rate for the formation of spinodally decomposed particles.

The rate of removal of heat is introduced are an engineering parameter to produce high yielding microstructures and discussed on the basis of kinetic arguments. The electrolytic nature of the monomers of κ–carrageenan persists in the fluid gel, with the cooling rate controlling the final kinetic of aggregation of the particles. The latter controls finally the reversibility upon cycles of stress ramps of structuring parameter *G'*.

4.2. Results and discussion

4.3. Effect of shear rate during fluid gel production

The effect of the applied shear on the production of κ-carrageenan fluid gels was initially investigated. This was assessed by measuring the viscosity of each of the fluid gel systems during their production process as a function of temperature and applied shear rate ($0.5 s^{-1}$ to $700 s^{-1}$); the data obtained are shown in Figure 2.1. All fluid gels were produced from the same "primary" solution containing 0.5% κ-carrageenan and 0.1% potassium chloride (KCl) concentrations, while the cooling rate during the production process was kept constant at 0.5 $^{o}C\ min^{-1}$.

The obtained data, across all shear rates, shows that as the temperature of the system is lowered, an increase in viscosity occurs at ~35°*C* (Figure 2.1). This viscosity increase has been ascribed (Norton, Jarvis *et al.*, 1999) to the formation of small gel nuclei (initiation of ordering), which begins close to the gelation temperature for the used hydrocolloid concentration (~32°*C*). As the temperature is lowered further the initially formed gel nuclei

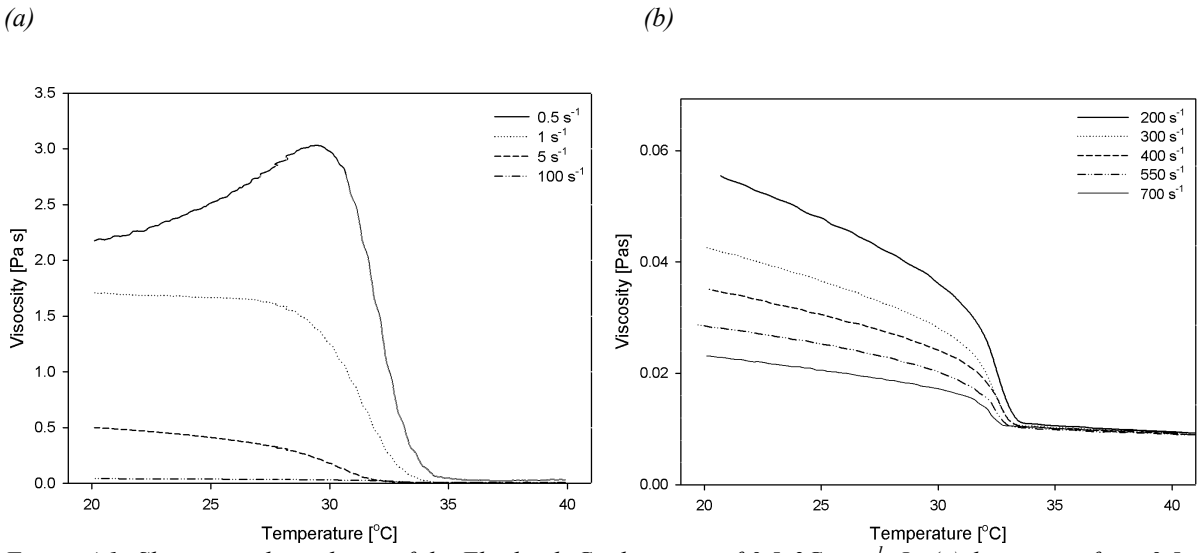

Figure 4.1: Shear rate dependence of the Fluid gel. Cooling rate of 0.5 °C min^{-1}. In (a)shear rates from 0.5 s^{-1} and 100 s^{-1} while in (b) shear rates from 200 s^{-1} and 700 s^{-1}.

continue to grow until an equilibrium particle size, as determined by the shear regime, is reached. The temperature range between ordering initiation and completion (or near completion) depends on the used hydrocolloid (about 5 °*C* in the case of κ-carrageenan) and it is within this range that the rapid viscosity increase takes place.

The initial formation of the small gel nuclei is believed to be the consequence of a demixing process that results in the formation of polymer-rich and polymer-poor regions in the system. The mechanism responsible for the initial stages of this demixing process is still not clear; there is plethora of arguments in the literature (*i.e.* Norton, Foster *et al.* (1998)) suggesting that demixing occurs either via spinodal decomposition or nucleation and growth.

Whichever mechanism is responsible for the initial stages of demixing, it appears that particles start to form in the early stages of the aggregation process, during which the nuclei are subjected to the applied shear forces and will appear to behave as water-in-water emulsion droplets; thus it is expected for both droplet coalescence and droplet break-up phenomena to take place within the system. What has not been fully determined either is the mechanism by which the growth of the (fluid gel) particles (once initially formed) occurs. However it has been suggested in the literature (Norton, Jarvis *et al.*, 1999) that this could be either via an "enrichment" process, of the initially small nuclei, from the surrounding non-gelled matrix or due to the coalescence/agglomeration of the particles being forced to come together under the applied shear flow. It therefore becomes clear that the observed rapid increase in viscosity is a direct result of the continual increase in both the number and volume fraction of the formed particles, which occurs within a temperature range near the hydrocolloid's gelation temperature (between ~35°*C* and ~30°*C* for the system in this study).

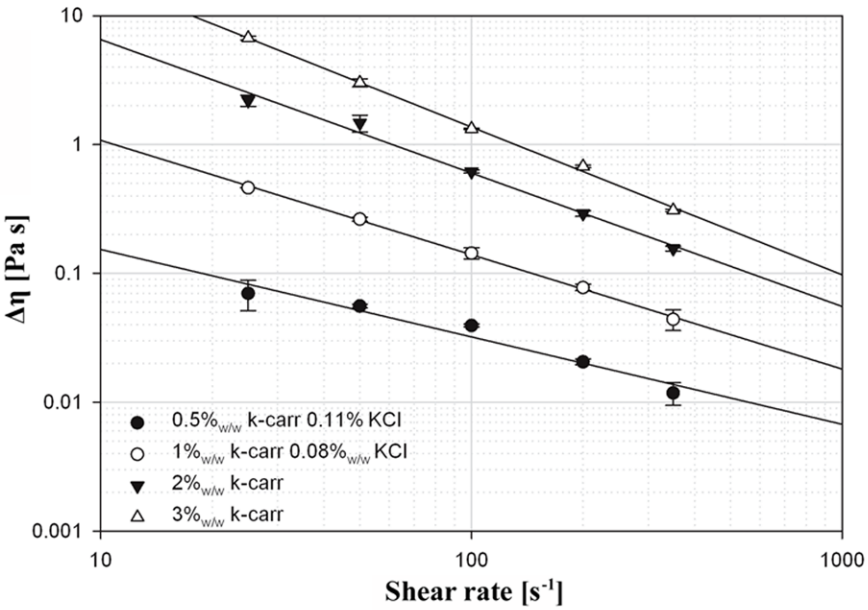

Figure 4.2:Double logarithmic plot of the increase in viscosity due to the formations of particles.

Emanuele and Palma-Vittorelli (1992) have reported that the viscosity increase ($\Delta\eta$), occurring within the temperature range between ordering initiation and completion, is inversely proportional to the shear rate ($\dot{\gamma}$) applied during the process. More specifically they report, for a 0.5%$_{w/w}$ agar solution, a power law relation between $\Delta\eta$ and $\dot{\gamma}$, the exponent of which is equal to -0.85. Data of viscosity change $\Delta\eta$ as a function of shear rate $\dot{\gamma}$ have been analysed for the fluid gel systems investigated in this study, Table 3.1. Figure 4.2 shows the relation between $\Delta\eta$ (calculated as described in the experimental section 3.3.1.4) and $\dot{\gamma}$ for fluid gels of different hydrocolloid concentrations produced at a cooling rate of 6 $°C\ min^{-1}$. The obtained straight lines on a double logarithmic plot confirm the power law dependency suggested by Emanuele and Palma-Vittorelli (1992). Table 4.1 contains the power law coefficients as calculated for the systems shown in Figure 4.2 using the following relation:

$$\Delta\eta = B(\dot{\gamma})^{c} \qquad \text{Eq. 4.1}$$

The power law exponent calculated for the systems investigated in this study is very close to that reported by Emanuele and Palma-Vittorelli (1992), however, it is also dependent, even though slightly, on the hydrocolloid concentration (see Table 4.1).

$\Delta\eta = B(\dot{\gamma})^{c}$	B	c	R^2
0.5% $_{w/w}$ κ-carrageenan and 0.1%$_{w/w}$ KCl	*0.73*	*-0.69*	*0.954*
1% $_{w/w}$ κ-carrageenan and 0.08%$_{w/w}$ KCl	*8.3*	*-0.89*	*0.998*
2% $_{w/w}$ κ-carrageenan	*71*	*-1.04*	*0.988*
3% $_{w/w}$ κ-carrageenan	*268*	*-1.15*	*0.995*

Table 4.1: Power law coefficients B and c calculated from the data shown in Figure 4.2.

Neglecting the influence of salt on the initial final value of the viscosity, the coefficient presented above can be expressed only function of the κ−carrageenan concentration, Eq. 4.2 and Eq. 4.3.

$$B = 7.5 C_P^{3.3} \quad \text{Eq. 4.2}$$

$$c = 0.85 C_P^{0.28} \quad \text{Eq. 4.3}$$

It is easily deduced by Eq. 4.2 that as the concentration of the polymer is increased the $\Delta\eta$ rise rapidly to higher values, whilst the slope of the curves in Figure 4.2, identifiable by *c*, does not vary significantly, but only to a power of 0.28 in the concentration, Eq. 4.3.

This phenomenon can be physically explained by considering that an increase in concentration of biopolymer produces particles with a higher rigidity *(B)*, resulting in lower propensity for the particles to squeeze past each other during the establishment of flow conditions, increasing as a consequence the bulk viscosity, but the particles interactions *(c)* and response to the shear is similar in the instances following the particle formation.

Coming back to the data presented in Figure 4.1, and as the temperature of the systems is further reduced (below ~30 °*C*), the initially observed "sudden" viscosity increase seems to become much more gradual for all applied shear rates except for values equal and lower than $0.5 s^{-1}$. In the case of the former (shear rates above 0.5 s^{-1} applied during the fluid gel production process), the observed change in viscosity could be a result of further ordering of a small number of remaining disordered polymer chains within the particles and/or at their surface; conformational ordering persists even at temperatures much lower than the gelling temperature. This would be expected to slightly increase the size of the particles and thus the viscosity measured during their production. Additionally the observed behaviour could be a consequence of the inter-particle interactions that take place as a result of the presence of disordered charged polymer chains at their surface (Norton, Foster *et al.*, 1998) which likely bind to free ions in the surrounding and form inter-particle bridges. As the applied shear rate is increased (for example from 1 s^{-1} to 5 s^{-1}) these chains tend to cyclise towards the particle forming a much smoother surface and thus limiting the likelihood of any inter-particle

interactions, which in turn results in the observed decrease in the "end" viscosity (the viscosity measured at the end of the fluid gel production process at ≈20 °*C*) as a function of applied shear. What should also be considered is the contribution to the increase in viscosity due to the decrease in temperature, generally known to obey an Arrhenius model.

On the contrary, the behaviour of a fluid gel subjected to very low shear rates (<0.5 s^{-1}) during its production process, and as the temperature of the system falls below ≈30 °*C*, is markedly different. What was observed, under this low shear rate environment, was that the viscosity of the system goes initially through a maximum and then gradually decreases (Figure 4.1). It appears that in this case, and due to the low shear involved, fluid gel particles are growing in size much faster and are much more "reactive" in terms of interacting with each other and creating aggregates. As a result their viscosity increases much more rapidly with decreasing temperature. In addition the formed fluid gel particles reach dimensions that are increasingly affected by the applied shear forces. Therefore, as the particles become very large (100's of micrometers), they are more likely to be broken up by the shear, resulting in the viscosity reduction that follows (Figure 4.1).

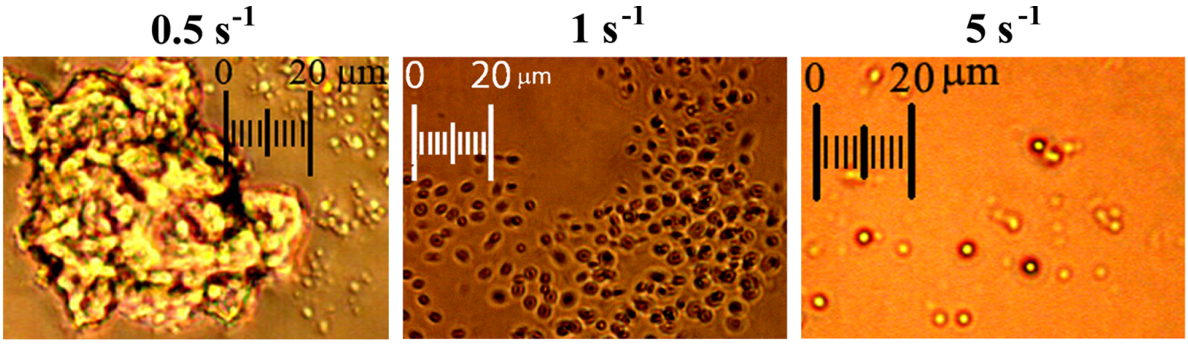

Figure 4.3: Micrographs of fluid gel particles as produced under different shear rates. Particles were diluted using 0.1% w/w KCl aqueous solution for the clearer observation of their structure

This hypothesis is supported by optical observation of the fluid gel structures produced at the end of each process as a function of the applied shear rate. Micrographs of the fluid gel system produced at the low applied shear rate (0.5 s^{-1}) revealed that irregular-shaped large

particles are formed, resembling fragments of a broken up larger gel structure (Figure 4.3). On the other hand, micrographs of fluid gels produced at higher applied shear rates (>0.5 s^{-1}) showed that the obtained particles are much smaller and of nearly spherical shape (Figure 4.3). This clearly supports the mechanism that was put forward earlier during the analysis of the rheological behaviour of fluid gels produced under these conditions of shear. The particles in this case are formed from the gelation of domain rich areas of the quenched solution, the size of which is determined by the shear environment.

The link between the size of the obtained fluid gel particles and the shear environment involved during their formation process is demonstrated in the obtained micrographs. More specifically the particle size of the produced fluid gels was found to decrease with increasing applied shear rates during the ordering process. An example can be seen in Figure 4.3 where the average size of particles produced for a shear rate of 1 s^{-1} is ~5 μm while that for a shear rate of 5 s^{-1} decreases to ~1 μm; note that a shear rate of 0.5 s^{-1} produces clusters/large aggregates of particles (rather than single/individual particles) of ~60 μm.

These experimental findings are in agreement with what is suggested in the literature; that is that the size of the fluid gel particles is dictated by the dynamic equilibrium between two competing processes (Carvalho and Djabourov, 1997). The break point between the nucleation and growth process and the spinodally decomposed particles appears from Figure 4.3 to lie some where between 0.5 s^{-1} and 1 s^{-1}. This critical shear rate ($\dot{\gamma}_c$) distinguishes between two processes. The first for $\dot{\gamma} < \dot{\gamma}_c$, in which the small gel nuclei grow, reaching large dimensions. This large gelled areas (~100μm) are affected by the constantly applied shear rate and are forced to break down into smaller particles until reaching equilibrium. The break down mechanism determines the large size and the irregular morphology. In the case of $\dot{\gamma} > \dot{\gamma}_c$, the mechanism of formation is diametrically opposite. During the cooling and shearing, the

domains of biopolymer rich areas form kept separated by the applied shear. First Onuki (1987) and later Chan, Perrot *et al*. (1988) suggested that it is only the applied shear that determines the equilibrium particle size. Therefore, and since at the early stages of the aggregation process the gel nuclei are expected to behave as water-in-water emulsion droplets, increasing the applied shear rate during the fluid gel production, should indeed result in a size reduction of the obtained particles; as demonstrated in this study. With mean particle diameter having a different function of the shear rate, depending on the mechanism of formation; determined by $\dot{\gamma}_c$.

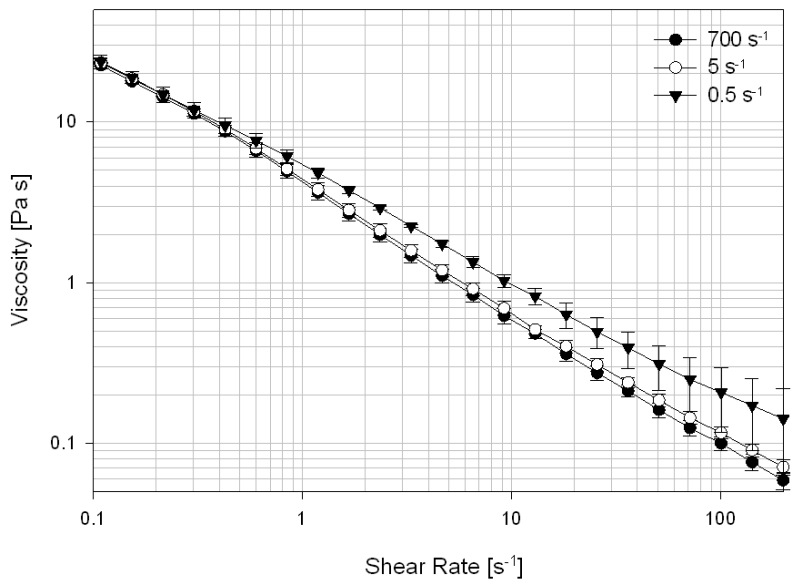

Figure 4.4 Shear thinning behaviour of 0.5% κ-carrageenan (0.1% KCl) fluid gels, produced under the different applied shear rates of 0.5 s^{-1}, 5 s^{-1} and 700 s^{-1}. The cooling rate during the formation process was 3 °C min^{-1}.

In order to investigate whether these differences in the particle size of the fluid gel, induced by varying the shear rate applied during their formation process, have an effect on the post-production flow behaviour of these systems the following analysis was performed. The viscosity of fluid gel samples (all 0.5% κ-carrageenan and 0.1% KCl), produced at 0.5 s^{-1}, 5 s^{-1} and 700 s^{-1} and at a constant cooling rate of 3 °$C\ min^{-1}$, was measured immediately after the end of their formation process and for a range of shear rates; data shown on a log-log scale in

Figure 4.4. It appears that, after production, the majority of samples (shear rates 5 s^{-1}-700 s^{-1}) exhibit a more or less identical shear thinning behaviour despite the difference in particle size between them. The reason for this is that in highly concentrated systems of (nearly spherical) particles, the flow is characterised on the micro scale by the relative flow of particles "squeezing" past each other. The bulk viscosity would thus be a direct function of the deformability (intrinsic elasticity) and packing of the particles, similarly to the behaviour of highly "packed" emulsions (Mason, Bibette *et al.*, 1996). The only exception to the flow behaviour post-production, as previously discussed, is for the particles produced at 0.5 s^{-1}. The reason for this is the different morphology of these particles (see Figure 4.3) and the non-uniform size distributions obtained which are also responsible for the higher variability of the viscosity data (standard deviation of the measurements in Figure 4.4).

4.3.1. Effect of cooling rate during fluid gel production

The effect of the applied cooling rate on the production of κ-carrageenan fluid gels was also investigated. This was assessed by measuring the viscosity of each of the investigated fluid gel systems throughout their production process as a function of temperature and for a wide range of applied cooling rates (0.5 – 6 $°C\ min^{-1}$). All fluid gels were produced from the same "primary" solution containing 0.5% κ-carrageenan and 0.1% KCl, while the applied shear rate during the production process was kept constant initially at 50 s^{-1}, 100 s^{-1} and finally at 300 s^{-1}.

The obtained data revealed that as the applied cooling rate is reduced, and for all applied shear rates, the viscosity of the systems slightly increases (Figure 4.5(a) to (c)). Even though the effect is small it is suggested to be a result of more interactions between particles occurring at lower cooling rates. It is worth considering the effect that changes in the applied cooling rate would have on the duration of the fluid gel formation process; as the cooling rate is reduced

processing time increases. As a consequence it is expected that the lower the cooling rate applied during fluid gel formation, and therefore the longer the fluid gel system is processed, the greater the likelihood of bridging between the formed particles. A higher degree of bridging for particles produced at low cooling rates would explain the observed viscosity increase shown in Figure 4.5 (a)-(c). However, what would also then be expected is that at the higher cooling rates greater bridging potential persists post-processing (this hypothesis is tested and discussed in detail in the later parts of this study).

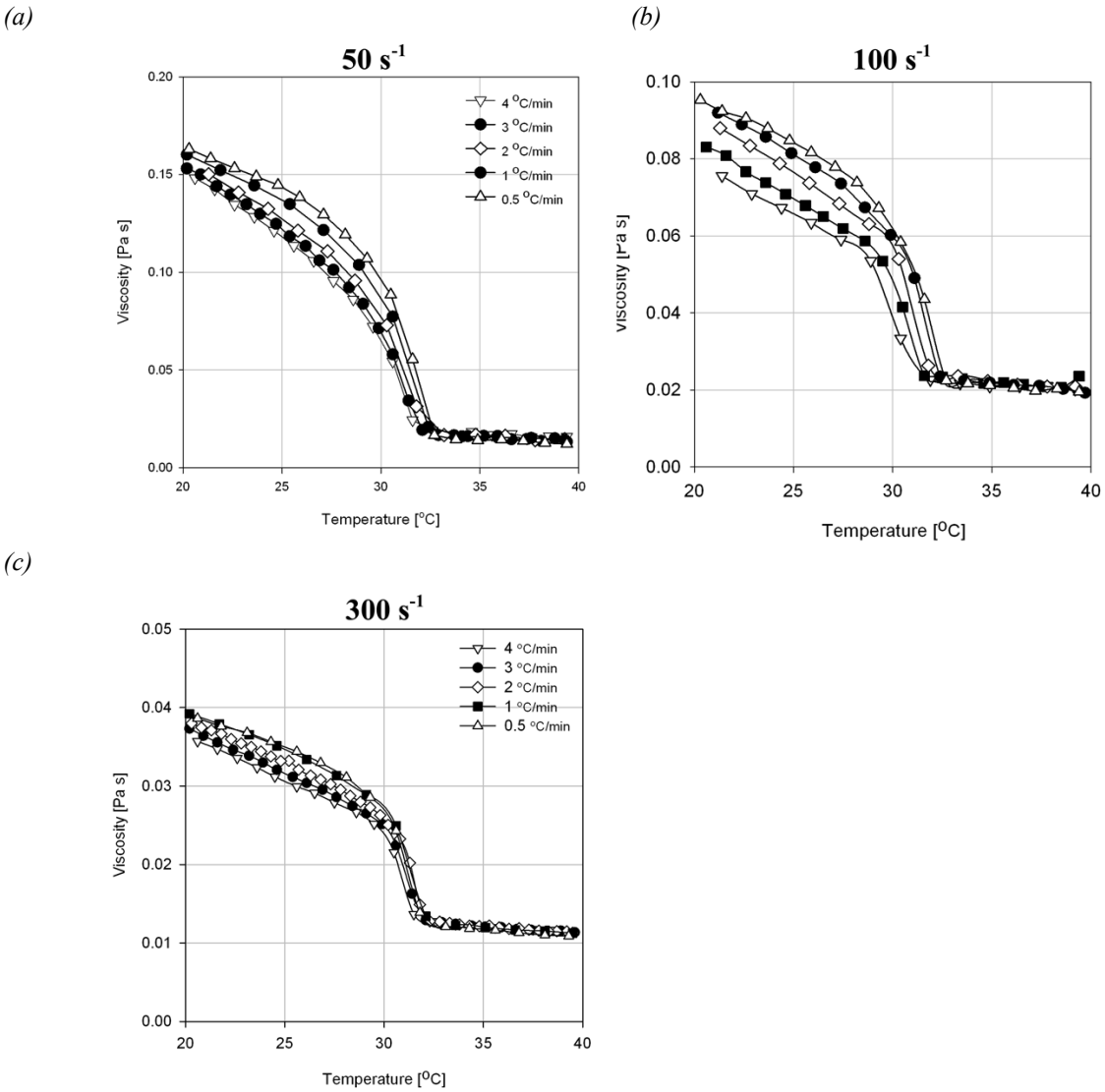

Figure 4.5: Viscosity of fluid gels, during their production process, as a function of the applied cooling rate. All systems are subjected to a constant shear rate of (a) 50 s^{-1}, (b) 100 s^{-1} and (c) 300 s^{-1}.

4.3.2. Particle interactions during and after production

In order to explore the nature of the interactions (bridging) between particles, occurring during fluid gel production, and to investigate whether these "persist" after sample production (and in the absence of applied shear), the following study was carried out. A range of fluid gels as in Figure 4.5(b) was produced but when the temperature of the process reached 20 °*C* shearing of the systems was stopped and samples were held at this temperature and under no applied shear for 30 minutes. Finally, and immediately after this relaxation stage, all systems were subjected to a shear stress ramp of 4 $Pa\ min^{-1}$. Shear stress data were recorded as a function of shear rate, for all the applied cooling rates, and these are shown in Figure 4.6.

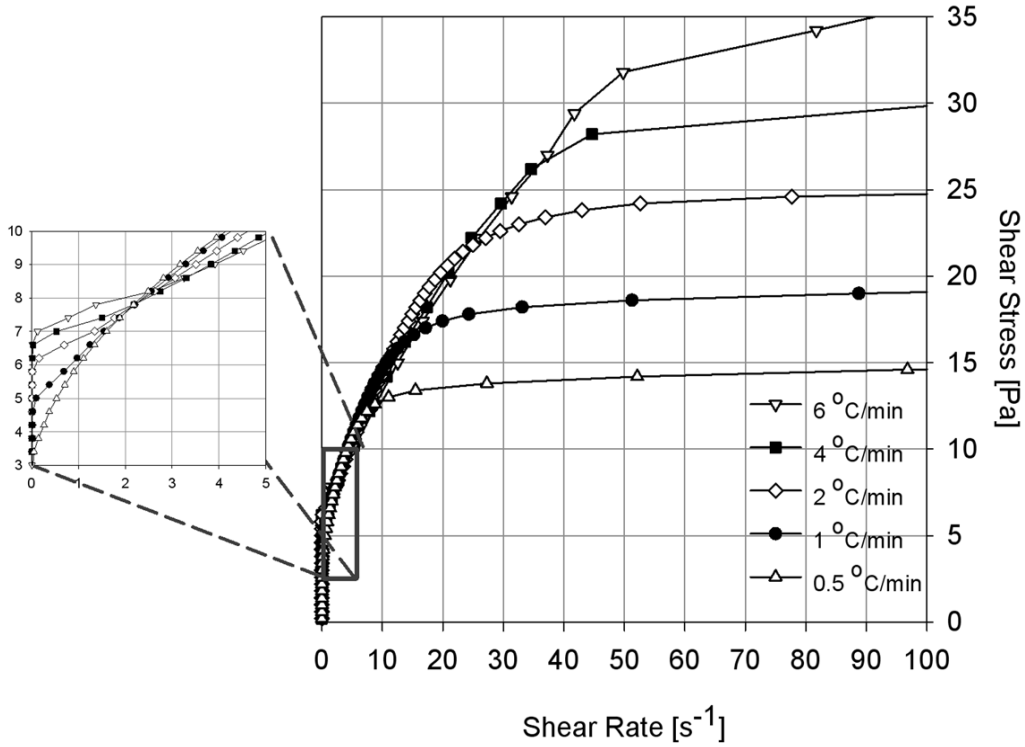

Figure 4.6: Response of fluid gels, produced at a constant shear rate of 100 s^{-1} and under different applied cooling rates, to a shear stress ramp of 4 Pa min^{-1}, measured as described in the text. Insert figure shows the observed yield stress dependence of the systems as a function of cooling rate.

The obtained results revealed the existence of a yield stress, extrapolated from the data in Figure 4.7 to zero shear rate, for all investigated fluid gel systems. The calculated yield stress, exhibited by the fluid gel systems after the 30 minutes relaxation interval, was found to depend on the cooling rate applied during their formation process. More specifically for an increase in the cooling rate from 0.5 $°C\ min^{-1}$ to 6 $°C\ min^{-1}$ the yield stress shows an increase from 2 *Pa* to 7 *Pa*. The bridging occurring between the particles is due to the cationic part of the salt; the yield stress is thus expected to increase for higher salt and biopolymer concentrations. What emerges then from this yield stress study is that the interactions (bridging) between the particles of the fluid gel structure not only exist post-processing but actually further develop (ripening of the structure) for a significant time after processing has finished. This continuous "strengthening" of the fluid gel structure, appears to be affected by the cooling rate applied during processing, with more extended interactions or bridging taking place for those structures produced at higher cooling rates.

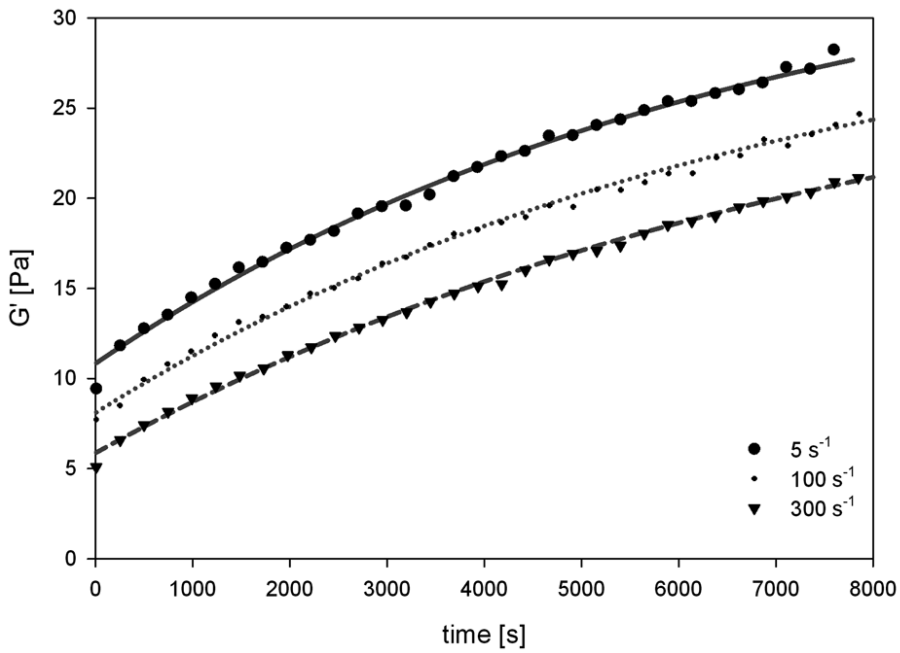

Figure 4.7 Storage modulus for 0.5% κ-carrageenan and 0.1% KCl fluid gels produced at different shear rates and cooling rate of 0.5 °C min^{-1} immediately after production.

In order to understand the time scale over which this "strengthening" process occurs the following kinetic study was carried out. Immediately after formation, a range of fluid gels was subjected to a "pseudo-resting" stage during which an oscillatory frequency of 1 *Hz* and a shear stress of 10 *mPa* were applied, and the elastic modulus response of the fluid gel samples was measured as a function of time. Figure 4.7 shows the data obtained for fluid gels (0.5% κ-carrageenan and 0.1% KCl) produced at different applied shear rates and a cooling rate of 0.5 $°C\ min^{-1}$. All three samples also show an increase in storage modulus with time and, as expected, fluid gels produced at the lowest shear rate have the highest storage modulus at the start of the kinetic experiment; since the low shear rate has allowed for more inter-particle interactions to occur during the fluid gel formation process. The observed behaviour can be modeled, supposing a first order kinetic of "interaction" between the fluid gel particles, by the following relation:

$$\frac{dG'}{dt} = K_e\left(G'_\infty - G'(t)\right) \qquad \text{Eq. 4.4}$$

$$\int_{G'_0}^{G'(t)} \frac{dG'(t)}{G'_\infty - G'(t)} = K_e \int_0^t dt \qquad \text{Eq. 4.5}$$

$$G'(t) = G'_\infty - \left(G'_\infty - G'_0\right)\exp\left(-K_e \cdot t\right) \qquad \text{Eq. 4.6}$$

	Shear rate, $\dot{\gamma}$ [s^{-1}]		
	5	**100**	**300**
G_0' [Pa]	10.30	7.74	5.47
G_∞' [Pa]	34.63	31.81	29.79
K_e [hr^{-1}]	0.54	0.51	0.45
R^2	0.99	0.99	0.99

Table 4.2: Model parameters from Eq. 4.2 calculated by fit to the data of Figure 4.7.

G_0' is the initial storage modulus after the shear has been stopped and G_∞' is the final storage modulus at a theoretically infinite time. The kinetic constant of the model (K_e) is strongly dependent on the likelihood of the particles to form an effective "bond" and thus it is suggested to describe the rate of "aging" of the fluid gel.

The data shown in Figure 4.7 were found to fit the proposed model (Eq. (2)) with a high correlation (shown as solid curves in Figure 4.7); calculated model parameters and coefficient of correlation R^2 are given in Table 4.2. As suggested from the data shown in Table 4.2 the applied shear rate during the production of the fluid gel has little effect on the relative rates of "aging"/ordering of the system; K_e changes only marginally with shear rate (Table 4.2). Therefore the extent of interactions between particles, taking place after the end of the fluid gel formation process and when shearing has stopped, are mainly controlled by the applied cooling rate during the process. On the contrary the interactions between the particles in the fluid gel systems, and thus the kinetic constant K_e, are expected to depend strongly on the polymer and salt concentrations.

By defining the as an aging rate (or ripening) of the gel, the first derivative in time of the storage modulus, it is possible to compare the data shown in Figure 4.7 against the ripening of a quiescently cooled gel. In order to successfully compare between samples, the cooling rate and the total experiment time has been kept identical also for the gel cooled under zero-shear. This allows plotting the result, shown in Figure 4.8, as a normalized ripening rate versus aging time. Figure 4.8, appears to be divided in two areas. At an initial stage, the aging rate of the fluid gel microstructure appears to be up to 3 times faster than for a quiescently cooled gel, diminishing to a value of ~0.5 after approximately 200*s*. As this appears puzzling with indications that could be a consequence of the mechanical energy, expressed in terms of shear rate, during cooling, is much clearer the relationship for the second stage of the aging. After the initial transitory, all the fluid gels reach an almost identical ripening rate, stabilizing with the exception of some noise of the measurement to a value of 0.5. This suggest, that the kinetic of gelation of the gel (Austen, Goodall *et al.*, 1988) and of the relative fluid gel follows the identical mechanism. The effect of salt and polymer concentrations on the rate of

"aging" of the particles (K_e), is thus expected to be similar to that reported for quiescently cooled gels.

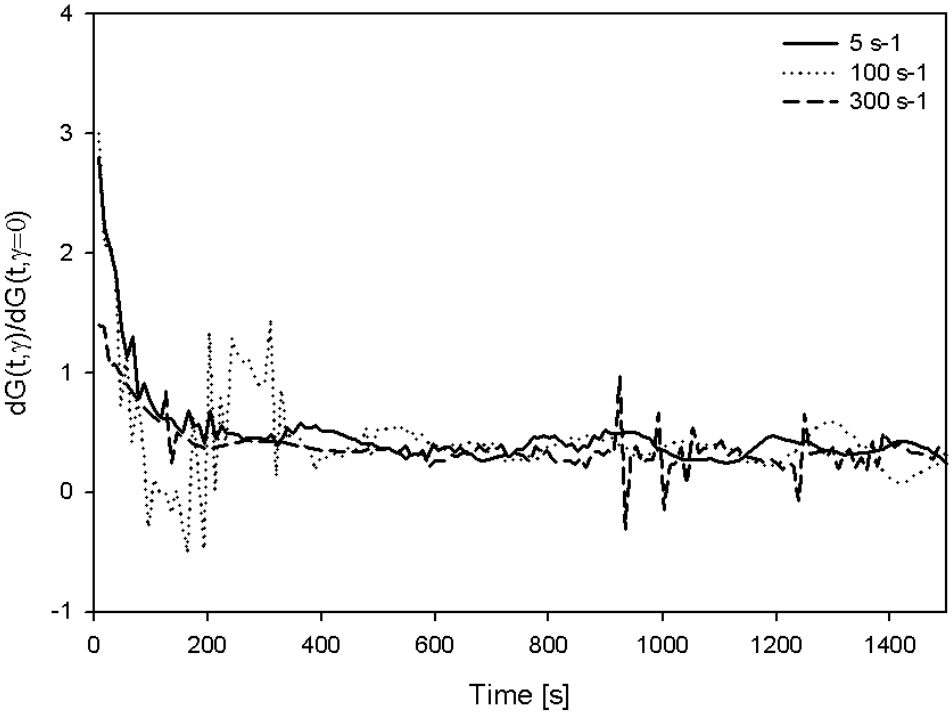

Figure 4.8: Kinetic growth rate ratio between fluid gel and quiescently cooled gel

The post-production extent of ordering was also monitored by performing stress sweep measurements within a stress range of 0.5 – 30 *Pa* and at a frequency of 1 *Hz* on a range of fluid gel systems produced at different shear and cooling rates; the chosen frequency is in the plateau region as measured by a frequency sweep. What was further investigated was whether the behaviour of the structure, observed during the first sweep, could be recovered by allowing the samples to "rest" for 15 minutes and immediately performing a second stress sweep (under the same experimental conditions as the first sweep).

Figure 4.9(a) shows the data obtained from performing the abovementioned test on a fluid gel sample produced at a cooling rate of 1 $°C\ min^{-1}$ and an applied shear rate of 5 s^{-1} (*system A*), while Figure 4.9(b) shows the data obtained for a fluid gel sample produced at a cooling rate of 6 $°C\ min^{-1}$ and an applied shear rate of 100 s^{-1} (*system B*).

(a) Stress Sweep Decay 5 s^{-1} and 1 °C min^{-1} *(b) Stress Sweep Decay 100 s^{-1} and 6 °C min^{-1}*

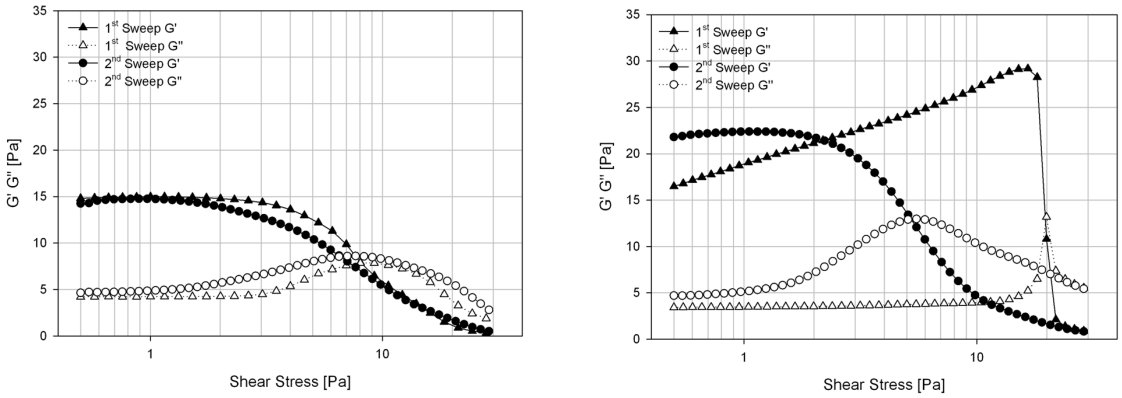

Figure 4.9: Storage (G') and loss (G") moduli from stress sweep measurements for Systems A (a) and B (b) performed at 1 Hz. The 1st Sweep was carried out immediately after the production of the fluid gels and, after a "resting" stage of 15 min, it was followed by a 2nd sweep. Both systems produced from a 0.5% κ-carrageenan and 0.1% KCl "primary" solution; information on the process parameters during the production of each system is given in the main text.

In the case of *system A* (Figure 4.9(a)) it was observed that the storage (G') and loss (G'') moduli remain constant until a shear stress of ≈2 *Pa* is applied. The fact that the structure of the fluid gel does not change within this shear stress range suggests that there are no interactions taking place between the particles in the system. If the applied shear stress is increased over ≈2 *Pa* the "original" fluid gel structure for *system A* starts to fail and finally "collapses". Furthermore it was identified that, for *system A*, there was little change in the G' and G'' values measured for the two performed stress sweeps (Figure 4.9(a)), which indicates that the structure of the system (as monitored during the 2nd sweep) fully recovered to its initial state (as monitored during the 1st sweep) during the allowed relaxation period.

The behaviour observed for *system B* is markedly different from that observed for *system A*. In the case of the former, and during the 1st stress sweep, what can be observed in Figure 4.9 (b) is a continuous increase in the storage modulus, which maintains till shear stresses of about 11 *Pa*. This is a clear indication that the structure of the fluid gel is changing due to interactions between the particles in the system that continue to take place (structure "build-up" or ripening) after its production and during the 1st stress sweep experiment itself.

The reason for this, as previously discussed (see discussion on the data for Figure 4.6), is the high cooling rate used for the production of *system B*; higher cooling rates result in faster fluid gel production processes. As processing time decreases the particles in the produced system have had less time to form and so there is greater reactivity remaining once the shear environment is removed, at the end of the production process, thus they interact with each other to a greater extend (more inter-particle bridging) than if produced more slowly at lower cooling rates.

Coming back to the data in Figure 4.9(b), what can be further seen is that the initial structure "build-up" for *system B* comes to a sudden end as shear stress increases over 11 *Pa* when the fluid gel structure finally collapses. Allowing *system B* to "rest" and then performing the 2nd stress sweep, revealed that there is a big difference in the G' and G'' values measured for the two performed stress sweeps (Figure 4.9(b)), which indicates that the structure of the system (as monitored during the 2nd sweep) changes completely from that measured during the 1st sweep. The behaviour for *system B* during this 2nd stress sweep now resembles (qualitatively) that measured for *system A*; G' and G'' remain constant at low shear stresses (fluid gel structure remains unchanged) and start to change at higher stresses as the structure begins to fail and finally "collapses".

4.4. Conclusions

A range of fluid gel structures has been produced from κ-carrageenan, a bio-polyelectrolyte obtained from red seaweed. It was shown that by controlling the material (κ-carrageenan and salt concentrations) and process (shear and cooling rates during fluid gel production) parameters it is possible to manipulate the properties and size of individual particles as well as the interactions/bridging between them.

More specifically it was demonstrated that particles of elliptical and spherical morphologies (smaller than 5μm) can be produced by controlling the rates of two conflicting processes taking place during fluid gel production; these are the rate of ordering of the helices in the flow, defined in our systems as the rate of cooling, and the rate of deformation, defined as the rate of applied shear.

What was also shown is that the interactions and bridging between fluid gel particles can be controlled by the process parameters during their production. It was therefore shown that, without changing the material properties of the system, it is possible to design fluid gel microstructures with desired viscoelastic characteristics that, over the time scale described in this work, can be fully reversible.

Chapter 5.

A FLUID DYNAMIC INVESTIGATION OF FLUID GEL PRODUCTION

5.1. Introduction

In order to produce fluid gels with predetermined rheological characteristics, it is important to adequately, understand and control fluid dynamic conditions during processing. The aim of this chapter is to obtain an understanding of the fluid flow conditions within a model pin stirrer heat exchanger; referred in this work as pin stirrer, using Positron Emitting Particle Tracking (*PEPT*).

This work considers, a Newtonian reference solution (99% in weight of glycerol) for comparison with the fluid gel (2% in weight of agar). This chapter discusses the similarities and the differences between the two fluids across every section. The intention is to provide the reader with added information, and clearer understanding of the phenomenology.

Using the velocity field it was possible to calculate the rate of shear, which used in conjunction with the particle paths lead to a description of the shear history experienced by a fluid element.

5.2. Rheology of PEPT fluids

Details of the experimental conditions and the description of the set up of the pin stirrer before starting the experiment are given in *Chapter 3: Material and Methods.*

From Figure 5.1(a), the resistance of a fluid gel to the flow (viscosity) is higher at low shear, decreases with increasing shear rate. Hence, the agar fluid gel is a shear thinning. Figure 5.1(b) reproduces, the profile of shear rate versus shear stress, showings the fluid gel to posses a Herschel-Bulkley like behaviour, with a yield stress of approximately of 20 *Pa*.

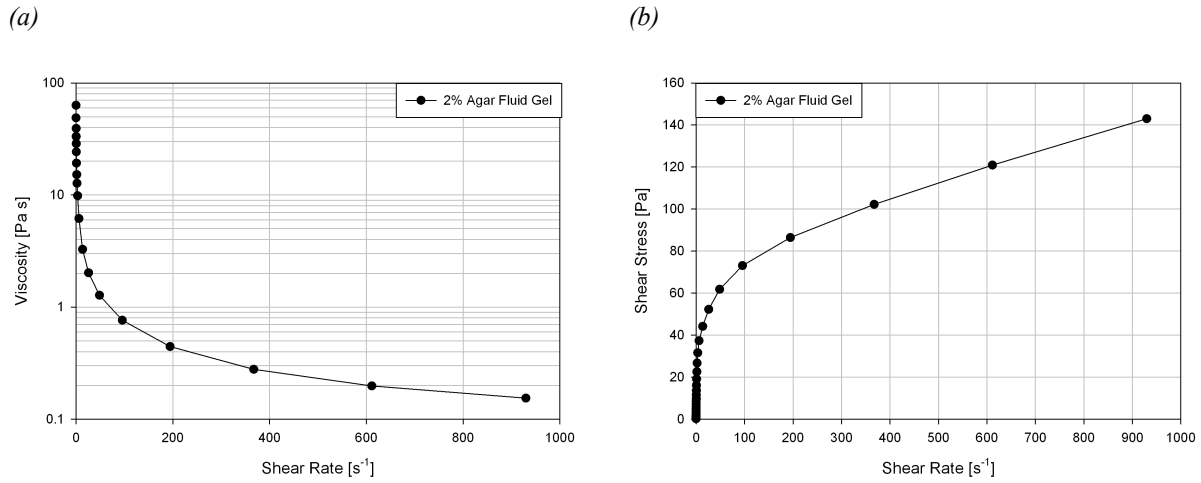

Figure 5.1: Rheology of the 2% agar fluid gel after the PEPT experiment. The sample was measured at 25 °C. In (a) the viscosity is plotted versus the rate of shear while (b) shows the relationship between the shear stress and shear rate.

Glycerol is a Newtonian fluid with viscosity well reported in literature (Dorsey, 1968). In this work a 99% glycerol in water solution was used, in order to obtain a fluid with a viscosity at 25°C of 1*Pa s*. This value of the viscosity obtained is in the same order of magnitude of the viscosity of the agar fluid gel.

Figure 5.1 shows the rheological properties of the fluids used in this work. In the experiment, agar at 65 *°C* was fed at the bottom of the pin stirrer. The fluid gel in the pin stirrer was formed by cooling down to 25 *°C* by circulating cooling water in the outside jacket. Agar was therefore led to gel within the shear field in the pin stirrer. The viscosity during this experiment varies with temperature, shear rate and the thermodynamic state of the biopolymer, *gelled / non-gelled.* These properties change locally within the pin stirrer making it challenging to predict the local rheological properties. It is therefore only possible to have a partial understanding of the rheological properties of the fluid gel within the column by observing the flow behaviour of the 2% agar fluid gel collected after the experiment.

5.3. Fluid dynamic investigations

5.3.1. Particle Paths

The raw data obtained from a *PEPT* experiment, has been pre processed as described in the relevant section of the Experimental Chapter. The refined data obtained is in essence the position of the tracer in time expressed in Cartesian coordinates. This preliminary knowledge of the motion paths within the pin stirrer contains considerable information. The results presented in this section are relative to glycerol (data set described in Table 3.3), however these observation are also common to the 2% agar fluid gel, showing at this stage an apparent similarity between the results obtained for the two fluid and across different runs.

The coordinate system used in this work is shown in Figure 2.9 and Figure 3.5

The labelling of the axes throughout this chapter has been kept consistent with what described by Figure 2.9 and Figure 3.5. A tracer rotating at a constant height, will result moving solely in the x and y coordinates while a change in z, will represents a movement along the height of the pin stirrer.

The typical particle motion along the x, y-axis in time is shown in Figure 5.2 (a) and (b). The tracer appears to move fluctuating periodically between -24*mm* and 24*mm*. These values correspond to the internal radius of the pin stirrer. The two figures therefore suggest the presence of a mainly rotational behaviour of the fluids within the pin stirrer. Figure 5.2(d) also supports this observation, where an extract of 2 seconds from the highlighted area of Figure 5.2(b) demonstrates that the particles mainly rotate around the central axis. This is expected as the stirrer rotates at 900*rpm*, resulting in a high rotational component. During these 2 seconds 226 locations were acquired, reflecting the overall temporal resolution of the run (113*Hz*) given in Table 3.3.

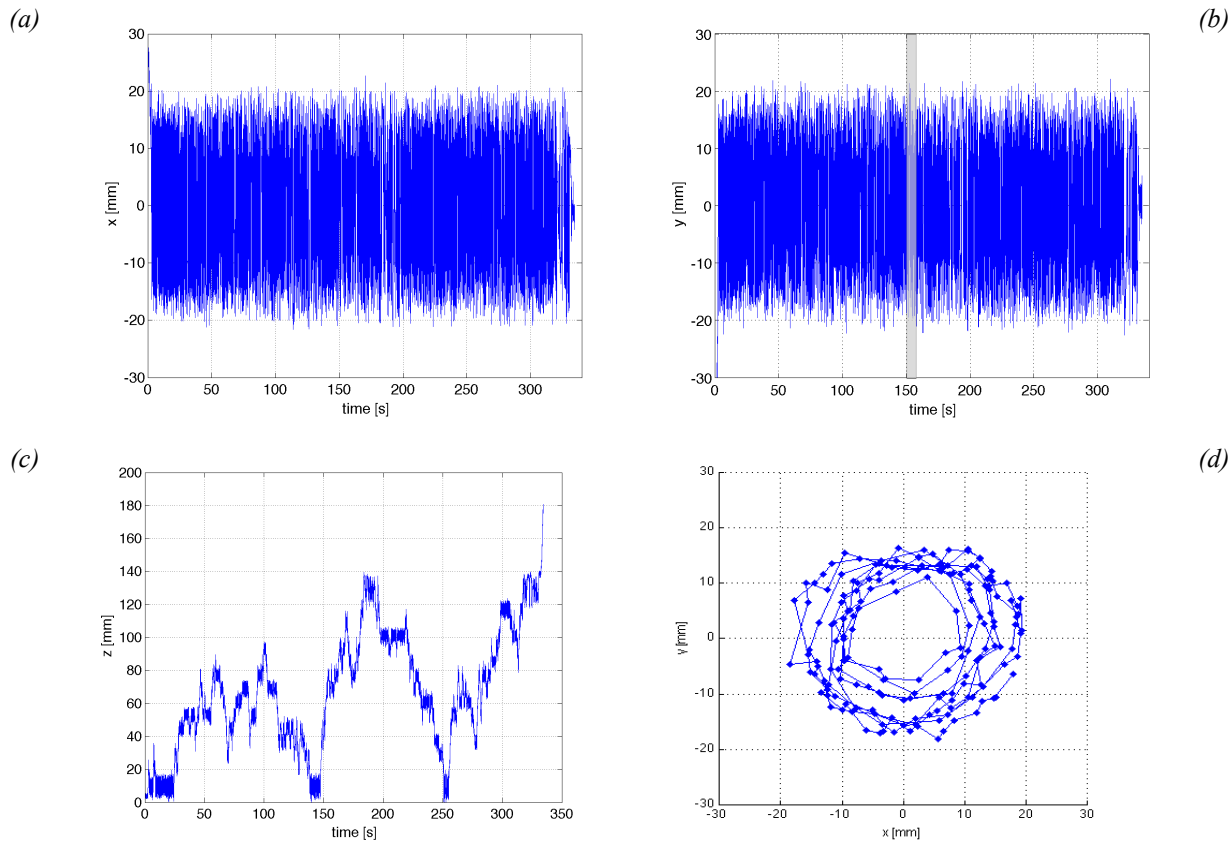

Figure 5.2: Tracer position in time for the glycerol during the experiment labeled "run 7". The figures in (a), (b) and (c) are respectively relative to the time progression of the Cartesian coordinates x,y and z. Meanwhile (d) is a 2 seconds extract from (a) (b), showing the rotational behavior of the tracer in the column and the number of acquired points per second.

The *z*-location of the tracer in time (Figure 5.2(c)) has a less intuitive behaviour compared to the motion along either *x* or *y*. The tracer is continuously subjected to leaps along the z-axis. These jumps suggest the presence of effective mixing inside the pin-stirrer. Interestingly the tracer seems to reside a considerable amount of time around fixed *z* before moving to a different height in the column, in Figure 5.2(c) between 200 and 220 seconds.

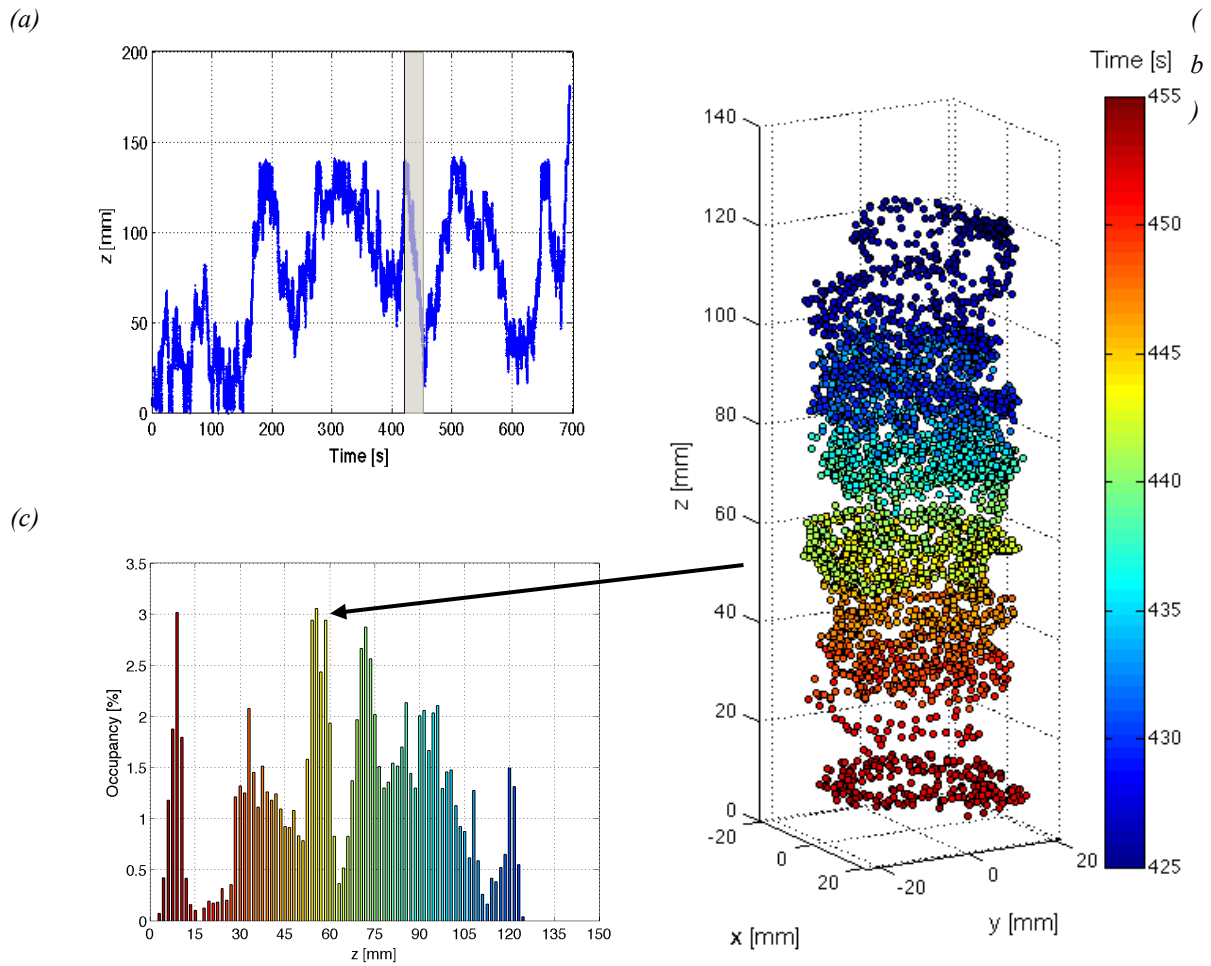

Figure 5.3: 3D particle paths for run 4 of glycerol. Clockwise from the top left: (a) shows the z locations in time with the highlighted portion expanded in (b) to show the 3D plot of the locations and in (c) for the relative z-occupancy

The movements of the tracer towards lower values of *z* describes a well mixed system, where a fluid element (described by the tracer) near the outlet at the top of the pin stirrer, is capable, given the right fluid dynamic conditions to proceed downwards towards the inlet, coming in contact with the incoming feed.

Figure 5.3 (a) to (c) clarifies the dynamics of these particular particle paths. The typical path of a particle demonstrating this 'random' behaviour is shown in the shaded area of Figure 5.3(a). Figure 5.3(b) shows the three-dimensional plot of these data with colour representing the time. From this figure one can see that particle follows a spiral flow.

Occupancy, defined as the percentage of time spent at a location, has been used in the past to characterise residence time in process equipment (Guida, Fan *et al.*, 2009). In Figure 5.3(c) a histogram of the flow residence time at different axial locations is shown. This graph is useful in describing the time spent by the tracer at each coordinate and can be used to further explain the backwards spiral motion obtain in Figure 5.3(b). The downward spiral, is a stage wise process were the tracer occupies preferably certain axial positions, and in some instances also rises, before continuing in the descent. Each time a tracer descends in a spiral, its movement can be represented by an occupancy histogram. All the histograms of the particle paths observed describe the descend as a stage wise movement, where the tracer resides at a preferred axial positions before proceeding either up wards or downwards, as shown in Figure 5.3(c). These axial positions or *z*-coordinates (equal to 8, 40, 56, 72, 88 and 120 *mm*) correspond with good accuracy to the axial location of six rotating pins.

The tendency of the tracer to reside longer in the proximity of these coordinates, may be explained either by an effect of a vortex created by the rotating pin resulting in a peculiar recirculation pattern or by the stationary pins that may hinder, a variation in *z*-direction. These conditions would actually allow the changes in *z*, only to those trajectories with an adequate momentum (velocity) and position within the pin stirrer.

The understanding of the mixing within the pin stirrer that emerges from these early observations of particle paths, describe a flow with predominant rotational movement. The inlet velocity of 0.0118 $m\ s^{-1}$ is not sufficient to quickly drive the fluid gel through the outlet present at the top of the pin-stirrer. The low inlet velocity has little or no effect on the internal flow patterns, characterized by frequent jumps of the tracer, just described. Higher inlet flow rates are expected to decrease the tendency of the tracer to randomly jump towards lower pins.

5.3.2. Return Time Distributions

The return time distribution (RTs) also known as circulation time distribution is a classical Lagrangian approach to the study of mixing, representing the number distribution of the time intervals between successive passages of a fluid element (represented by the tracer) through a fixed volume or surface. Return time distributions can be obtained using *PEPT* data. Return time distribution provide an understanding of mixing at a macroscopic scale (*macro-mixing*) within a process equipment (Larachi, Grandjean *et al.*, 2003; Chiti, 2007). In addition the RTs can be used to understand recirculation patterns, such as the ones observed within the pin stirrer, see Figure 5.3.

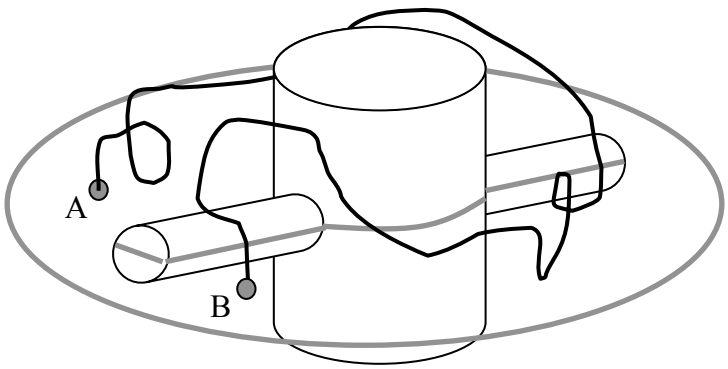

Figure 5.4: Schematic of the position of the reference plane in the Return Time calculations. The two points indicate the initial (A) and the first consecutive crossing from the tracer of the plane (B).

In this study 8 planes were used and will be referred to as reference planes. These planes were selected to be at the same axial locations as the rotating pins, Figure 5.4. It is hence possible to obtain 16 distributions, 8 relative to the glycerol and 8 for the fluid gel experiment as shown in Figure 5.5 (a) and (b).

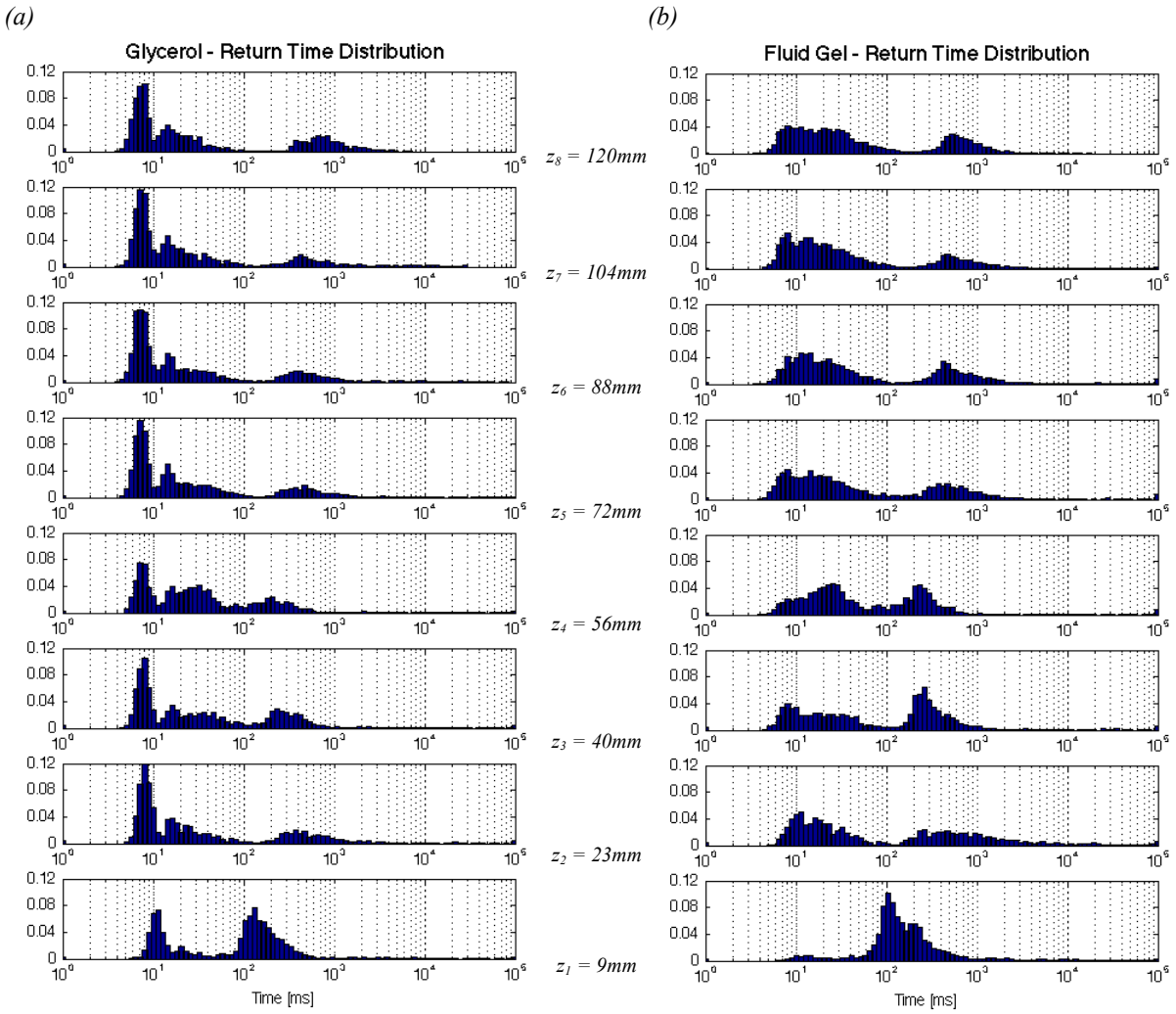

Figure 5.5: Return time distributions for glycerol (a) and fluid gel (b) for different axial positions.

Figure 5.5(a) shows that the return time distribution obtained for all reference planes are similar, with the exception of the first bottom pin ($z_1 = 9mm$).

The return time distributions for glycerol show a tri-modal characteristic Figure 5.5(a). A similar but less pronounced behaviour was observed for the Fluid gel, Figure 5.5(b), where the distinction between the two peaks at time scales of the order of 10 *ms* is less distinguishable.

Caution has to be taken when considering such short return times, and the error should be considered (see 3.3.2.6 discussing error minimization). The high velocity to the fluid and tracer near the pin, might mislead the reader in disregarding the localization error. However,

the motion is almost fully tangential and therefore two locations with coordinates (x_1,y_1,z_1) and (x_2,y_2,z_2), will have the planar components x and y least affected by the localization error, since Δx and Δy were sensibly larger than the error. The change in the axial component Δz of the position vector on the other hand, is of the same order of magnitude of the localization error. For this reason it is impossible to distinguish at this timescale, between a legitimate plane crossing due to oscillations behind the pin or wrongfully positioned locations. For rigour, the discussion, will not regard *RTs* at this length scale and only *RTs* shown in Figure 5.5(a) and (b) belonging to bins greater than ~10 *ms* are considered 'valid' particle paths.

The *RTs* for to the lowest reference plane are different from any other respective *RTs* for both fluids. This plane, which is at the same height of the first rotating pin ($z = 9\ mm$), is the closest to the inlet and to the bottom of the pin stirrer. The flow domain on this plane has a very different geometry when compared to the other planes. In fact, the bottom wall of the pin stirrer constrains the fluid movement, as shown in the schematic of Figure 5.6.

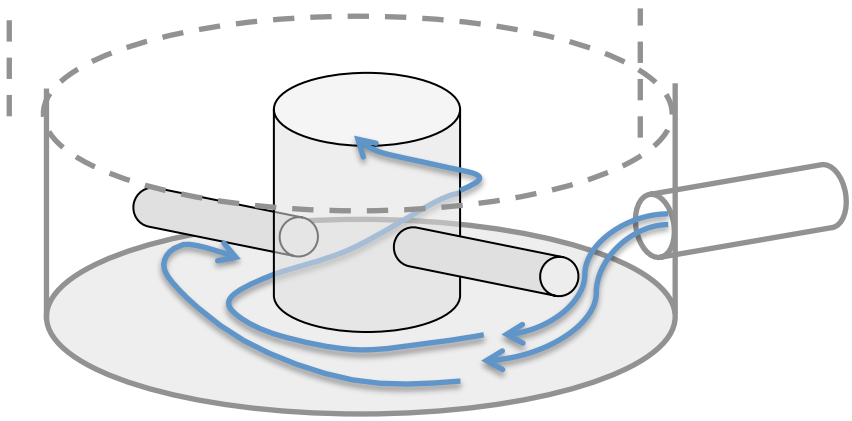

Figure 5.6: Schematic representation of the constrain imposed on the flow by the bottom wall of the pin stirrer. The arrows are inspired by the PEPT result. All the grey shaded areas are rotating, including the bottom wall.

As a consequence of its intended use in the food manufacturing industry, the pin stirrer was designed to minimise the probability of leakage and external contamination. For this reason the shaft, pins and the circular bottom wall are welded together into a singular rotating

element (Figure 3.3 and Figure 5.6). The clearance between the first pin (z = 9mm) and the bottom is of 5.2mm. The flow conditions, experienced by the tracers crossing the first reference plane (z_1) are therefore extremely different from any other plane. All these features, are valid for both fluids, and are responsible for the different flow near the inlet. Moreover for the specific case in which the fluid gel was circulating in the pin stirrer, the first reference plane was surrounded by low viscosity mixture of fluid gel and fresh biopolymer solution. Further reference planes, were gradually less exposed to the ungelled solution, and therefore higher viscosity.

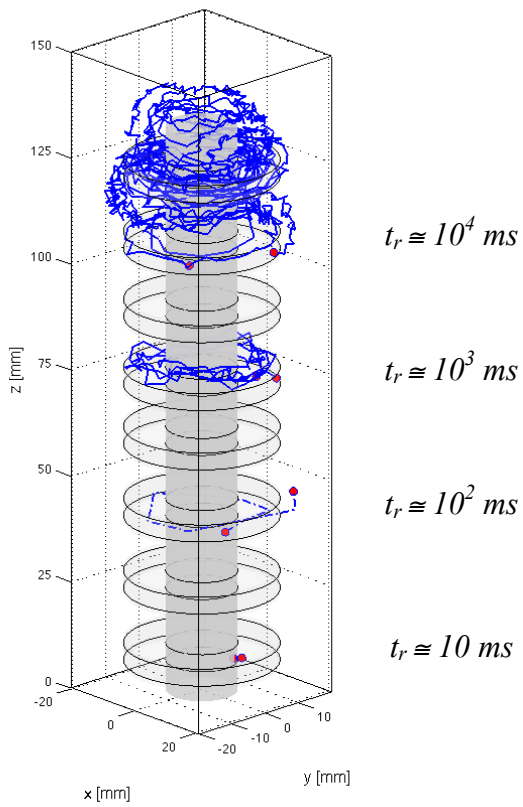

Figure 5.7: Four characteristic particle paths for different return times, as specified in the labels. The circular markers identify the two crossing points of the reference plane. The 8 disks describe the impeller swept volume.

Figure 5.7 is the key to clearly describe the *RT* distributions proposed in Figure 5.5 (a) and (b). The particle will travel different lengths depending on the return time. Figure 5.7

shows typical particle paths representing the different time scales *i.e.* 10 *ms*, 100 *ms*, 1*s* and 10 *s*.

In Figure 5.7 a return time of 10 *ms,* corresponds to random axial oscillation, with the tracer returning to the reference plane without completing a revolution. Particle paths with return time between 10^2 *ms* and 10^3 *ms*, are very likely to stay within the proximity of the rotating pin associated to the reference plane. In the rare instances where the right conditions are set for the particle to flow to the top or bottom level of the pin stirrer the return time increases significantly. From Figure 5.7 appears that particles returning to the reference plane after a RT of the order of ~10^4 *ms,* cross at least one other compartment and are extremely unlikely. In fact the tails of the RTs distributions in Figure 5.5 represent the frequency at which these jumps happen. No trend was observed in these jumps implying that the phenomenon is random, a statistical approach is followed in the next paragraph.

5.3.2.1. Statistical description of the tracers dispersion

Random events such as the movement of the tracer in the pin stirrer can be described statistically. As it was previously explained, three classes of particle paths can be distinguished based on the distance they travel before returning to the original plane. In this section, stationary reference planes were opportunely added to the pin-stirrer. These stationary planes, positioned at the same axial position of the stationary pins mounted on the external jacket (Figure 3.3), delimit compartments. Each section (or compartment) is positioned to contain a rotating pin, hence 8 compartments.

Two transfer probabilities were calculated in each compartment representing the dispersion of the tracers in the pin stirrer. The transfer probability was defined as the ratio between the tracers that cross the reference plane, and travel to the upper (or lower) compartment over the total number of tracers crossing the reference plane. This can be also

described as the ratio between the integral of the *RT* distribution of the particles that leave the reference plane over the integral of the total *RT* distribution (*RT* distributions shown in Figure 5.5). The transfer probability, defined as above, gives indication on the mass exchange rate between compartments within the column.

In Figure 5.8(a), the continuously stirred tanks connected in series, represent the compartments. In Figure 5.8(b) and (c) are shown respectively the transfer probabilities for glycerol and fluid gel.

An "upward shift" transfer probability of 0.4, means that 40% of the tracers, crossing the reference plane precede to the upper compartment. This probability (*Upward shift* in Figure 5.8(b) and (c)) is throughout the pin stirrer, always grater than the probability of moving to a lower compartment (*Downward shift* in Figure 5.8(b) and (c)). As there is a net flow of $0.33 ml\ s^{-1}$ (see 3.3.2.2) in the axial direction due to the inlet feed at the bottom of the pin stirrer, one would expect the probability of a particle to move towards the exit situated at the top of the pin stirrer, to be larger when compared to those at smaller z values, this is true only for the first 4 compartments. For values of z greater than $66mm$ the difference between the upward shift and downward shift transfer probability decreases to for compartments situated at axial locations higher than $66mm$. Further study is required to link the probability transfer to a mass flow rate.

The tracer travels to another compartment, only when dragged by a strong recirculation flow. The reference plane chosen lies on the same axis of the rotating pin. It is therefore reasonable to assume that a direct hit by the rotating pin causes the tracer to successfully travel to a following compartment.

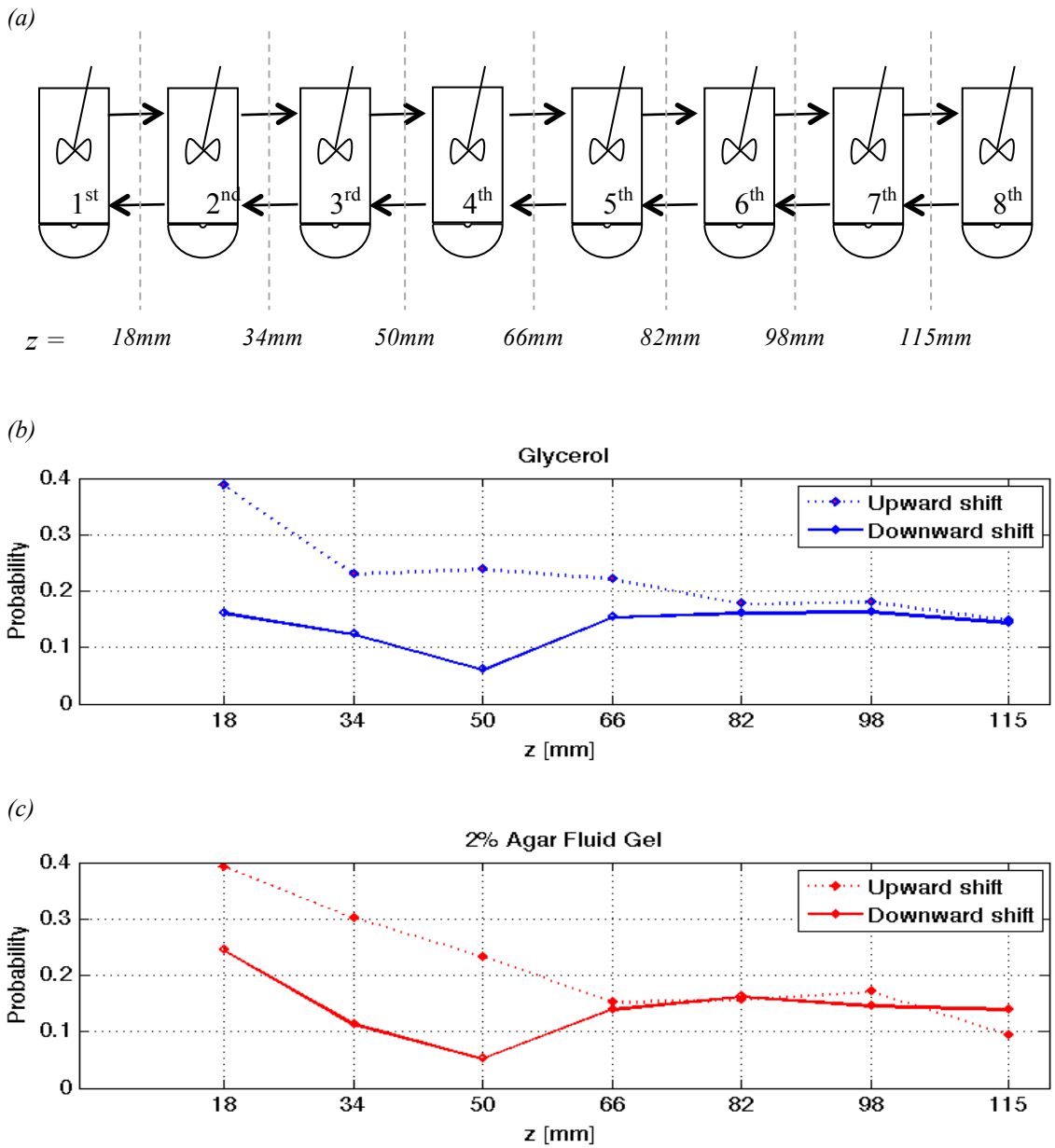

Figure 5.8: In (a), is proposed a schematic of the pin stirrer as a tank in series model. The following graphs show in (b) for glycerol and than for fluid gel in (c), the probability of a tracer leaving the surrounding of each pin to move either to an above compartment or below.

The probability, of a tracer to cross more than one compartment in a single jump should be equal to the product of the single probabilities of jumping each compartment.

The stationary reference planes were carefully positioned, with axial position adjusted to match the axial location of the stationary pins. The result however was found to changed minimally with the axial position of the stationary planes.

5.3.3. Azimuthally averaged velocity contour plots

The contour plots are helpful in visualizing the result of the velocity flow fields. In order to characterize and fully understand the fluid dynamics of the pin stirrer, in this section are presented the contour maps of the velocity for both the glycerol and the fluid gel. The velocity, v is calculated as $v = \sqrt{v_\theta + v_r + v_z}$, where the three components were obtained from the data analysis of the *PEPT* data (see 3.3.2.8). Figure 5.9(a) to (d) shows the velocity contour plots for the velocity magnitude, along side with the single components v_θ, v_z and v_r. Because of the symmetry along the θ-coordinate, the velocities are averaged over all θ-positions.

In Figure 5.9 one can seed that the tangential component of the velocity vector is one order of magnitude higher than the axial or the radial velocity. The tangential velocity is predominant. Similar results were found both glycerol and fluid gel.

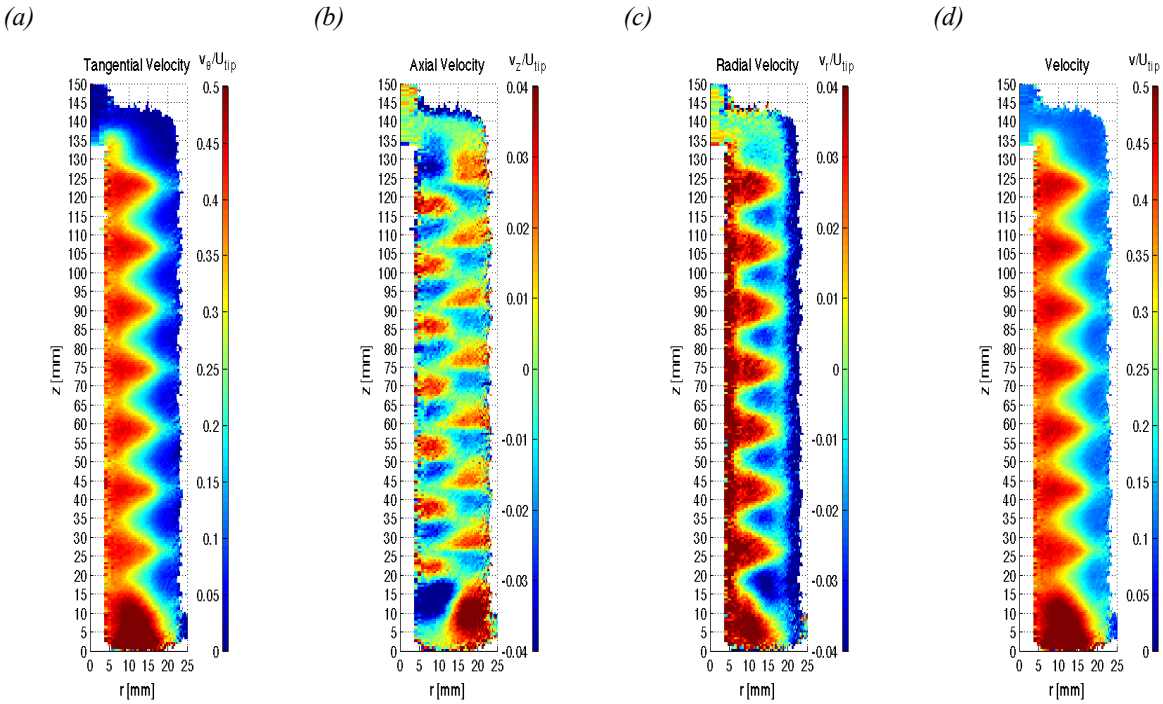

Figure 5.9: Eulerian azimuthally averaged contour plots for glycerol. On the left hand side the three components v_θ, v_z and v_r, while on the right hand side the modulus v.

The axial location of the top 7 rotating pins present on the shaft are clearly defined in the azimuthal projection, with exception of the first bottom pin, Figure 5.9 (a) - (d). The inlet pin found at a $z = 9mm$, appears to create in its surroundings an extended area of velocity above 0.55 times the U_{tip}. The other pins seem all to be inducing a similar velocity profile with intensity of the order of $0.4U_{tip}$. The higher velocity near the inlet could be explained by the geometrical disposition of the first pin along the shaft as described by Figure 3.3, and also by the drag force exerted by the bottom-rotating wall (shown in the sketch in Figure 5.6). This different flow profile is also hypothesised to be the cause of the irregular *RTs* in the first compartment shown in Figure 5.5.

Figure 5.10 shows the velocity contours for fluid gel. One can see that velocity plots are similar to those shown in Figure 5.9 for the experiment relative to glycerol. The fluid gel *PEPT* measurement differs from glycerol, for a lack of locations recorded in the top right corner corresponding to a toroidal volume. The glycerol contour plots indicate that in this region was recorded the lowest velocity throughout the column. The two top stationary pins, present at a z of 135 mm, Figure 3.3 might contribute in reducing drastically the velocity, by breaking the flow. The low velocity in this area, corresponds to a low shear, and consequently the biopolymer accumulates in the region, quiescently gelling and blocking the tracer from flowing in the corner.

Near the inlet, the bottom-rotating wall contributes to the momentum exchange with the flow, by exerting a drag force on the nearby fluid. The short distance between the pin and the bottom wall, favours in this area a high velocity, for both fluids. Velocity calculated for fluid gel was throughout the cross-section of the pin stirrer lower compared with glycerol with a maximum of $0.4U_{tip}$ compared to the $0.7U_{tip}$ glycerol.

The radial component of the velocity, v_r in the fluid gel experiment, in Figure 5.10(c) is approximately $0.06U_{tip}$ near the inlet (z=25*mm*) and decreases constantly for each consecutive pin along the stirrer, finally reaching a value of 0.04 times U_{tip} at z = 122 *mm*; on the other hand the tangential component of the velocity in Figure 5.10(a) follows an opposite trend. v_θ had a maximum of $0.25U_{tip}$ in proximity of the second pin at 25 *mm*, and was found to increase to $0.35U_{tip}$ near the last rotating pin at z = 122 *mm*. As the biopolymer rises in the pin stirrer, the difference between the tangential component of the velocity and the radial also increase. With the flow becoming more anisotropic and oriented towards the circumference. An isotropic flow on the contrary has no preferential orientation, and theoretically the ratios between all the velocity components are equal to 1. Isotropicity is an indication of good mixing performance (Paul, Atiemo-Obeng *et al.*, 2003). In Figure 5.10 the ratio between v_θ/v_r is the highest near the inlet and increases along the length of the pin stirrer. This trend is a clear indication of the increase in viscosity due to gelation of the biopolymer.

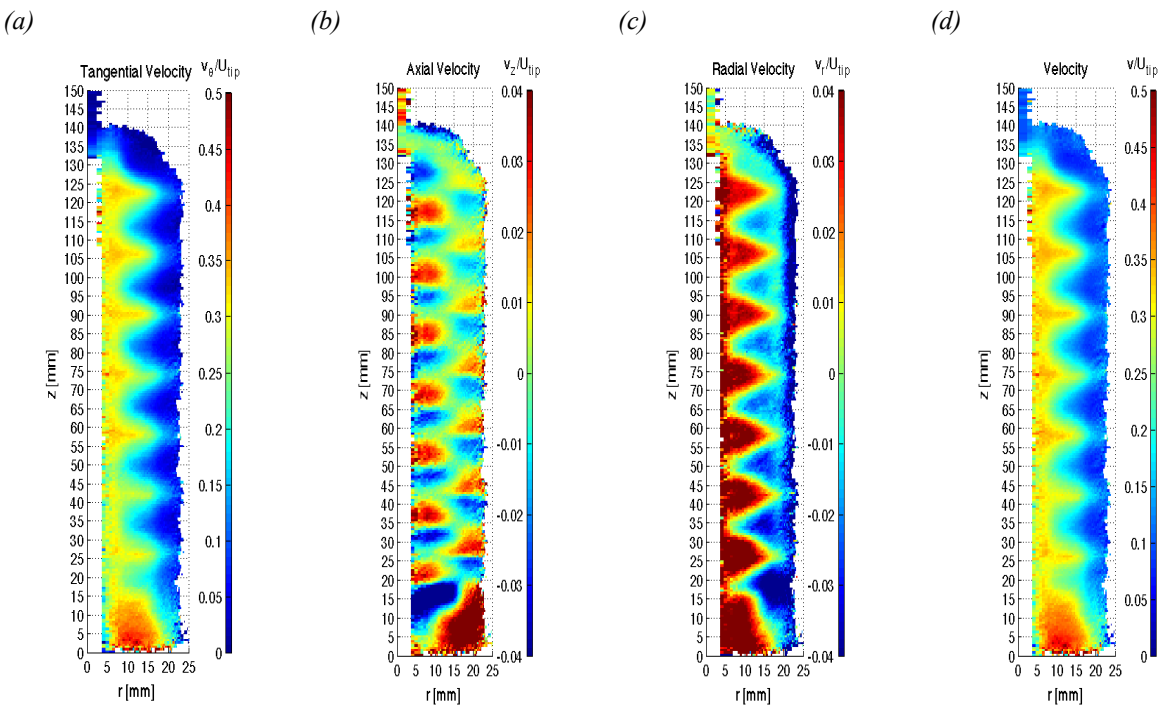

Figure 5.10: Eulerian azimuthally averaged contour plots for 2% agar fluid gel. Similarly to glycerol, on the left hand side the three components v_θ, v_z and v_r, while on the right hand side the modulus v.

Along the pin stirrer, the value of v_z was found to oscillate between -0.04U_{tip} and 0.04U_{tip}; the change in sign occurred exactly on the axial coordinate of the pin (Figure 5.9(b) and Figure 5.10(b)). The radial component of the velocity v_r near the pins was always positive, representing an outward moving tracer. These considerations about the axial and radial velocity component v_z, v_r; suggest the presence of recirculation vortexes created by pins in the confined space.

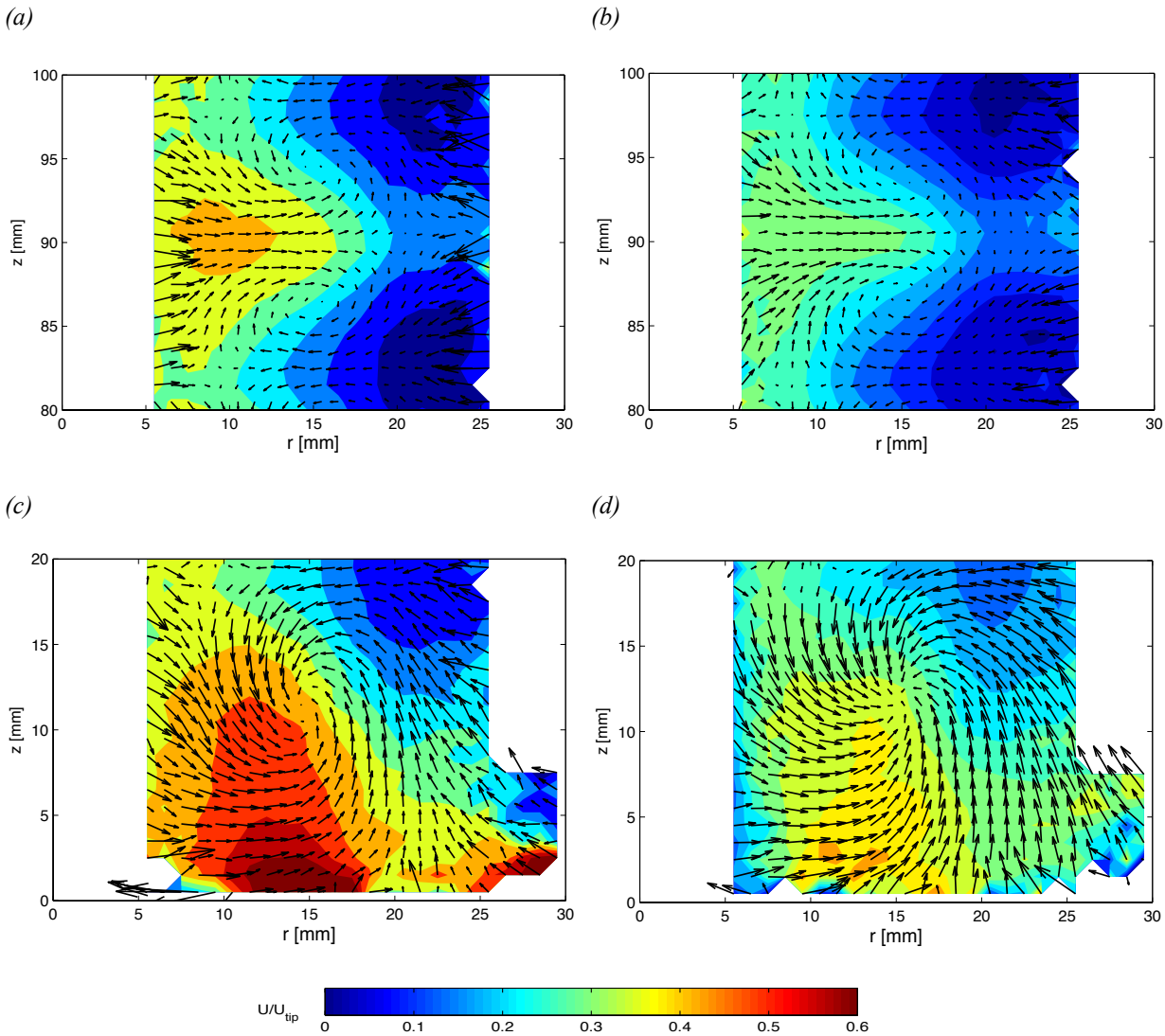

Figure 5.11: Velocity Vectors over imposed on contours of the magnitude of the velocity. (a) and (b) are the velocity vectors relative to the 6th pin of the stirrer meanwhile figures (c) and (d) show the vector plot near the inlet. Figure (a) and (c) are relative to glycerol and figure (b) and (d) to fluid gel.

Figure 5.11 shows vector plot of the velocity field created in the surrounding of the rotating pins. Figure 5.11(a)-(c) is relative to the glycerol, while Figure 5.11(b)-(d) are the vector plots obtained from fluid gel. The first pin, rotates closely to the bottom wall, creating a particular flow field, as shown in Figure 5.11(c)-(d). All the vector plots relative to the flow around the upper pins were similar and therefore in Figure 5.11(a)-(b) is shown only the velocity field around the 6th pin.

From Figure 5.11(a) and (b) one can see two vortexes been formed as the pin rotates in the compartment. The upped Vortex has an anti-clockwise motion meanwhile the bottom vortex rotates in a clockwise fashion. Each rotating pin always formed two counter rotating trailing vortexes. These trailing vortices are formed when the flow, pushed outwards by the pins breaks against the outer wall and changes direction. Half of the flow is directed upwards while the remaining in the opposite direction. This is shown in Figure 5.11(a) for glycerol and in Figure 5.11(b) for fluid gel.

The bottom pin on the other hand, was only recorded to form a single anti-clockwise vortex. Figure 5.11(c) and (d) show the vortex centre to be at approximately $z = 11$ *mm* and $r = 16$ *mm* during both experiments. It is remarkable how both fluids have identical flow structures with similar vortex intensities, rotation and position. This suggests a strong contribution of the pin stirrer geometry to the flow profile.

5.3.3.1. Velocity Profiles

Figure 5.12 shows the azimuthally averaged velocity profile across the height of the pin stirrer for a constant radius of 10 *mm*. Both fluids have the highest recorded velocity approximately for $r = 10$ *mm*.

For any values of the axial location z, the magnitude of the velocity calculated for the glycerol experiment was greater than the one obtained for the fluid gel experiment, Figure

5.12(d). The same can be said for the tangential component Figure 5.12(a). Although the impeller rotational velocity of 900 *rpm* was identical for both experiments, the difference in velocity can therefore be attributed to a difference in viscosity between fluid gel and glycerol.

The remaining two component of the velocity, the axial v_z and radial v_r, respectively shown in Figure 5.12(b) and Figure 5.12(c) were similar, with exception of the area near the first pin for $z < 20$ *mm*. Below this coordinate both v_z and v_r were higher for the fluid gel.

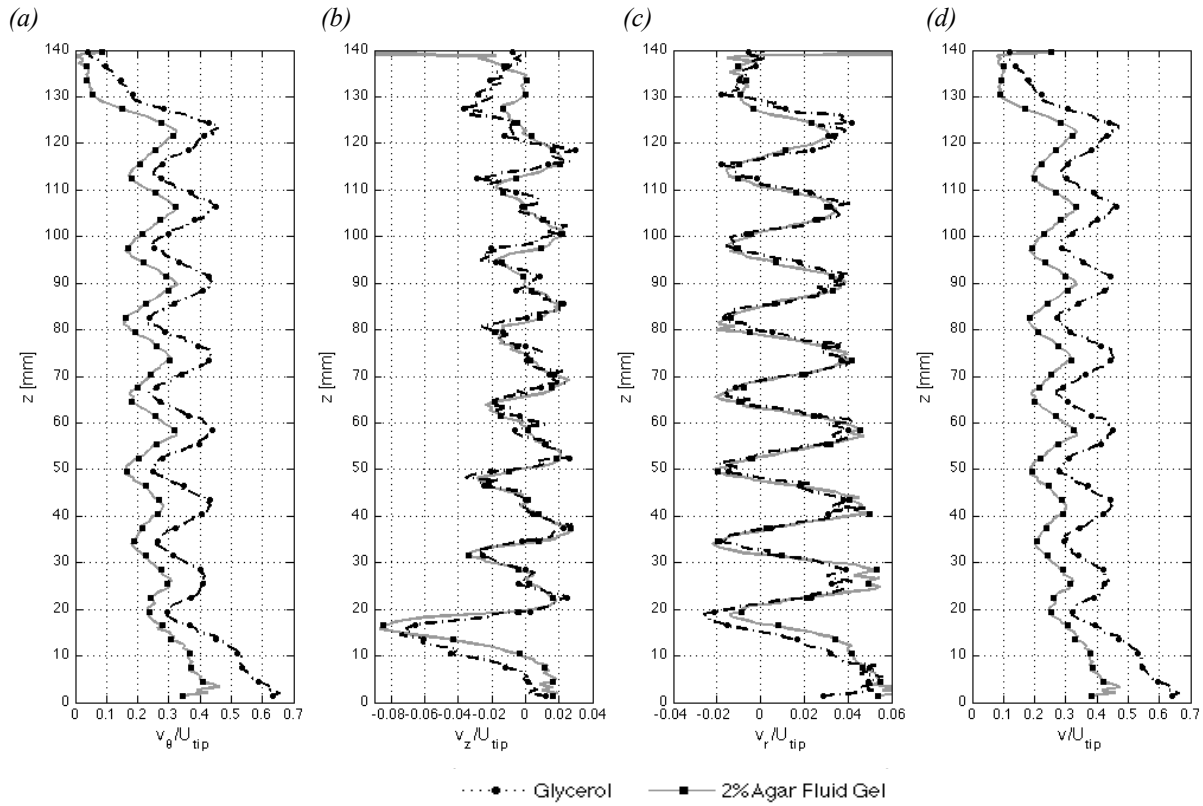

Figure 5.12: Velocity Profile along z, for r = 10 mm. From left to right are illustrated the comparison between tangential, axial and radial component of the velocity. The last graph shows the modulus of the velocity.

Similarly to what discussed in *Section 5.3.3,* the area of the pin stirrer near the inlet ($z <$ 20 *mm*) is during the fluid gel experiment, filled low viscosity non-gelled biopolymer. For this reason, in Figure 5.12 the difference between the two fluids are greater near the inlet. The Newtonian glycerol maintains a constant maximum radial velocity profile for all the pins. On the contrary the fluid gel has a lower maximum of v_r after each stage with increasing z.

Two fluids in fully turbulent conditions express the same velocity field for the same given applied stress. The difference in velocity between the two fluids proves two fundamental factors. Firstly that the difference in velocity field can be conjectured to be due to a difference in viscosity, and consequently that the flow regime is either laminar or transitional.

Although the calculation of the Reynolds number is complex due to the difficulty in quantifying the local properties of the flow, it is common practice for mixing vessels fitted with an agitator, to estimate the Reynolds number (N_{Re}) according to Eq. 5.1.

$$N_{Re} = \frac{\rho N D^2}{\eta} \qquad \text{Eq. 5.1}$$

Where N is the rotational velocity, D is the impeller diameter while, ρ and η are respectively the density and the viscosity of the fluid (Sinnott, 2005). Based on Eq. 5.1, the Reynolds number for the glycerol solution with a viscosity, η of $1 Pa\ s$ is N_{Re} = 2109. In stirred tanks, it is often regarded the flow as fully turbulent for value of $N_{Re} > 10^4$.

The following paragraph describes the velocity fields within the pin stirrer at predetermined axial coordinates, versus the fixed radial coordinate shown in Figure 5.12. The use of the two approaches to describe the flow field, adds important details to the description of the three dimensional movement of the flow.

(a) *(b)*

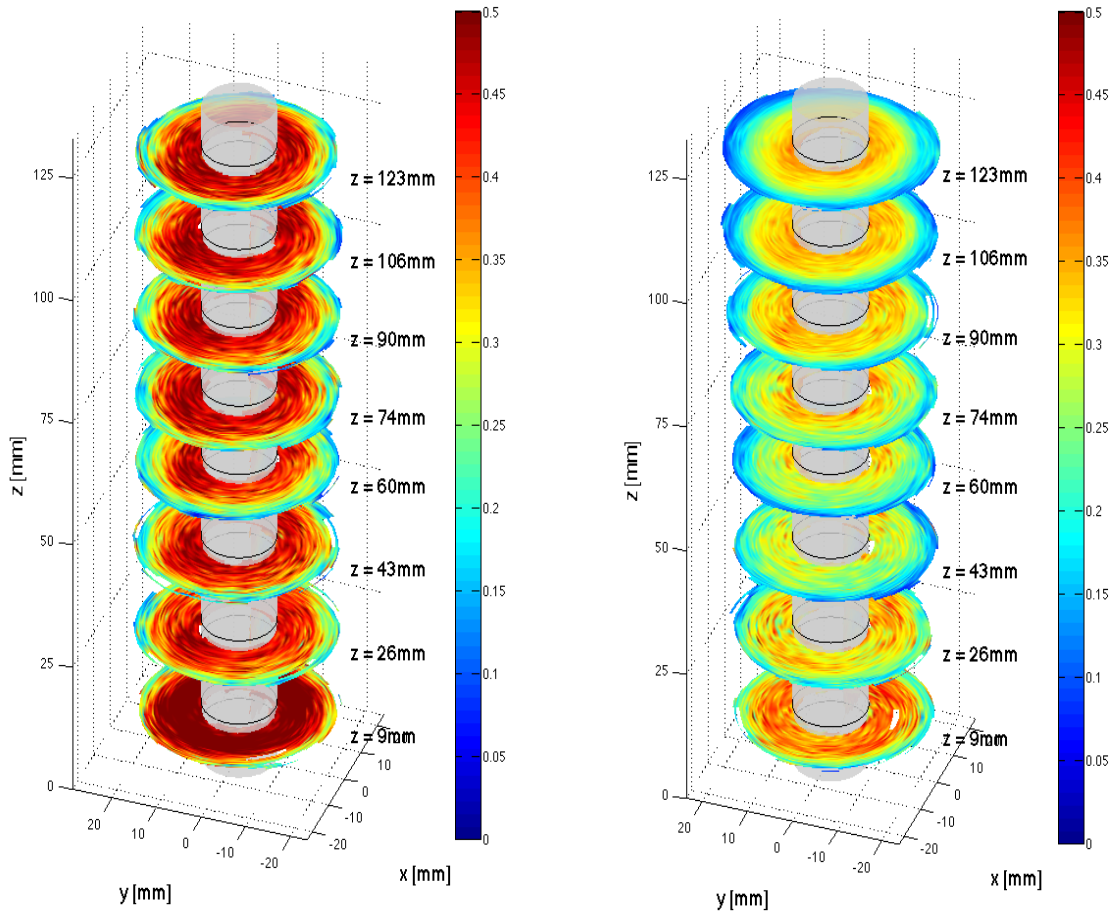

Figure 5.13: Glycerol azimuthally radial velocity plot. In (a) is shown the contour plots for each rotating pin with the velocity expressed as normalized by U_{tip}. The remaining figures are the velocity profiles at for the given coordinates.

Figure 5.13(a) shows the radial velocity contour plot and the velocity profiles for glycerol while Figure 5.13(b) shows, in a similar manner, the velocity contour plot for fluid gel. The axial coordinated of the planes were chosen to correspond to the locations of the rotational pins, and therefore the maximum velocity measured in each compartment. The colour scales were chosen to be identical to compare velocities between the two different fluids, the reader is therefore pointed to Figure 5.14 and the relative discussion for a more quantitative description of the fluid gel radial distribution of the velocity.

The contour plot of the velocity magnitude for glycerol Figure 5.13(a), shows similar velocity fields across the length of the column. The velocity maps shown in the contour plot

relative to z = 26 *mm* until z = 123 *mm* were found to be very similar with a maximum velocity equal to $0.45U_{tip}$ and a minimum calculated velocity of approximately $0.15U_{tip}$. The first plane found at z = 9 *mm* on the other hand, has a maximum velocity above $0.5U_{tip}$ and the minimum, was never inferior of $0.3U_{tip}$. The fluid gel on the other hand, had significantly lower radial velocity profile throughout the pin stirrer, with maximum velocity only reaching $0.34U_{tip}$ and minimum measured near the outer wall, of $0.1U_{tip}$.

In the interest of proving a more quantitative description of the flow field for both runs, in Figure 5.14 plane corresponding to the 6th rotating pin (z = 90 *mm*) and the planes associated to the closest stationary pins (z = 82 *mm* and z = 98 *mm*) were chosen as reference to show the profiles of the azimuthally averaged radial velocity. In addition in Figure 5.14(g) and (h) are shown the radial velocity profile relative to the lowest rotational pin at z = 9 *mm*.

Figure 5.14 is arranged as a matrix, with the two columns contain the results for the two fluids, while each row is a different axial position. The differences in velocity profiles between the two fluids are evident for each z plane chosen, respectively Figure 5.14(a) and (e) for glycerol and Figure 5.14(b) and (f), but differ when compared to each other because of their different rheological behaviour and the phase change of the fluid gel.

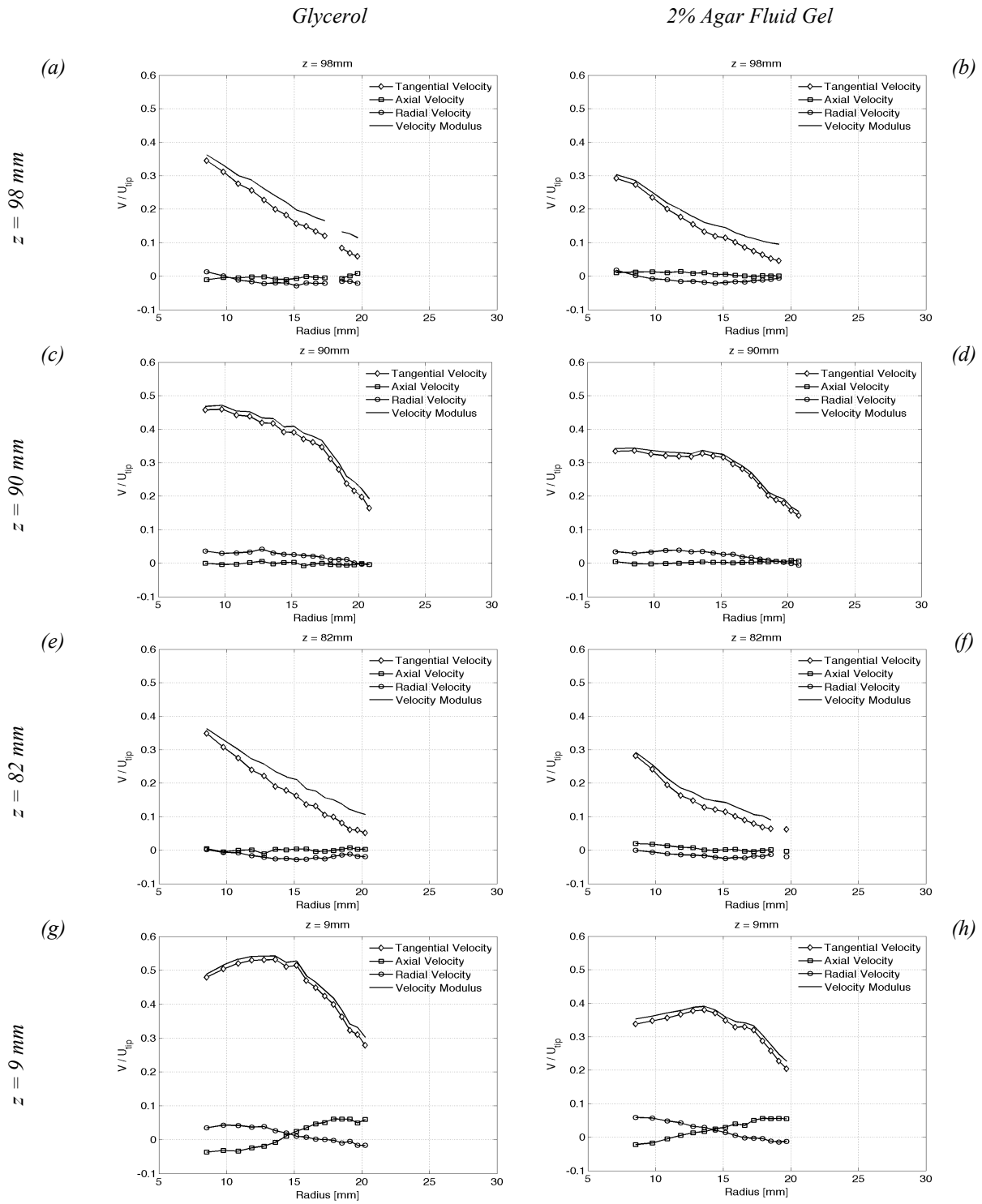

Figure 5.14: Glycerol and 2% Agar fluid gel azimuthally averaged radial velocity profiles. All the velocities are normalized by U_{tip}.

Glycerol for coordinates of $z = 98mm$ and $z = 82mm$ has the highest velocity in proximity of the shaft for $r = 7mm$, decreasing linearly with the radius. This characteristic velocity profile is almost completely due to the strong tangential component of the flow at these two coordinates, as a matter of a fact, both the axial and radial components are close to zero for any value of r.

The fluid gel on the other hand is a shear thinning fluid and as expected, had a different velocity profile. The effect of the shear-thinning behaviour of the fluid gel is shown in Figure 5.14 *(b)* and *(f)* where a moderate hyperbolic trend is observed.

The first compartment of the other hand found at $z = 9mm$ in stirrer, presents a unique characteristic of a strong recirculation, described by the velocity profiles in both Figure 5.14(g) and (h). The flow has negative axial component for values of $r < 15mm$, representing the downward movements induced by the first rotating pin. The downwards moving flow, is blocked by the base of the pin stirrer and forced to move back upward at $r > 15mm$. The characteristic radius of 15 mm is once again the determined by length of the rotating pins.

5.3.4. Shear rates

The formation of the fluid gel particles is directly controlled by the advection of the flow. One of the principal aims of this fluid dynamic study is to quantify the rate of shear. The shear rate is calculated from the velocity field, according to Eq. 3.9, is shown in Figure 5.15(a) and (b), using contour plots, similarly to the figures regarding the velocity. The contour plots shown in Figure 5.15(a) and (b) (respectively for glycerol and fluid gel), are azimuthally averaged, while Figure 5.15(c) reports the shear rate distributions calculated over the entire volume of the pin stirrer.

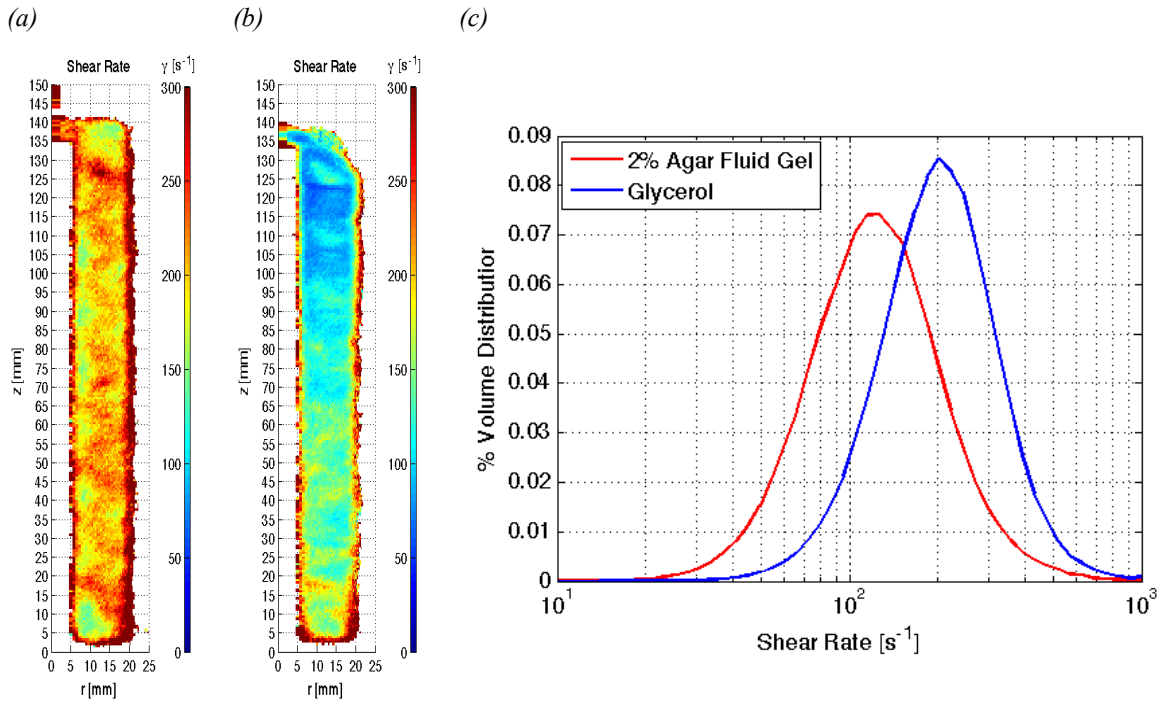

Figure 5.15: The azimuthally averaged contour plots of the shear rates measurements relative to glycerol in (a) and fluid gel in (b) and the relative volume distribution.

The glycerol contours plot in Figure 5.15(a) shows consistency in the intensity of the shear field at various heights within the column; mean while in Figure 5.15(b) the average values of shear drop quite drastically moving upwards in the column. In both cases the highest values are found along the pin stirrer wall, with values reaching $300s^{-1}$. In this region the tracer is forced to quick changes of direction, resulting in the increased shear. The centre of pin stirrer for a radial coordinate r that goes from $7mm$ to approximately $17mm$ is characterized by constant shear rate with values that vary between $150s^{-1}$ and $250s^{-1}$.

The fluid subject to the maximum shear rates was to be found in the 1.25 mm gap between the tip of the pin and the outer wall. In this region, the impeller has the highest tangential velocity, equal to the tip speed $U_{tip} = 1.74m\ s^{-1}$. The maximum shear rate can be estimated as the ratio between the length of the gap and the tip velocity and it was found to be approximately of $1250s^{-1}$, this value is in excellent agreement with the values of shear rate calculated from the *PEPT* data and reported in Figure 5.15.

The shear rates calculated for the first compartment of the pin stirrer in the glycerol experiment, Figure 5.15(a) confirms the assumptions proposed after analysing the velocity contour plots in Figure 5.9. During this experiment, the lowest levels of shear rate, were found in correspondence of the highest velocity. Since the shear rate is defined, as the change in velocity along certain directions; the highest velocity measured in the first compartment also correspond to the least mutable. The rate of shear rate in this area drops to a value of $\approx 100\ s^{-1}$.

The fluid gel contour map of the shear rates is shown in Figure 5.15(b) and appears substantially different from the glycerol. The shear rate values are significantly lower in the upper region of the column, but rise in magnitude in the initial stages of the pin stirrer, until reaching near the inlet intensity similar to those found for glycerol. The pins within the unit, during the gelation, are capable of establishing a shear rate, rarely higher than 200 s^{-1} and as low as $15 s^{-1}$, these values are found respectively for z = 10 *mm* and z = 130 *mm* and r measured between 7 *mm* and 17 *mm*. The high values of shear rates reported along the wall of the pin stirrer are due to rapid changes in direction of the tracer.

The viscosity is the measure of the resistance of the fluid to a deformation. Across the height of the pin stirrer, all the pins rotate with identical velocity, but areas of the flow that offer less resistance, less viscosity, are subjected to greater deformation. In other words, the higher values of shear rate found in proximity of the bottom of the pin stirrer are a consequence of the lower viscosity of the un-gelled biopolymer solution. Building on this argument, the differences between glycerol and fluid gel are easily explained, by referring to Figure 5.1.

In order to summarise the differences in terms of shear rates for the two fluids, Figure 5.15(c) shows their distributions. The average shear rate within the pin stirrer during the

glycerol experiment is 221s^{-1}; meanwhile for the fluid gel the mean shear rate drops to approximately 140s^{-1}.

	Mean, $\bar{\dot{\gamma}}$	Standard Deviation	Skewness	Time weighted Mean, $\bar{\dot{\gamma}}_t$
Glycerol	221.0973	109.3939	1.9080	198.43
2% Agar Fluid Gel	140.4033	83.6326	2.5260	110.12

*Table 5.1: Details about the Shear rate distributions presented in Figure 5.15.*Log-normal distributions have a skewness of zero, although distributions based on experimental measurements such those in Figure 5.15(c) may not always be perfectly symmetric. The skewness of the dataset is important because it describes whether deviations from the mean are going to be positive or negative. In Table 5.1 the skewness is positive for both fluids, meaning that the right tail is longer; the "mass" of the distribution is concentrated on the left of the figure.

The detailed description of the differences between the two distributions is reported in Table 5.1. The table also contains in the *4th* column the average time weighted shear rate, introduced in Eq. 5.2.

$$\bar{\dot{\gamma}}_t = \frac{\sum \dot{\gamma}(i,j)\delta t(i,j)}{\sum \delta t(i,j)} \qquad \text{Eq. 5.2}$$

The time weighted average shear rate takes into account the time spent by the tracer in each cell δt, and it is a more representative measure of the average shear experienced by the tracer. The time weighted mean shear rate, $\bar{\dot{\gamma}}_t$ is for both the glycerol and the fluid gel experiments significantly lower than the mean shear rate $\bar{\dot{\gamma}}$. The reason is that portions of the flow within the pin stirrer where the value of the shear rate is the highest are also characterized high velocities, thus lower time spend at that particular shear rate.

The important difference observed between the average shear rate and the time average, suggest the importance of considering "time" in approaching the an accurate characterization

of the pin stirrer. To effectively characterize the shear rate within the pin stirrer it is necessary, to understand both the shear field, and the local residence of the tracer anywhere in the unit.

5.3.5. Occupancy

Occupancy is the percentage of time that the tracer actually spends within a cell against the total experimental time. The routine *eulo.m* calculates two diverse kinds of occupancy.

The occupancy based on the number of passes; calculated as the percentage of the number of times the tracer crosses each cell over the total number of passes. This commonly used method for quantifying occupancy is misleading, because the number of passes does not satisfy the principle of occupancy. A contour plot of the number of passes does not distinguish between tracers that cross through a corner of the cell at high velocity (*low occupancy*) or a slow moving tracer passing diagonally through a cell (*high occupancy*). To overcome this problem, an advanced code was developed in MATLAB® within the *eulo.m* script. The code, computes in each cell the actual distance travelled by the tracer as a linear interpolation between two locations, following the 2D schematics shown in Figure 5.17.

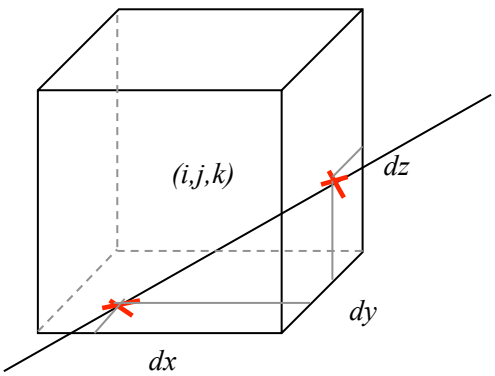

$$dist(i,j,k) = \sqrt{dx^2 + dz^2 + dy^2}$$

Figure 5.16: Enhanced accuracy occupancy algorithm developed for fast moving tracer.

The actual time that a tracer spends in a cell is thus calculated as shown by Eq. 5.3, with t_∞ representing the total experimental time.

$$\delta t(i,j,k) = dist(i,j,k)/v(i,j,k)$$
$$t_E = \frac{t_\infty}{N_{cells}} \qquad \text{Eq. 5.3}$$

Recently the occupancy from *PEPT* data has been normalized for comparison, by the total experimental time (Depypere, Pieters *et al.*, 2009). This technique has the drawback of being grid size depended. Smaller grid cells, result in a smaller occupancy. Guida, Nienow *et al.* (2010) gave a more accurate description of the occupancy, also discussed by Barigou, Chiti *et al*. (2009), where for cells that have equal volume, the problem is solved by using the ergodic time, t_E defined in Eq. 5.3.

The ergodic time represents the time that the tracer would spend in any cell if the flow was ergodic. In a single-phase system, such a condition implies an equal probability of tracer presence at every point in the flow. Ergodicity is a theoretical state, which can be approached only after an infinite tracking time. However, it can be mathematically shown that, if the probability of visit is sufficiently high everywhere, ergodicity can be safely assumed when the trajectory of the tracer is recorded over a sufficiently long time to achieve adequate data resolution in every region (Wittmer, Falk *et al.*, 1998).

The time spent by the tracer in each cell, is fundamental for the understanding of the local residence time of the fluid within the column and allows to reconstruct a shear rate history of the tracer. The results are shown in Figure 5.17 for glycerol and Figure 5.18 for fluid gel.

The number of passes and the time occupancies for glycerol are shown respectively in the two contours plots in Figure 5.17(a), (b). Figure 5.17(a) shows the tracer passing mostly from the centre of the available fluid space, for *r* within 10 *mm* and 17 *mm*. Although the tracer passes most often from the central area of the pin stirrer, the time occupancy shown in Figure 5.17(b) describes the tracer occupying the area of the pin stirrer at higher radial positions, *r* ≈17 *mm*. This is partially due to the fact that for a similar tangential velocity, for higher radial

coordinates the particle needs to travel a longer path in order to complete a revolution around the impeller. The histogram in Figure 5.17(c) describe the system as homogeneous along the axial coordinate *z*, with the tracer spending an equal time along any *z* position.

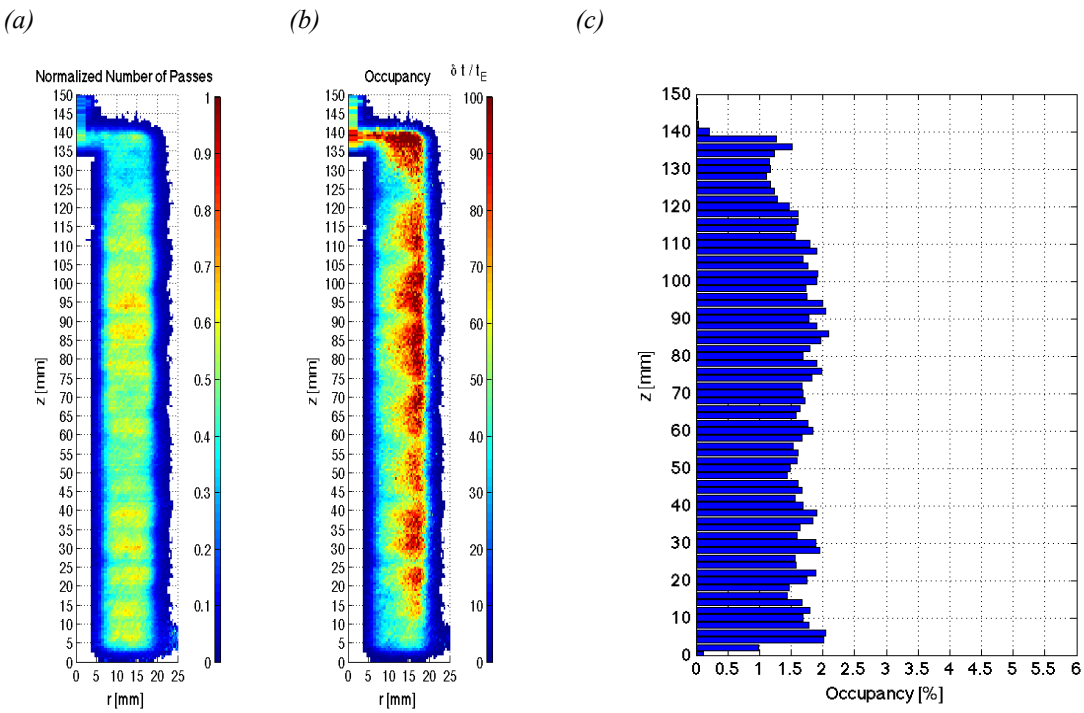

Figure 5.17: The contour plots in (a) and (b) are relative to the number of passes normalized by the maximum number of passes in the azimuthally averaged cells and the occupancy shown as sum of all the azimuthal values. In (c) the histogram of the occupancy for glycerol subdivided in to 2 mm bins.

The results of the study of the occupancy for the fluid gel experiment are shown in Figure 5.18(a), (b) and (c). Contrarily to what seen for the glycerol, the contour plot of the occupancy is less even. Figure 5.18(a) shows the normalized number of passes to have an evident maximum in the topmost compartment. One can see that as a consequence of the high number of passes at this coordinate, also the residence time occupancy shown in Figure 5.18(b) has a similar behaviour. The tracer resides preferentially in the vicinity of the top compartment of the pin-stirrer at z = 130 *mm* the occupancy was measured to be 200 times the ergotic time. Furthermore the value of the occupancy below z = 80 *mm*, decreases to values 50 times t_E, which are comparable to those obtained for the reference glycerol experiment.

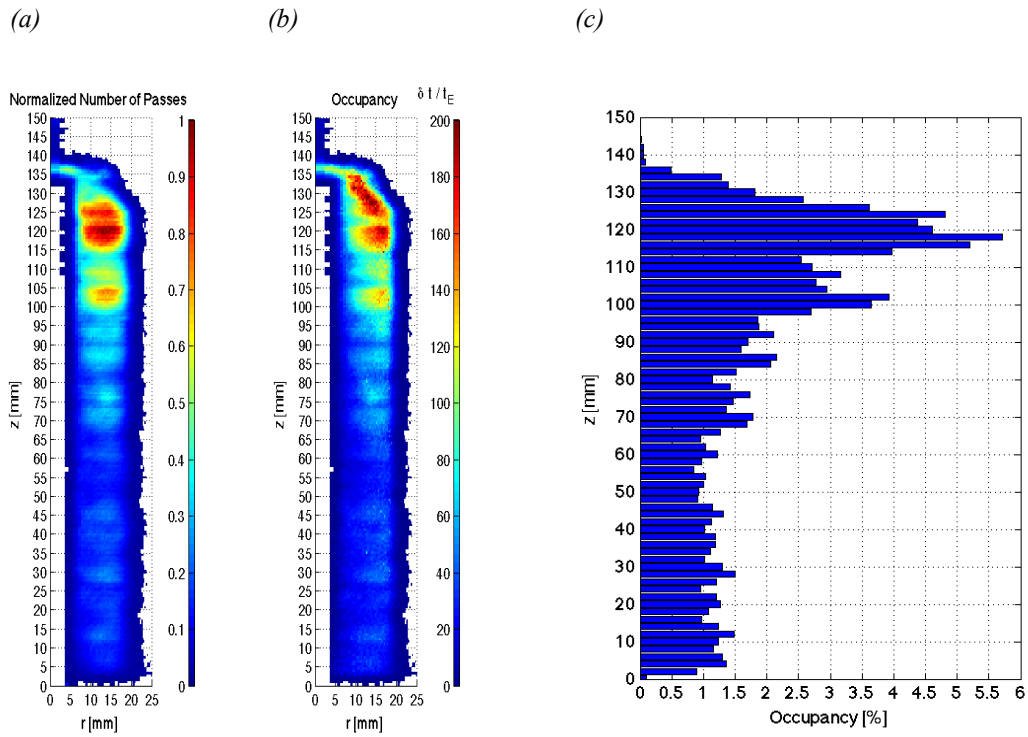

Figure 5.18: The contour plots in (a) and (b) are relative to the number of passes normalized by the maximum number of passes in the azimuthally averaged cells and the occupancy shown as sum of all the azimuthal values. In (c) the histogram of the occupancy for the 2% agar fluid gel subdivided in to 2 mm bins.

5.3.5.1. Formation of dead zones during the fluid gel experiment

The lack of data points in the top corner of the pin stirrer observed for the fluid gel experiment, Figure 5.18(a) and (b). Suggest the presence in this area of a dead zone, from which the tracer is excluded. The main hypothesises behind the formation of this area were, the formation of a fluid gel, with high yield stress that consequently behaved as a solid, or the accumulation of gelled biopolymer due to the low shear in this area.

Investigation carried out after each experiment proved the presence of a gelled ring of biopolymer in the area corresponding to the dead zone of Figure 5.18(a) and (b). Due to the invasive and disruptive nature of the procedure necessarily followed to disassemble the pin stirrer, it was not possible to carry out compression or rheological tests on the recovered

sample. The formation of the gelled biopolymer in this dead zone is assumed to be consequence of the early gelation of fresh biopolymer solution in the area of the pin stirrer characterized by a low shear Figure 5.15(a) and by referring to the schematics of the external jacket in Figure 3.3, also exposed to the lowest temperatures. Thus in the ideal conditions for the biopolymer to quiescently cool creating a gelled toroid.

5.3.6. Particle Shear Rate History

So far the Lagrangian particle paths, and the Eulerian maps were analysed and discussed separately. In the Eulerian description of the flow field, the flow quantities, such as velocity and rate of shear are a function of fixed position at a determined time. The Lagrangian study provided on the other hand unique information on the motion or trajectory of the tracer within the pin stirrer. In this section, the Lagrangian particle trajectories are overlapped to the Eulerian maps. These two, distinct approaches were used in combination to determine the shear rate history of the particle crossing each cell. This important parameter that controls the formation of the fluid gel particles, changes for different particle trajectories since each tracer follows a unique path.

Figure 5.19 shows the distributions of the shear history experienced by different tracers. The first two graph, Figure 5.19(a) and (b) respectively relative to the first 4 runs of glycerol and fluid gel, are calculated over the entire particle path from the entrance in the pin stirrer to the outlet. Figure 5.19(c) and (d) shows the particle shear rate distributions for glycerol and fluid gel relative to the initial 60 seconds.

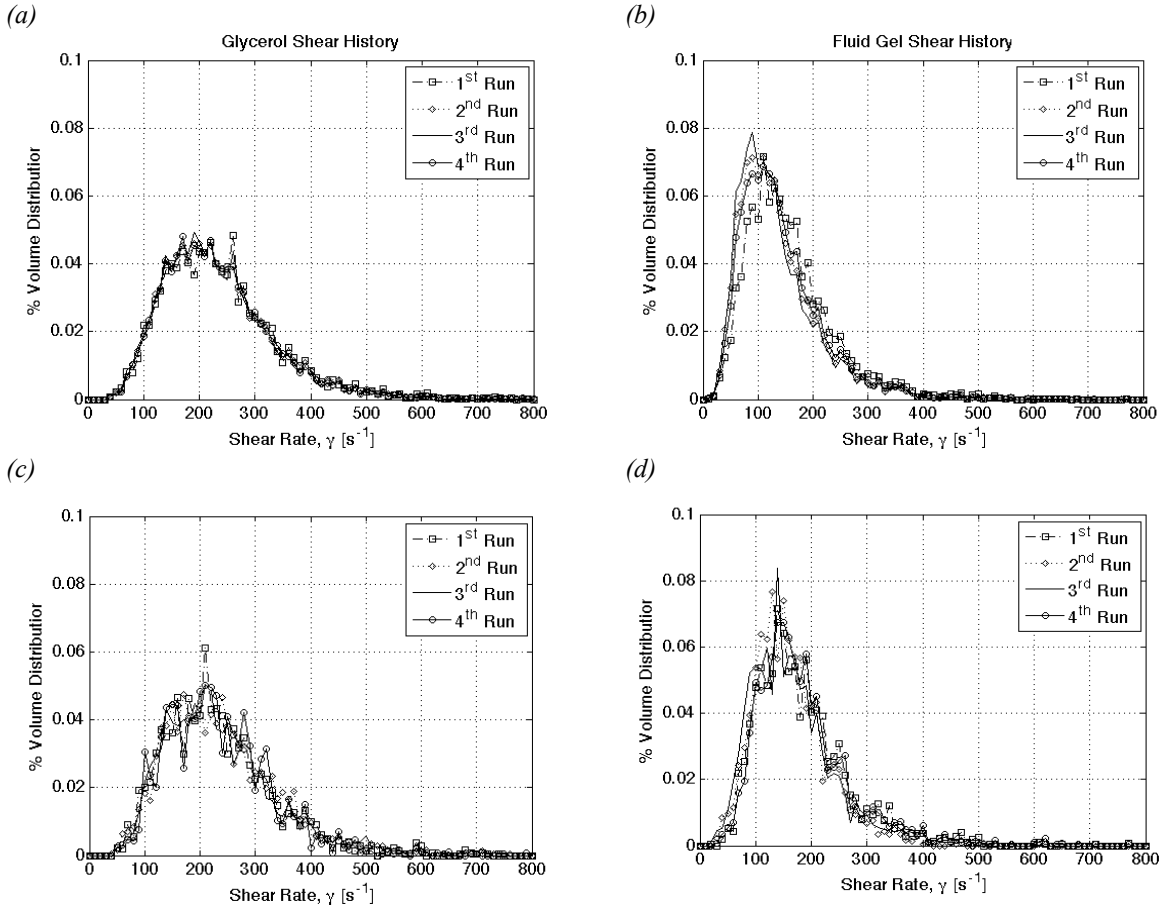

Figure 5.19: Distributions of the shear rates encountered along 4 particle paths. In (a) for glycerol, (b) for fluid gel along the full particle path length, while only along the initial 60 seconds in (c) for glycerol and (d) for fluid gel.

The shear histories distributions were found to be similar across different runs for glycerol in Figure 5.19(a) and fluid gel in Figure 5.19(b). Moreover, these distributions were also similar to the overall shear rates distributions presented in Figure 5.15(c), suggesting that the tracer visited most of the cells in the pin stirrer before exiting. As time progresses and the tracer travels further in the pin stirrer, also the shear rate history distributions across different runs become similar. In Figure 5.19(c) and (d) respectively for glycerol and fluid gel, are shown the particle shear rate history distributions relative to the initial 60 seconds after the tracer entered the pin stirrer. Although Figure 5.19(c) appears similar to Figure 5.19(a) and Figure 5.19(d) to Figure 5.19(b), differences can be described in terms of time weighted average shear rates as described by Eq. 5.2 and summarised in Table 5.2.

Run	Path length	1st	2nd	3rd	4th
Glycerol Shear Rate, $\overline{\dot{\gamma}_t}$ [s^{-1}]	Complete Path	213.6	211.8	216.3	218.2
	First 60 seconds	207.9	198.8	191.8	194.7
Fluid Gel Shear Rate, $\overline{\dot{\gamma}_t}$ [s^{-1}]	Complete Path	123.0	136.7	129.2	126.0
	First 60 seconds	136.7	169.9	153.3	147.7

Table 5.2: Time weighted average shear rates relative to the full shear history described in Figure 5.19. The shear rates were calculated according to Eq. 5.2

In Table 5.2 the time average shear rate, $\overline{\dot{\gamma}_t}$ experienced by the tracer for the 4 runs during the glycerol experiment are lower than the $\overline{\dot{\gamma}_t}$ relative to the complete run. The opposed trend was found for the experiment with fluid gel. The $\overline{\dot{\gamma}_t}$ relative to the first 60 seconds is higher than the $\overline{\dot{\gamma}_t}$ calculated over the complete particle path. The reason is the lower viscosity near the inlet. For instance, for the second run the shear in this region is as high as 169.9 s^{-1} compared to the average shear rate computed over the complete path of 136.7 s^{-1}.

5.4. Conclusions

PEPT allowed an in-depth study of the fluid dynamics within the pin-stirrer for glycerol and the 2% agar fluid gel. Strong similarities have been observed between the two particle paths, where both showed a predominantly rotating comportment. The sporadic events have been observed, where the displacements of fluid in the z direction, lead the tracer to move backwards towards the inlet. These changes in the height, leading to a change in compartment proved for both glycerol and fluid gel to be caused by local fluid dynamic conditions, and accountable for less than 15% of the total fluctuations of z across the rotating pin reference plane.

The velocity obtained opportunely deriving the location in time, reflects what described by observing the simple evolution of the locations of the tracer in time. The radial and axial components of the velocity show a significantly lower intensity compared to the tangential component, they highlight the areas responsible for the jumps in z. The proposed azimuthally averaged Eulerian plot of the axial velocity is also helpful in identifying the exact position of the rotating pins.

The Eulerian transform of the velocity obtained for the 2% agar fluid gel, highlighted an area in the top corner with missing information on the velocity. The tracer resulted to have never occupied this corner of the stirrer, indicating that the biopolymer gelled in this area of low velocity and low temperature, resulting in a reduced internal volume. The gelled biopolymer also acts as an obstacle for the tracer trying to flow towards the outlet. The gelled biopolymer in this area reduces the space for its passage; acting as a “filter” selectively blocking the tracer from flowing through the outlet and affecting the occupancy.

A main unexpected result and possibly the most important achievement of the comparison between glycerol and the fluid gel consist in the drastic difference in velocity profiles between the two experiments. This interesting observation suggests that the flow is not fully developed into turbulent conditions and the observed mixing is occurring under laminar conditions. This finding aids any future computational fluid dynamic simulation of the pin stirrer, producing more accurate results.

The shear rate is a more sensitive measure of the fluid dynamic conditions within the pin stirrer, because it implies computing the first derivative in space of the velocity components. These more significant changes in the local flow conditions, helped identify viscosity differences within the pin stirrer. Glycerol for instance showed a uniform and more homogeneous map of shear rate throughout the column. On the other hand because of the phase change of the biopolymer throughout the pin stirrer, the associated change in viscosity lead to a significant reduction of shear rate, between the bottom and the top of the pin stirrer. The transition between biopolymer solution and fluid gel appears gradual. In none of the two separate experiments the rate of shear exceeded 500 s^{-1}, with a time weighted average of 140 s^{-1} in the first 60 seconds of permanence within the pin stirrer.

Chapter 6.

A MODEL FOR FLUID GEL LUBRICATION

6.1. Introduction

The previous chapter proposed a description of the fluid dynamic properties within the pin stirrer heat exchanger, with particular attention to the rates of shear. This understanding is applied here, in order to engineer fluid gels with specific characteristics of size and elasticity.

The lubrication behaviour of these fluid gels is then carefully discussed focusing the considerations on the Stribeck curves. The lubricating mechanics of fluid gels particles are examined throughout this chapter. The concluding model for particle entrainment considers all the experimental evidences discussed.

6.2. Fluid gel particle sizes

Fluid gels produced (see Table 3.5) at a constant motor speed of 1450 rpm have all very similar particle sizes and size distributions (in Figure 6.1(a)). Conversely, decreasing the shaft speed of the pin-stirrer (in Figure 6.1(b)) results in fluid gels (all of the same 2% agarose concentration) of broader size distributions and larger mean diameters. What becomes apparent is that the mechanism of fluid gel formation greatly depends on the applied shear regime.

This is consistent with earlier studies (Norton, Jarvis *et al.*, 1999) where it was shown that the final particle size depends on the shear rate applied during the fluid gel formation process. More specifically, the mechanism of formation of the fluid gel particles is dictated by the ratio of the Brownian diffusion time over the time for convective movements in the shear flow, which is the inverse of the shear rate, $\dot{\gamma}$ (Brown, Cuttler *et al.*, 1990; Norton, Foster *et al.*, 1998). Fluid gels can be then produced either via spinodal decomposition, for a Peclet number >1 or via mechanically fracturing a system that is “trying” to form a stable matrix, for a Peclet

number <1 (Carvalho and Djabourov, 1997; Gabriele, Spyropoulos *et al.*, 2009). The "single-bell" shaped distribution curves shown in Figure 6.1, indicate that fluid gel formation in this study is driven by a single mechanism, and furthermore the fact that their Sauter mean diameter is approximately 110 μm, is consistent with particles produced with a Peclet number <1 as explained elsewhere (Ellis and Jacquier, 2009).

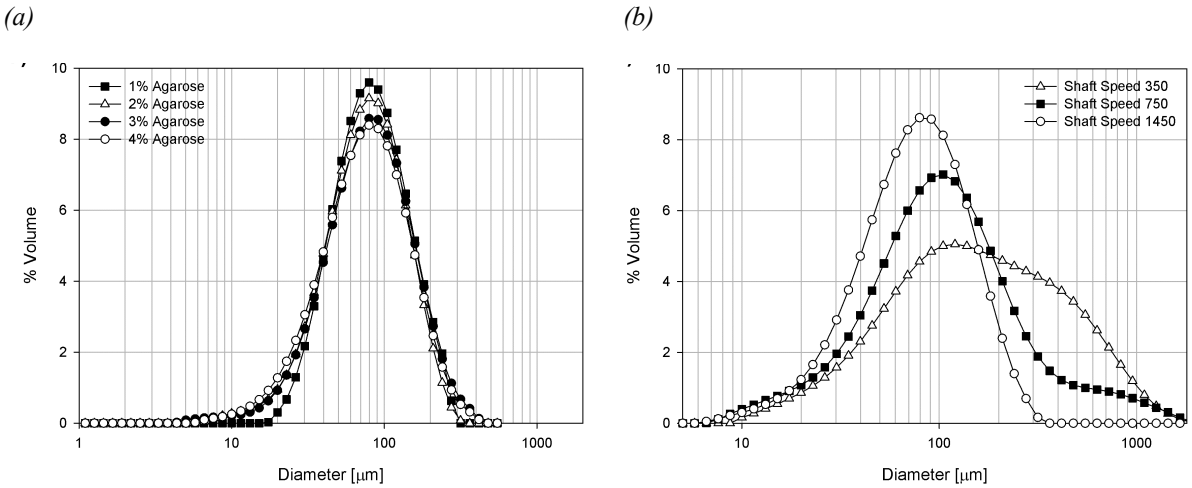

Figure 6.1:Particle size distributions of fluid gels (a) with varying agarose concentrations (1% - 4%), produced at a constant shaft speed of 1450 rpm, and fluid gels (b) with the same 2% agarose concentration, produced at variable shaft speeds.

According to the study carried out in the previous chapter, a difference in viscosity of the inlet solution will reflect in a difference in shear rates within the pin stirrer. The similarity between the distributions shown in Figure 6.1(a) suggest that the decrease in shear rates due to the increase in viscosity, is not sufficient to significantly modify the final particle size distribution. The particle size is influenced by the shear rate in the early stages of gelation. The similarities in terms of particle size therefore can only be interpreted as a similar shear conditions in this area during the gelation, possibly caused by the onset of turbulent conditions.

On the other hand, by changing the shaft rotational speed, the change in average particle size seems significant. According to Metzner and Otto (1957), the correlation for the agitation of non-Newtonian fluids, the average rate of shear decreases proportionally to the shaft speed.

Metzner and Otto (1957) obtained for a shear thinning solution of 2.5% CMC a proportionality constant $k_{MO} = 13$. In terms of shear, a change of shaft speed from 1450 *rpm* to 750 *RPM*, is equal to an average 50% reduction in the rates of shear.

6.3. Fluid gel particle elasticity and rheology

The textural properties (deformation/elasticity) of each of the particles in a fluid gel system have been previously shown to be the same as those of a quiescently cooled gel of the same hydrocolloid concentration.(Frith, Garijo *et al.*, 2002) Therefore, in the present study, texture analysis was performed on quiescently cooled agarose gel systems (Figure 6.2) and the obtained behaviour was adopted as that of the individual particles of fluid gels with the same agarose concentration.

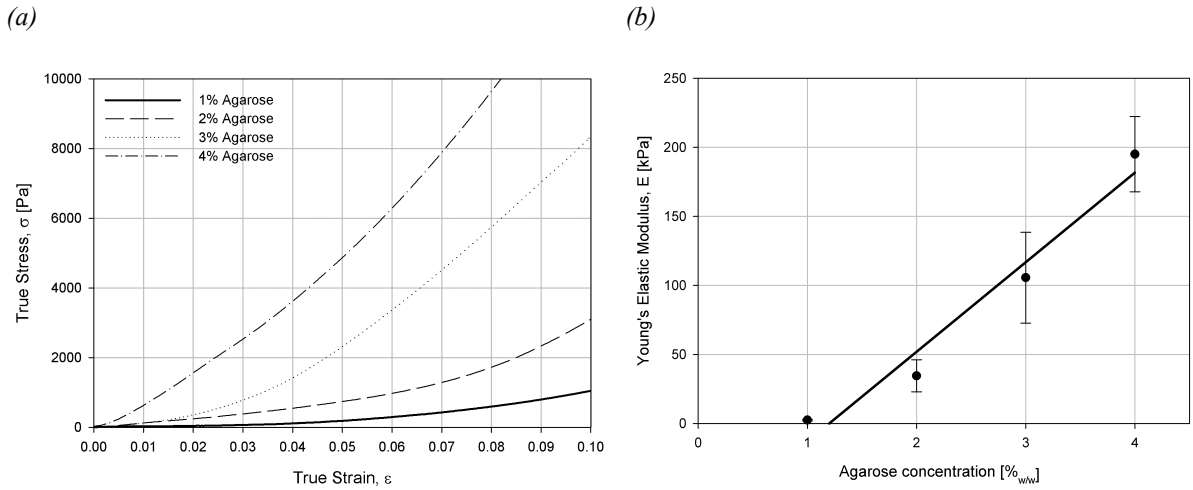

Figure 6.2:Texture analysis of the investigated fluid gels. (a) True stress versus true strain curves as a function of agarose concentration. (b) Young's elastic modulus E as a function of agarose concentration. The linear regression shown in (b) is described by f(x) =-77.89 + 64.89x

Figure 6.2 shows that increasing the agarose concentration in the system results in an increased elastic modulus for the individual fluid gel particles. Despite the isotropic nature of the gel network, the measured samples exhibit a non-linear elastic behaviour over the tested range of strains. For this reason the Young's modulus (elasticity) for each of the samples is calculated as the slope of the initial linear region of the true stress (σ) true strain (ε) curves.

The obtained Young's modulus data were found to linearly depend on the agarose concentration in the system (Figure 6.2(b)), in agreement to what has been reported elsewhere (for example Ellis and Jacquier, 2009).

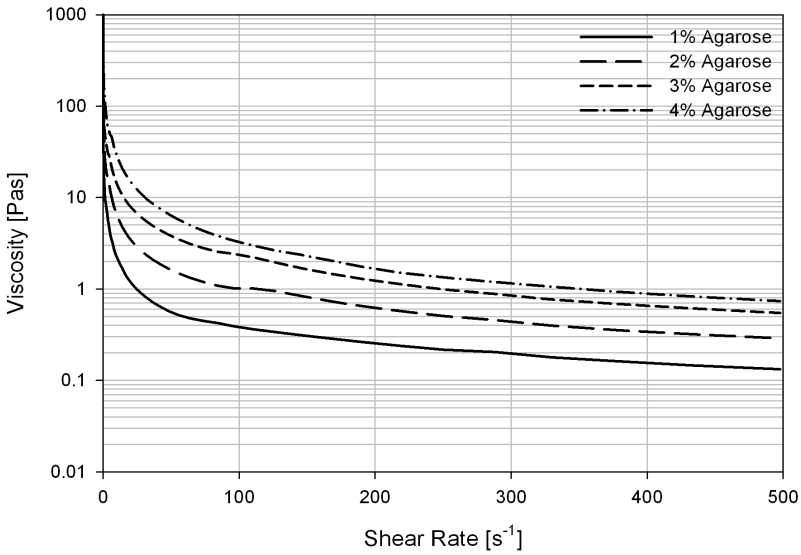

Figure 6.3:Rheological behaviour (flow curves) of fluid gels as a function of agarose concentration.

The bulk rheology of the agarose fluid gels will be affected by particle elasticity. For non-ionic fluid gels particle-particle interactions are only due to week Van der Waals forces. As a result the flow behaviour of these systems is mainly dictated by particle elasticity, resisting the deformation. Because the particle elasticity is linearly proportional to the agarose concentration, the increase in viscosity due to agarose concentration, shown in Figure 6.3, can be related to and increase in particle elasticity. The particulate nature of the fluid gels is reflected by the strong shear thinning behaviour and the yield stress as shown in Table 6.1.

$\eta = K\,\dot{\gamma}^{n}$	**K [Pa.s^{n+1}]**	***n*** **[]**	**R^2**	**τ_0 [Pa]**
1% Agarose	13.2	-0.74	0.998	2.3
2% Agarose	41.2	-0.80	0.989	7.5
3% Agarose	97.6	-0.82	0.995	31.6
4% Agarose	261.8	-0.90	0.994	55.4

Table 6.1:Power-law dependency of the rheological behaviour of agarose fluid gels and the corresponding zero yield stress, τ_0, calculated by extrapolating to zero shear stress. K and n are the consistency constant and power-law index, respectively.

6.4. Tribology of fluid gels

A series of tribology experiments were carried out in order to investigate the lubrication properties of agarose fluid gels as a function of hydrocolloid concentration in the system; the obtained data, for a normal load *W* of 4 *N*, are given in Figure 6.4.

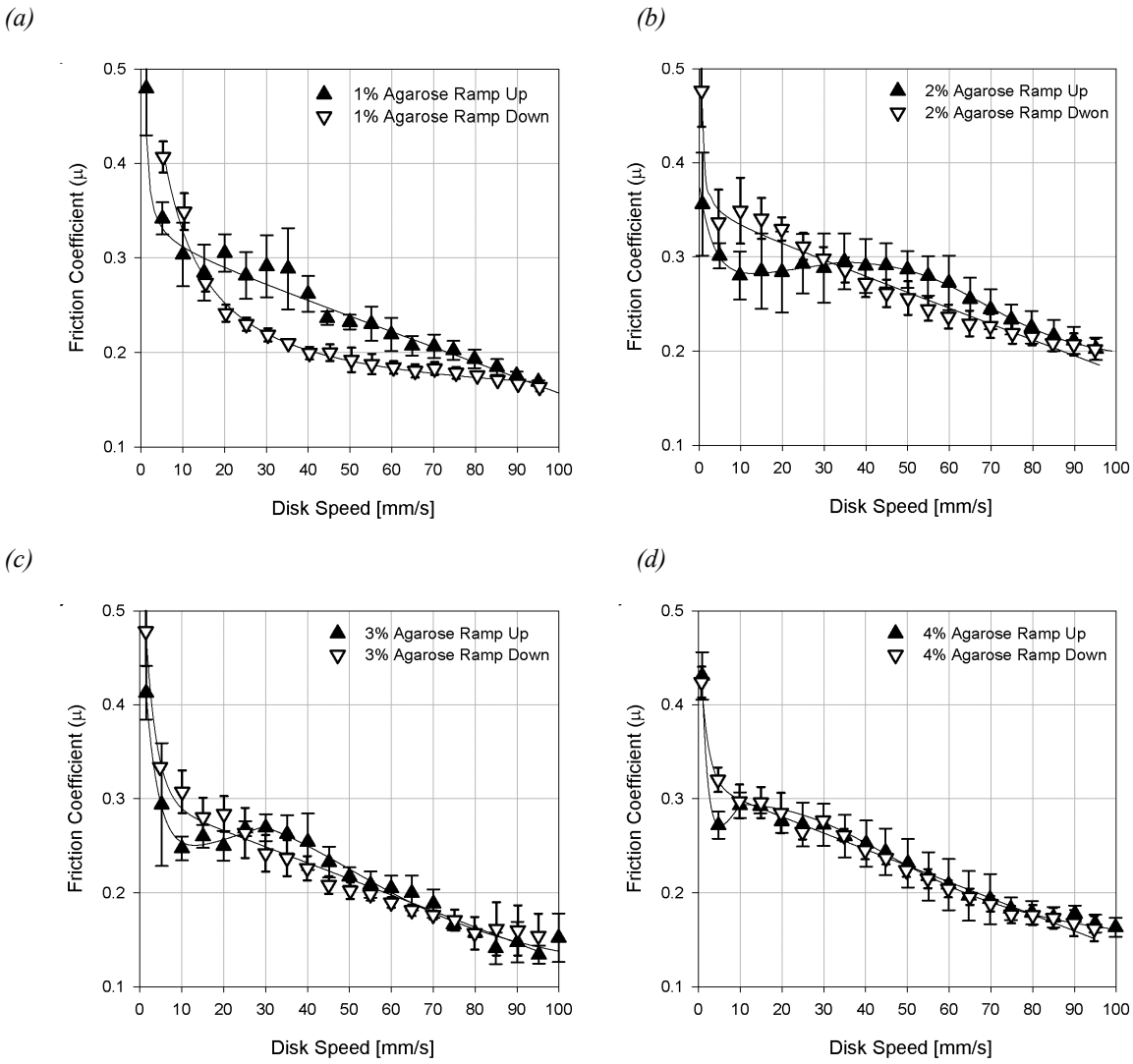

Figure 6.4:Stribeck curves, for increasing (open symbols) and decreasing (filled symbols) disk velocity ramps, displaying the tribological behaviour of fluid gels with agarose concentrations of (a) 1%, (b) 2%, (c) 3% and (d) 4%. For all the tests shown the applied normal load W was kept constant at 4N. Friction coefficient data points are average values of at least three repetitions while the solid lines only serve to guide the reader's eye.

The friction coefficient data (μ_F, see Eq. 2.7), as measured for initially increasing (ramp-up) and subsequently decreasing (ramp-down) disk speeds U, clearly exhibit a behaviour that is dependent on agarose concentration in the fluid gel system. Furthermore there seems to be a hysteresis between the ramp-up and the ramp-down tests, the extent of which is also concentration dependent; higher agarose concentrations lead to a less pronounced hysteresis. As oppose to the "smooth" behaviour observed in the ramp-down experiments, for all tested agarose concentrations (Figure 6.4), the behaviour during the ramp-up in speed exhibits a somewhat unusual behaviour. More specifically, for all systems there is initially a decrease in friction as the disk speed increases to ≈10 $mm\ s^{-1}$ (Figure 6.4). Increasing the disk speed further, results in a local maximum in friction for all systems except the 1% agarose fluid gel, as shown in Figure 6.4(b) - (d). The disk speed, at which this temporary increase in friction occurs, depends on the agarose concentration in the system and in fact its value decreases as the hydrocolloid concentration in the system is increased. Finally, for even higher disk speeds (above ≈40 $mm\ s^{-1}$) the friction coefficient of all fluid gels begins to decrease again, a trend that the system maintains all the way up to the maximum tested disk speeds (Figure 6.4).

The dependence of friction on the direction of the applied speed ramp, as identified for the systems in this study, has not been previously observed in terms of "classical" tribology (Halling, 1975); the term "classical" tribology refers to friction coefficient data obtained as a function of disk speed for Newtonian isotropic lubricants (*i.e.* oil, emulsions, biopolymer solutions). The trend exhibited by the friction data in the ramp-up tests is also different from what has been previously reported (Yakubov, McColl *et al.*, 2009). Classical tribology studies have shown that friction decreases in the mixed lubrication regime, with increasing disk speeds, a trend that is usually followed by a minimum in the friction values as the system enters the hydrodynamic region and μ_F increases. In contrast, data on the lubrication

properties of fluid gels shown here exhibit a maximum friction coefficient value in the mixed lubrication region.

The minimum in the friction values (in the mixed lubrication regime) reported in classical tribology studies can be explained by the Reynolds equations, used to describe the fluid dynamics of the entrainment mechanism, and it has been suggested to be a result of the positive pressure gradient created by the increasing disk speed U (Gohar, 2001). As U increases, the entrained lubricant reduces the contact of the surfaces' asperities ("roughness"), until the limiting condition of fully separated surfaces is reached. Subsequently, further increase in U, results in an increase in the friction coefficient, which is entirely dependant on the fluid dynamic properties of the lubricant.

6.4.1. Film thickness

In the past 50 years a series of semi empirical equations have been developed in order to calculate the film height of the entrained fluid for a range of elastohydrodynamic lubrication (EHL) conditions, where the elastic deformation of the lubricated surfaces becomes significant (Hamrock, 1994). Under these conditions the effect of the entrained fluid on friction is determined by the Hertzian Contact theory and the Reynolds transport equation. Dowson and Higginson (1959) numerically derived a semi-empirical equation to calculate the film thickness during lubrication by differentiating the Reynolds equation. Based on this early work first Johnson (1970) and then Esfahanian and Hamrock (1991) proved the effectiveness in predicting the gap size improving and revisiting the model for soft-EHL (Hamrock and Dowson, 1978).

More recently, de Vicente, Stokes *et al.* (2005) calculated the film thickness (h_{min}) during lubrication using the semi-empirical equation proposed by Esfahanian and Hamrock (1991) given below:

$$h_{min} = 3.27(\eta \cdot U)^{0.66} \cdot W^{-0.21} \cdot E^{*-0.44} \cdot R^{0.768} \qquad \text{Eq. 6.1}$$

where η the viscosity of the "lubricant", U the disk speed, W the normal load, E^* the reduced material elasticity and R the ball radius. Eq. 6.1 can be used for the W and U used in this study.

However, the major limitation of Eq. 6.1 is that it was developed for Newtonian fluids. To adapt Eq. 6.1 to the shear thinning rheology shown by the fluid gels, the constants W, E^* and R have been grouped into a single constant b, as shown in Eq. 6.4.

$$h_{min} = b(\eta \cdot U)^a, \quad \text{with } b = 3.27W^{-0.21} \cdot E^{*-0.44} \cdot R^{0.768} \qquad \text{Eq. 6.2}$$

Assuming that the contact area between the soft ball and the disk as a flat surface, the shear rate ($\dot{\gamma}$) in the contact region can be described by:

$$\dot{\gamma} = \frac{U}{h_{min}} \qquad \text{Eq. 6.3}$$

This assumption, allows the use of the experimentally obtained viscosity values (Table 6.1) to derive a bulk rheology dependent thin-film thickness h_{min}^R:

$$h_{min}^R = \left(b \cdot k^a\right)^{\left(\frac{1}{a \cdot n+1}\right)} \cdot U^{\frac{a(n+1)}{a \cdot n+1}} \qquad \text{Eq. 6.4}$$

where k is the consistency constant and the shear thinning behaviour is taken into account by the exponential term n. Note that for a Newtonian fluid (n=1) Eq. 6.4 is reduced to Eq. 6.2.

Eq. 6.4 is plotted in Figure 6.5, as a function of agarose concentration in the fluid gels, where the relationship between the disk speed U and the bulk rheology dependent thin-film thickness h_{min}^R can be clearly observed. For all agarose concentrations Eq. 6.4 predicts an increase in the minimum film thickness as the disk speed is increased. Nonetheless it also

appears that the predicted range of film thicknesses (for example 1.5 - 3μm for a system of 4% alginate concentration) is much smaller than the experimentally obtained particle size of the fluid gels (~80μm for the 4% agarose system, see Figure 6.1). This large difference between the two size scales would imply that entrainment of the fluid gel particles does not take place, a suggestion which contradicts what was experimentally observed in Figure 6.4. In these conditions standard EHL theory applies with limitations.

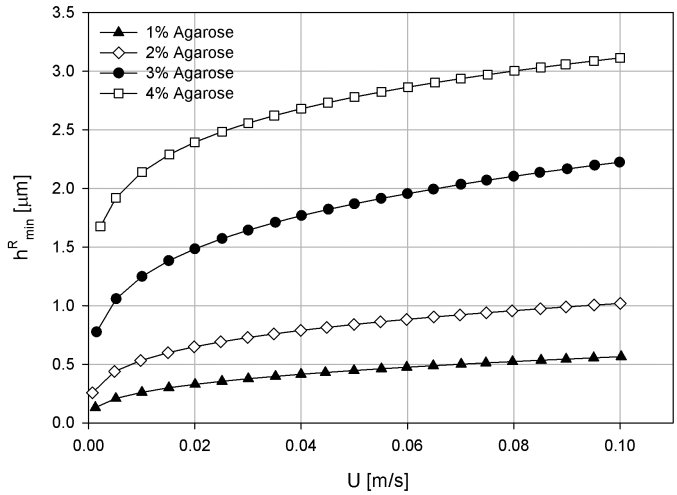

Figure 6.5: Minimum film thickness h^R_{min} function of the disk speed obtained from Eq. 6.4

6.4.2. The entrainment mechanism and entrainment velocity U_{entr}

The mechanism of entrainment of the fluid gel systems studied here is expected to be different. Starting from a static condition where there is no relative motion ($U \cong 0$), neither the fluid gel particles nor the fluid medium are present in the gap between the ball and the disk which are in dry contact. Under these conditions entrainment is prevented by the normal load applied on the ball. As the velocity progressively increases, a condition of selective entrainment begins to establish. At this stage, the fluid surrounding the particles (fluid medium) is driven in the gap, under the increasing pressure gradient described by the Reynolds equation (Gohar, 2001). Entrainment of the fluid medium is therefore driven by the

increasing speed, while entrainment of the fluid gel particles at this stage is hindered. This mechanism is schematically shown in Figure 6.6(a) (Zone A).

As the velocity is further increased, the fluid gel particles are gradually allowed in the gap (Figure 6.6(a), Zone B), which results in an increase in the measured friction coefficient values (Figure 6.4 (b) and (c)). The gap size at this stage is of the same scale as the size of the particles being entrained; realistically only a monolayer of fluid gel particles is expected to separate the ball from the disk. De Wijk and Prinz (2005) have previously described how particles alone can be responsible for holding non-conforming surfaces apart which can result in a higher friction coefficient.(de Wijk and Prinz, 2005) The mechanism of lubrication provided by the system shifts from film lubrication, to a lubrication regime provided by the rolling/sliding of the particles between the two surfaces, which appears to be responsible for the increase in the friction coefficient, as shown in Figure 6.6(a) (Zone B).

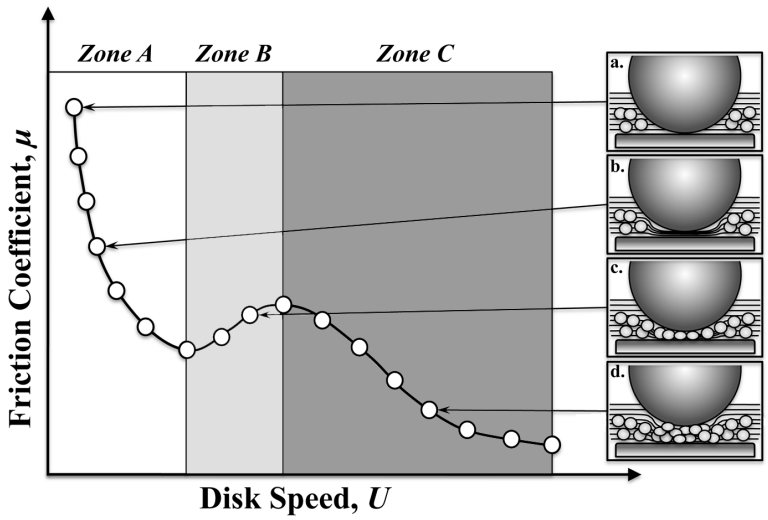

Figure 6.6: Schematic representation of the proposed mechanism of fluid gel lubrication. Zone A: the disk speed U is not high enough to induce entrainment of the particles; under these velocity conditions, only the fluid medium can access the gap between the ball and disk (a and b). Zone B: U is high enough to induce the onset of the entrainment of the particles, which results in an increase in the values of the friction coefficient μ; the gap between the ball and disk is similar to the size of the particles (c). Zone C: further increase in U allows for more particles to be entrained, which increases the gap between the surfaces above the dimensions of the particles and as a result μ again decreases with U (d).

Finally, for even higher speeds, an increasing number of fluid gel particles become entrained between the ball and the disk. Lubrication under these velocity conditions is now expected to be provided by multilayers of particles, which force the two surfaces further apart Figure 6.6(a) (Zone C). As a result the lubricating film thickness is much larger in comparison to the size of individual fluid gel particles, which suggests that the mechanism of film lubrication (as discussed for Zone A of the schematic in Figure 6.6(a)) is restored. The proposed mechanism is in agreement with the experimentally observed decrease in the friction coefficient of the system that occurs at high disk speeds (Figure 6.4).

As discussed earlier the starting position for the ramp-up (in velocity) tribology tests (open symbols in Figure 6.4) is a static condition of no relative motion ($U \cong 0$), where the ball and the disk are in dry contact. However, the starting position for the ramp-down tribology tests (filled symbols in Figure 6.4) is very much different as the two surfaces are now well separated by either the fluid medium (system shown in Figure 6.4(a)) or by the fluid gel particles (system shown in Figure 6.4(b) – (d)), already fully entrained in the gap. In this case, and as the velocity decreases, entrainment of the particles (or that of the fluid medium) is increasingly disfavoured. As a result the thickness between the ball and the disk becomes gradually smaller and the friction coefficient is increased (Figure 6.4). When the velocity U is reduced below a certain critical value it is expected that entrainment of the particles does not take place at all and eventually, as U approaches zero, the two surfaces will come into contact.

The mechanism proposed here is similar to what has been recently described by Meeker, Bonnecaze *et al*. (2004). In their study, the authors demonstrated, both mathematically and experimentally, that a micro-elastohydrodynamic lubrication (*EHL*) regime establishes between microparticles, present in a suspension of high (particle) phase volume, and the surface(s) involved. They further argued that surface roughness, particle elasticity and the

lubrication layer between the particle(s) and the surface(s) determines the local fluid dynamics.

The suggestion that the behaviour of a thin monolayer of particles, during lubrication, is affected by the elasticity of the particles, is in agreement with the experimental findings in the present study. The elasticity of the agarose fluid gel particles seems to affect the "critical" velocity (U_{entr}) under which these particles become fully entrained; as proposed earlier, entrainment of the particles takes place for those disk speeds where there is a maximum in the friction coefficient values (Zone B in Figure 6.6). From Figure 6.4 it becomes evident that as the elasticity of the particles is increased (from the 2% to the 4% agarose fluid gels), the value of the U_{entr} velocity, required to induce entrainment of the particles, is reduced. For example the U_{entr} for the 3% agarose fluid gel (Figure 6.4(c), is $\approx 30\ mm\ s^{-1}$, while, for the 4% agarose fluid gel (Figure 6.4(d), is in the order of $\approx 10\ mm\ s^{-1}$.

As a matter of a fact the entrainment of fluid gel particles takes place at higher velocities, as the applied normal load is increased, also explains why there is no particle entrainment detected (within the tested range of disk speeds) for the 1% agarose fluid gel system when a 4*N* normal load was applied (Figure 6.4(a)). It appears that, under these conditions of normal load, the velocities required to induce particle entrainment are higher than the range of those tested. When *W* is reduced to 1 *N* (Figure 6.7(c)), there is evidence that particle entrainment for the same system begins to take place; note the increase in the friction coefficient at intermediate velocities in Figure 6.7(c) a behaviour that is not observed when the applied normal load is increased from 1 *N* to 4 *N* (Figure 6.4(a)). Particle entrainment for this system is now detected since decreasing the applied normal load also leads to a lowering of the disk speed required to induce its (entrainment) onset.

(a) *6 Newton*

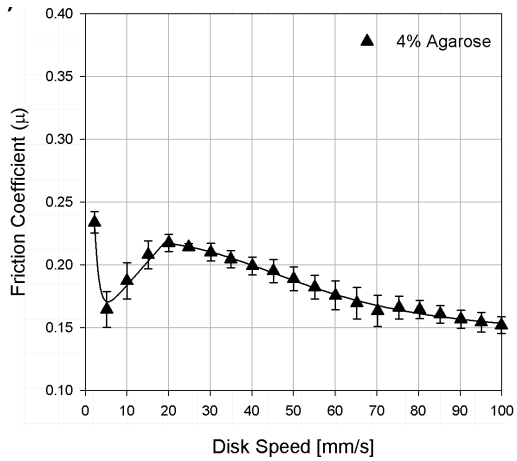

(b) *8 Newton*

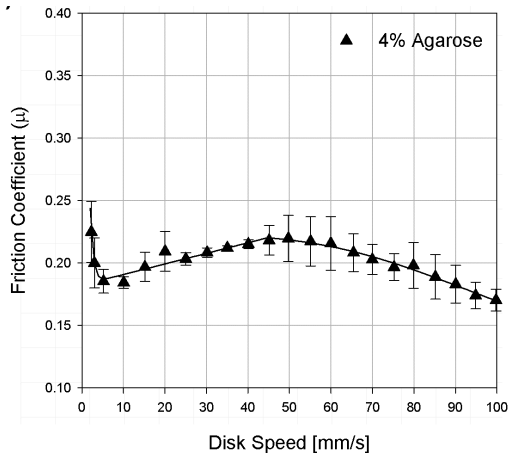

(c) *1 Newton*

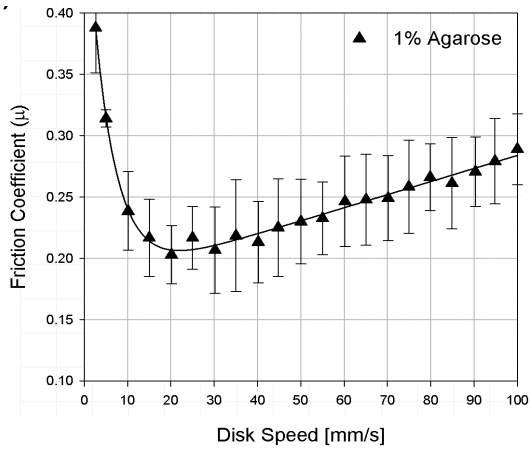

Figure 6.7: Effect of variations of the applied normal load W on the tribological behaviour of fluid gels. Stribeck curves for a 4% agarose concentration fluid gel with W of (a) 6 N and (b) 8 N, and (c) for a 1% agarose concentration fluid gel with W of 1 N.

It is important to emphasise that these observations are in agreement with what is proposed in this study regarding fluid gel lubrication, *i.e.* that the applied normal force (W) affects the onset of particle entrainment and that particle elasticity (E) affects the magnitude of the friction coefficient values (minimum and maximum friction) exhibited during the lubrication process. In terms of the "critical" velocity U_{entr}, under which the particles become fully entrained, the two parameters W and E mutually oppose each other; U_{entr} is proportional to the particles' elasticity (E) and inversely proportional to the applied normal load (W). The U_{entr} value can therefore be used as a system-specific parameter that "describes" the entrainment of the particles in the gap, and thus their overall lubrication behaviour.

$$U_{entr} \propto (E)^{\varepsilon} (W)^{-\omega} \qquad \text{Eq. 6.5}$$

6.5. Particle size effect on the lubrication

The effect of fluid gel particle size and size distribution on the lubrication properties of these systems has been investigated. The lubrication behaviour of the 2% agarose fluid gels with particle sizes shown in Figure 6.1(b) was monitored for a range of disk speeds and the obtained data are given in Figure 6.8. The experimental data revealed that decreasing the average size of the fluid gel particles results in an overall reduction in the friction coefficient of the system. This observation is in agreement with previous work on starch-containing custard desserts, with either added silica (sharp–Sil) or dynaseed (rounded–Dyn) particles, where the friction for the systems containing the smallest particles was lower than that of the systems containing the largest ones (de Wijk and Prinz, 2005).

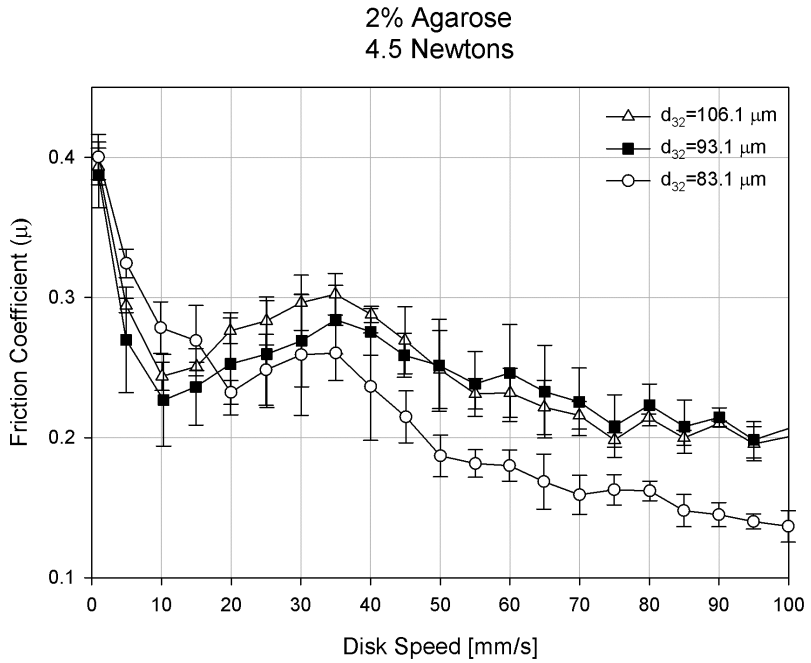

Figure 6.8: Effect of particle size on the lubrication properties of a 2% agarose fluid gel. Stribeck curves shown are for a normal load of 4.5 N.

At the initial stages of the lubrication process (for disk speeds up to ~20 $mm\ s^{-1}$) the friction coefficient of all three systems decreases with increasing speed and appears to be unaffected by the difference in particle size (Figure 6.8). As proposed earlier for this stage in the lubrication process, entrainment of fluid gel particles does not take place and therefore all tested systems are expected to behave in a similar manner. As U is further increased though, fluid gel particles start entering the gap between the ball and disk and as a result their friction profiles are now affected by the difference in their size. Interestingly enough all tested systems exhibit similar U_{entr} values (~35 $mm\ s^{-1}$), despite the fact that the corresponding friction values depend on the particle size of the fluid gel systems and are therefore different; friction values at U_{entr} increase with increasing particle size (Figure 6.8). The great similarity in the U_{entr} values for the systems further confirms that the critical entrainment speed for the fluid gel particles is only a function of their elasticity and the applied normal load. Finally for velocities greater than U_{entr} all fluid gel systems exhibit a steady decrease in friction with increasing disk speed, in agreement with the hypothesis proposed in this work.

6.6. Conclusions

The lubrication behaviour of agarose fluid gels has been investigated and a mechanism describing the lubrication process for these systems has been proposed. It was demonstrated that initially (at low disk speeds, $U < U_{entr}$) entrainment of the particles is restricted and friction decreases with increasing speeds only due to the presence of fluid medium in the gap between the ball and the disk. As U is further increased and approaches U_{entr}, particles begin to access the gap between the two surfaces and the system's friction is increased. Particles then become entrained at $U = U_{entr}$ at which stage a maximum in the measured friction coefficient is observed. Finally and as U becomes greater than U_{entr} the system's friction again begins to decrease as lubrication is now provided by multilayers of particles.

In addition it was established that the U_{entr} value is only dependent on the elasticity E of the particles and the normal load W applied during the lubrication process (see Eq. 6.5). Fluid gel systems of the same elasticity E but of different particle sizes displayed an overall reduction in friction with decreasing size; when subjected to a lubrication process of the same applied normal load W. The evidence presented in this study tends to suggest that the U_{entr} value of a fluid gel system (systems containing particles of the same dimensions) can be used as a descriptor of its overall lubrication behaviour.

Besides advancing the currently limited knowledge on the lubrication properties of fluid gels, the present work also provides insight into how novel products (based on fluid gel technology) that deliver an enhanced sensory perception, can be designed; for example by controlling the elasticity E of the fluid gel particles.

Chapter 7.

CONCLUSIONS AND FUTURE RECOMMENDATIONS

7.1. Conclusions

7.1.1. Fluid gels from Bio-Polyelectrolytes

- *κ-carrageenan based fluid gels were produced and their rheological properties fully investigated.*

The primary objective of this thesis was to investigate the design of fluid gel based microstructures with enhanced elastic and rheological properties for the use in food and personal care products. To the best of my knowledge no study considered the use of κ-carrageenan for fluid gels production has previously been reported. This thesis extends the knowledge in the field of fluid gels formed by spinodally decomposed bio-polyelectrolyte.

Similarly to the study carried out by Wolf, Scirocco, *et al*. in 2000, where the gelation was induced on mixtures of biopolymers, particular structures maybe formed by interfering with the gelation mechanism of non gelling molecules such as glycerol. Vast opportunities for the use of the fluid gels in consumer goods, specifically in skin creams are in their compatibility with other common constituents such as glycerol.

- *Particle shape and size are depended on the applied shear rates during the gelation in laminar flow.*

The fluid gel microstructures obtained exhibit properties depended not only on the initial chemical composition, but also on the process. For this reason, in order to control accurately the shear rates during the production of *κ*-carrageenan fluid gels, well-defined geometries were used. It was also proved that a regular particle size distribution with spherical and elliptical morphologies is achieved only for a Peclet number greater than one (Pe > 1). More specifically particles of elliptical and spherical morphologies (smaller than 5μm) can be produced by controlling the rates of two conflicting processes taking place during fluid gel

production; these are the rate of ordering of the helices in the flow, and the rate of deformation, defined as the rate of applied shear.

In high quality formulated products well-defined and homogeneously small particles are desirable. The limits in stability for obtaining such characteristics from fluid gels, need to be investigated further. While this work suggests the existence of a critical shear rate for the formation of spinodally decomposed particles at defined concentrations, a systematic study should identify limiting concentrations and shear rates.

- *κ-carrageenan fluid gels ripen due to lack of complete structuring during the shear process.*

Once formed the particles express a degree of ionic interaction or bridging, found to be function of the cooling time. Particles that are kept after the gelation, under a continuous shear field form fluid gels with weaker intra-particles bridges. Faster cooling on the other hand, proved to produce microstructures where the particles were tightly interlinked. Modifying process parameters during their production can therefore control the interactions and bridging between fluid gel particles. Therefore, without changing the material properties of the system, it is possible to design fluid gel microstructures with desired viscoelastic characteristics.

For a specific composition of biopolymer and salt, the kinetic of ripening of κ-carrageenan fluid gels were comparable to the rates of gelation under quiescent conditions. Evidence suggests that the concentration of salt and biopolymer play a big role in controlling the intra particle interactions. In fluid gels systems, higher concentrations of salt and biopolymer mean a faster kinetic. Increase in the ripening rate, discussed so far will be obtained by dosing of salt in the initial solution.

7.1.2. Fluid dynamic study of large scale fluid gel formation

- *The shear rates in the C-Unit can be measured using PEPT.*

The pin stirrer is entirely built in stainless steel and enclosed in a heating jacket. This typical design limits the techniques that can be used to experimentally quantify the flow within. Consequently, very little is present in literature describing the internal flow structures. This thesis for the first time proposes a complete fluid dynamic characterization of the pin stirrer by means of *PEPT*. In Chapter 5, the *PEPT* results are presented and discussed, initially for particle paths and consequently to the particles shear history which was found to be similar in magnitude for both fluids used. The experiment with glycerol showed to have the highest shear rates, 200 s^{-1} mean while an average shear rate of 140 s^{-1} was found for the 2% agar fluid gel. Custom made routines have been developed to overcome some of the limitations of the technique, such as the poor time resolutions and the in areas of high velocity gradients.

In the future the author recommends the approach taken in this thesis is followed and the programming routines available in Appendinx I to be used, when dealing with future *PEPT* studies of similar pin stirrers. The knowledge provided in this thesis can be used to design a second-generation of pin stirrer aimed at the production of the fluid gels. It is recommended to modify the design, in order to reduce the areas of lower shear, where the quiescent gelation of the biopolymer is facilitated.

- *Exlusion of the tracer from specific areas of the pin stirrer due to localized gelation.*

This fluid dynamic study has been carried out to understand the limitations of the model pin-stirrer and the differences in the flow patterns when two fluids with different viscosities were used. As described in Chapter 5, a lack of data points during the *PEPT* experiment with

fluid gel in the top corners of the pin stirrer, indicate the presence of a quiescently gelled biopolymer, not observed for glycerol. The combined use of the Newtonian glycerol and shear thinning agar fluid gel, has allowed observing typical fluid flow patterns due to the internal geometry of the pin stirrer, suggesting design improvements.

- *The differences in the velociteis calculated from PEPT data, suggest the flow is in laminar regime*

The Eulerian velocity plots obtained from the Lagrangian data, have given a quantitative understanding to the mixing regime within the pin stirrer. Both glycerol and Fluid gel have radial and axial components of the velocity one order of magnitude lower than the tangential component. The difference in velocity profiles between the two experiments, suggest the flow regime to be laminar.

Previous complex computational fluid dynamic simulations of the pin stirrer, can now be safely run with assumptions based on the experimental data presented in this thesis. Running the *CFD* simulations or designing further experiments, should consider the laminar regime of the flow within the pin stirrer.

7.1.3. Fluid gels Tribology

- *Particles are excluded from the gap in the tribology experiments at low velocities. They are entrained at higher rates and are responsible for increase in the friction coefficient.*

The lubricating properties of fluid gels and more in general of pastes of soft particles, was studied. The fluid gel particles have a fundamental role in the lubrication of sliding non-conforming surfaces. Tribological measurements showed that for low sliding velocities, typically with velocity inferior of a critical entrainment velocity, the particles are excluded from the gap. For this condition, an increase in velocity was shown to produce a consistent

decrease in friction. Higher sliding velocities, in accord with the Reynolds lubrication equation induce a decrease in pressure in the lubrication contact area. This change in pressure, is responsible for the entrainment at higher velocities of a monolayer of particles. This layer causes a localized increase in friction corresponding to a critical entrainment velocity U_{entr}. Further increase in velocity only produced a decrease in friction as more and more particles entered the gap.

The tribology experiments were carried out on a smooth *PMMA* surface. The author recommends that further work is done choosing different surfaces to used in the tribometer, in order to match more closely conditions naturally found in the oral cavity or skin. This should provide useful insight on the role of roughness on the entrainment of particles. Besides surface roughness, further studies should also cover the role played by surface elasticity as well as surface chemistry on the lubrication mechanism.

- *The friction coefficient of the fluid gels is depended on the ratio between the elasticity of the particles and the normal load applied.*

The critical velocity for the entrainment of the particles, in Chapter 6 as U_{entr}, was found to be proportional only to the group ($E^{\varepsilon}\ W^{-\omega}$) meanwhile a change in the particle size lead to a reduced overall friction coefficient when subjected to a lubrication process of the same applied normal load W. The evidence presented in this study tends to suggest that the U_{entr} value of a fluid gel system (systems containing particles of the same dimensions) can be used as a descriptor of its overall lubrication behaviour.

Besides advancing the currently limited knowledge on the lubrication properties of fluid gels and more in general of pastes, the present work also provides insight into how novel products (based on fluid gel technology) can be designed to deliver a controlled sensory perception. For example by controlling the elasticity E of the fluid gel particles.

Chapter 8.

References

Adams, M., B. Briscoe and S. Johnson (2007). "Friction and lubrication of human skin." Tribology Letters **26**(3): 239-253.

Agterof, W. G. M., G. E. J. Vaessen, G. A. A. V. Haagh, J. K. Klahn and J. J. M. Janssen (2003). "Prediction of emulsion particle sizes using a computational fluid dynamics approach." Colloids and Surfaces B: Biointerfaces **31**(1-4): 141-148.

Anderson, N. S., J. W. Campbell, M. M. Harding, D. A. Rees and J. W. B. Samuel (1969). "X-ray diffraction studies of polysaccharide sulphates: Double helix models for k- and i-carrageenans." Journal of Molecular Biology **45**(1): 85-88.

Anderson, N. S., T. C. S. Dolan and D. A. Rees (1968). "Carrageenans. Part III. Oxidative hydrolysis of methylated -carrageenan and evidence for a masked repeating structure." J. Chem. Soc., C.: 596-601.

Araki, C. (1937). "Acetylation of agar-like substances of Gelidium amansii L." J. Chem. Soc. Japan **58** 1362.

Araki, C. (1956). "Structure of the Agarose Constituent of Agar-agar." Bulletin of the Chemical Society of Japan **29**(4): 543 - 544.

Armisen, R., F. Galatas and S. A. Hispanagar (2000). Agar. Handbook of Hydrocolloids. G. O. Phillips and P. A. Williams, Woodhead Publishing**:** 21 - 40.

Arnott, S., A. Fulmer, W. E. Scott, I. C. M. Dea, R. Moorhouse and D. A. Rees (1974). "The agarose double helix and its function in agarose gel structure." Journal of Molecular Biology **90**(2): 269-272.

Austen, K. R. J., D. M. Goodall and I. T. Norton (1985). "Anion-independent conformational ordering in iota-carrageenan: Disorder-order equilibria and dynamics." Carbohydrate Research **140**(2): 251-262.

Austen, K. R. J., D. M. Goodall and I. T. Norton (1988). "Anion effects on equilibria and kinetics of the disorder-order transition of k-carrageenan." Biopolymers **27**(1): 139-155.

Bakalis, S., P. W. Cox, A. B. Russell, D. J. Parker and P. J. Fryer (2006). "Development and use of positron emitting particle tracking (PEPT) for velocity measurements in viscous fluids in pilot scale equipment." Chemical Engineering Science **61**(6): 1864-1877.

Bakalis, S., P. J. Fryer and D. J. Parker (2004). "Measuring velocity distributions of viscous fluids using positron emission particle tracking (PEPT)." AIChE Journal **50**(7): 1606-1613.

Barigou, M., F. Chiti, P. Pianko-Oprych, A. Guida, L. Adams, X. Fan, D. J. Parker and A. W. Nienow (2009). "Using Positron Emission Particle Tracking (PEPT) to Study Mixing in Stirred Vessels: Validation and Tackling Unsolved Problems in Opaque Systems." JOURNAL OF CHEMICAL ENGINEERING OF JAPAN **42**(11): 839-846.

Bertrand, J., J. P. Couderc and H. Angelino (1980). "Power consumption, pumping capacity and turbulence intensity in baffled stirred tanks: Comparison between several turbines." Chemical Engineering Science **35**(10): 2157-2163.

Bett, K. E. and J. B. Cappi (1965). "Effect of Pressure on the Viscosity of Water." Nature **207**(4997): 620-621.

Bialek, J. M., M. G. Jones and I. T. Norton (2000). Pourable edible aqueous-continuous emulsions. d. o. C. Lipton, Inc. (Englewood Cliffs, NJ). United States. **6136363**.

Bird, R. B., W. E. Stewart and E. N. Lightfoot (2002). Transport Phenomena, John Wiley & Sons.

Bongaerts, J. H. H., K. Fourtouni and J. R. Stokes (2007). "Soft-tribology: Lubrication in a compliant PDMS-PDMS contact." Tribology International **40**(10-12): 1531-1542.

Broadbent, C. J., J. Bridgwater and D. J. Parker (1995). "The effect of fill level on powder mixer performance using a positron camera." The Chemical Engineering Journal and the Biochemical Engineering Journal **56**(3): 119-125.

Brown, C. R. T., A. N. Cuttler and I. T. Norton (1990). Liquid based composition comprising gelling polysaccharide capable of forming a reversible and a method for preparing such

composition. European, UNILEVER PLC (Unilever House Blackfriars P.O. Box 68, London, EC4P 4BQ, GB)

Brummer, R. and S. Godersky (1999). "Rheological studies to objectify sensations occurring when cosmetic emulsions are applied to the skin." Colloids and Surfaces A: Physicochemical and Engineering Aspects **152**(1-2): 89-94.

Bryce, T. A., A. H. Clark, D. A. Rees and D. S. Reid (1982). "Concentration Dependence of the Order-Disorder Transition of Carrageenans. Further Confirmatory Evidence for the Double Helix in Solution." European Journal of Biochemistry **122**(1): 63-69.

Bulone, D., D. Giacomazza, V. Martorana, J. Newman and P. L. San Biagio (2004). "Ordering of agarose near the macroscopic gelation point." Physical Review E **69**(4): 041401.

Buyong, N. and O. Fennema (1988). "Amount and Size of Ice Crystals in Frozen Samples as Influenced by Hydrocolloids." Journal of Dairy Science **71**(10): 2630-2639.

Carvalho, W. and M. Djabourov (1997). "Physical gelation under shear for gelatin gels." Rheologica Acta **36**(6): 591-609.

Cahn, J. W. (1961). "On spinodal decomposition." Acta Metallurgica **9**(9): 795-801.

Chan, C. K., F. Perrot and D. Beysens (1988). "Effects of Hydrodynamics on Growth: Spinodal Decomposition under Uniform Shear Flow." Physical Review Letters **61**(4): 412.

Chen, Y., Z. Hu and J. C. Lang (1998). "Turbidity investigation of the sol–gel transition in carrageenan gels under physiologic conditions." Journal of Applied Polymer Science **68**(1): 29-35.

Chiti, F. (2007). Lagrangian studies of turbulent mixing in a vessel agitated by a rushton turbine: Positron emission particle tracking (PEPT) and computational fluid dynamics (CFD). Department of Chemical Engineering. Birminngham, Birmingham**:** 229.

Cox, P. W., S. Bakalis, H. Ismail, R. Forster, D. J. Parker and P. J. Fryer (2003). "Visualisation of three-dimensional flows in rotating cans using positron emission particle tracking (PEPT)." Journal of Food Engineering **60**(3): 229-240.

de Vicente, J., J. R. Stokes and H. A. Spikes (2005). "The Frictional Properties of Newtonian Fluids in Rolling–Sliding soft-EHL Contact." Tribology Letters **20**(3): 273-286.

de Vicente, J., J. R. Stokes and H. A. Spikes (2005). "Lubrication properties of non-adsorbing polymer solutions in soft elastohydrodynamic (EHD) contacts." Tribology International **38**(5): 515-526.

de Vicente, J., J. R. Stokes and H. A. Spikes (2006). "Soft lubrication of model hydrocolloids." Food Hydrocolloids **20**(4): 483-491.

de Wijk, R. A. and J. F. Prinz (2005). "The role of friction in perceived oral texture." Food Quality and Preference **16**(2): 121-129.

Dea, I. C. M., A. Morrison, R. S. Tipson and H. Derek (1975). Chemistry and Interactions of Seed Galactomannans. Advances in Carbohydrate Chemistry and Biochemistry, Academic Press. **Volume 31:** 241-312.

Depypere, F., J. G. Pieters and K. Dewettinck (2009). "PEPT visualisation of particle motion in a tapered fluidised bed coater." Journal of Food Engineering **93**(3): 324-336.

Dickinson, E. (1989). "Food colloids -- An overview." Colloids and Surfaces **42**(1): 191-204.

Dorsey, N. E. (1968). Properties of ordinary water-substance, in all its phases: water-vapor, water and all the ices. New York.

Dowson, D. and G. R. Higginson (1959). "A numerical solution to the elastohydrodynamic problem." Journal of Mechanical Engineering Science **1**(1): 6-15.

Dresselhuis, D. M., E. H. A. de Hoog, M. A. Cohen Stuart and G. A. van Aken (2008). "Application of oral tissue in tribological measurements in an emulsion perception context." Food Hydrocolloids **22**(2): 323-335.

Ellis, A. and J. C. Jacquier (2009). "Manufacture and characterisation of agarose microparticles." Journal of Food Engineering **90**(2): 141-145.

Elmore, J. R., H. Heymann, J. Johnson and J. E. Hewett (1999). "Preference mapping: relating acceptance of "creaminess" to a descriptive sensory map of a semi-solid." Food Quality and Preference **10**(6): 465-475.

Emanuele, A., L. Di Stefano, D. Giacomazza, M. Trapanese, M. B. Palma-Vittorelli and M. U. Palma (1991). "Time-Resolved study of network self-organization from a biopolymeric solution." Biopolymers **31**(7): 859-868.

Engelen, L., M. Schipper and F. Bosman (2005). "Oral size Perception of particles: Effect of size, type, viscosity and method." Journal of Texture Studies **36**(4): 373-386.

Esfahanian, M. and B. J. Hamrock (1991). "Fluid-Film Lubrication Regimes Revisited." Tribology Transactions **34**(4): 628 - 632.

Fairhurst, P. G., M. Barigou, P. J. Fryer, J. P. Pain and D. J. Parker (2001). "Using positron emission particle tracking (PEPT) to study nearly neutrally buoyant particles in high solid fraction pipe flow." International Journal of Multiphase Flow **27**(11): 1881-1901.

Falshaw, R., R. H. Furneaux and D. E. Stevenson (1998). "Agars from nine species of red seaweed in the genus Curdiea (Gracilariaceae, Rhodophyta)." Carbohydrate Research **308**(1-2): 107-115.

Fangary, Y. S., M. Barigou, J. P. K. Seville and D. J. Parker (2000). "Fluid trajectories in a stirred vessel of non-newtonian liquid using positron emission particle tracking." Chemical Engineering Science **55**(24): 5969-5979.

Feke, G. T. and W. Prins (1974). "Spinodal Phase Separation in a Macromolecular Sol ‚Üí Gel Transition." Macromolecules **7**(4): 527-530.

Ferry, A.-L. S., J. R. Mitchell, J. Hort, S. E. Hill, A. J. Taylor, S. Lagarrigue and B. Vall√®s-P√†mies (2006). "In-Mouth Amylase Activity Can Reduce Perception of Saltiness in Starch-Thickened Foods." Journal of Agricultural and Food Chemistry **54**(23): 8869-8873.

Ferry, A. L., J. Hort, J. R. Mitchell, D. J. Cook, S. Lagarrigue and B. Valles Pamies (2006). "Viscosity and flavour perception: Why is starch different from hydrocolloids?" Food Hydrocolloids **20**(6): 855-862.

Frith, W. J., X. Garijo, T. J. Foster and I. T. Norton (2002). Microstructural origins of the rheology of fluid gels. Gums and stabilisers for the food industry, The Royal Society od Chemisty. **11:** 95 - 103.

Gabriele, A., A. W. Nienow and M. J. H. Simmons (2009). "Use of angle resolved PIV to estimate local specific energy dissipation rates for up- and down-pumping pitched blade agitators in a stirred tank." Chemical Engineering Science **64**(1): 126-143.

Gabriele, A., F. Spyropoulos and I. T. Norton (2009). "Kinetic study of fluid gel formation and viscoelastic response with kappa-carrageenan." Food Hydrocolloids **23**(8): 2054-2061.

Gabriele, A., F. Spyropoulos and I. T. Norton (2009). Rheology of microstructures based on spinodally decomposed polysaccharides fluid gels. 5th International Symposium on Food Rheology and Structure, Zurich.

Gibbs, J. W. (1957). Collected Works. New Haven, Conneticut, Yale University Press.

Gohar, R. (2001). Elastohydrodynamics. London, Imperial College Press.

Guest, S. and C. Spence (2003). "What role does multisensory integration play in the visuotactile perception of texture?" International Journal of Psychophysiology **50**(1-2): 63-80.

Guida, A., X. Fan, D. J. Parker, A. W. Nienow and M. Barigou (2009). "Positron emission particle tracking in a mechanically agitated solid-liquid suspension of coarse particles." Chemical Engineering Research and Design **87**(4): 421-429.

Guida, A., A. W. Nienow and M. Barigou "PEPT measurements of solid-liquid flow field and spatial phase distribution in concentrated monodisperse stirred suspensions." Chemical Engineering Science **In Press, Corrected Proof**.

Guinard, J.-X. and R. Mazzucchelli (1996). "The sensory perception of texture and mouthfeel." Trends in Food Science & Technology **7**(7): 213-219.

Guo, F., Z. Fu, P. L. Wong and P. Yang (2008). "Experimental study on lubrication regime variation in point contacts." Tribology International **41**(6): 451-460.

Halling, J. (1975). Principles of Tribology. Prescot, Tinling Ltd.

Hamrock, B. J. (1994). Fundamentals of fluid film lubrication. New York, Mc Graw Hill.

Hamrock, B. J. and D. Dowson (1978). "Elastohydrodynamic lubrication of elliptical contacts for material of low elastic modulus, Part 1 - Fully flooded conjunction." Jour. Lubr. Tech. **100**(2): 236 - 245.

Hanselmann, W. and E. Windhab (1998). "Flow characteristics and modelling of foam generation in a continuous rotor/stator mixer." Journal of Food Engineering **38**(4): 393-405.

Harden, A. and W. J. Young (1913). "The Enzymatic Formation of Polysaccharides by Yeast Preparations." Biochem J. **7**(6): 630 - 636.

Hawkesworth, M. R., M. A. O'Dwyer, J. Walker, P. Fowles, J. Heritage, P. A. E. Stewart, R. C. Witcomb, J. E. Bateman, J. F. Connolly and R. Stephenson (1986). "A positron camera for industrial application." Nuclear Instruments and Methods in Physics Research Section A: Accelerators, Spectrometers, Detectors and Associated Equipment **253**(1): 145-157.

Hertz, H. (1826). "Über die Berührung fester elastischer Körper." Journal für die reine und angewandte Mathematik **92**: 156-171.

Hill, E. (2007). How green is your cream? Financial Times, The Financial Times Ltd.

Hutchings, J. B. and P. J. Lillford (1988). "THE PERCEPTION OF FOOD TEXTURE - THE PHILOSOPHY OF THE BREAKDOWN PATH." Journal of Texture Studies **19**(2): 103-115.

Ilievski, D., M. Rudman and G. Metcalfe (2001). "The separate roles of shear rate and mixing on gibbsite precipitation." Chemical Engineering Science **56**(7): 2521-2530.

Imai, E., K. Hatae and A. Shimada (1995). "Oral Perception of Grittiness: Effect of Particle Size and Concentration of the Dispersed Particles and the Dispersion Medium." Journal of Texture Studies **26**(5): 561-576.

Imai, E., Y. Shimichi, I. Maruyama, A. Inoue, S. Ogawa, K. Hatae and A. Shimada (1997). "Perception of grittiness in an oil-in-water emulsion." Journal of Texture Studies **28**(3): 257-272.

Imeson, A. (2000). Carrageenan. Handbook of Hydrocolloids. G. O. Phillips and P. A. Williams, Woodhead Publishing**:** 87 - 103.

Johnson, K. L. (1970). "Regimes of elastohydrodynamic lubrication." Journal of Mechanical Engineering Science **12**(1): 9-16.

Kandel, E. R. (1991). From Nerve Cells to Cognition: The Internal Cellular Representation Required for Perception and Action. Principles of Neural Science. E. R. K., J. H. S. and T. M. Jessell. New York, McGraw-Hill**:** 382 - 403.

Kara, S., E. Arda and Ö. Pekcan (2007). "Monovalent and Divalent Cation Effects on Phase Transitions of i-carrageenan." Journal of Bioactive and Compatible Polymers **22**(1): 42-61.

Kilcast, D. and S. Clegg "Sensory perception of creaminess and its relationship with food structure." Food Quality and Preference **13**(7-8): 609-623.

Kroezen, A. B. J., J. Groot Wassink and E. Bertlein "Foam generation in a rotor--stator mixer : schaumerzeugung in einem rotor--stator mischer." Chemical Engineering and Processing **24**(3): 145-156.

Larachi, F., B. P. A. Grandjean and J. Chaouki (2003). "Mixing and circulation of solids in spouted beds: particle tracking and Monte Carlo emulation of the gross flow pattern." Chemical Engineering Science **58**(8): 1497-1507.

Ledward, D. A. (2000). Gelatin. Handbook of Hydrocolloids. G. O. Phillips and P. A. Williams, Woodhead Publishing**:** 41 - 66.

Leone, M., F. Sciortino, M. Migliore, S. L. Fornili and M. B. P. Vittorelli (1987). "Order parameters of gels and gelation kinetics of aqueous agarose systems: Relation to the spinodal decomposition of the sol." Biopolymers **26**(5): 743-761.

Lund, B., A. C. B. Parker and G. W. Gould (1999). The microbiological safety and quality of foods, Aspen Publishers Inc.

Malone, M. E., I. A. M. Appelqvist and I. T. Norton (2003). "Oral behaviour of food hydrocolloids and emulsions. Part 1. Lubrication and deposition considerations." Food Hydrocolloids **17**(6): 763-773.

Malone, M. E., I. A. M. Appelqvist and I. T. Norton (2003). "Oral behaviour of food hydrocolloids and emulsions. Part 2. Taste and aroma release." Food Hydrocolloids **17**(6): 775-784.

Manning, G. S. (1969). "Limiting Laws and Counerion Condensation in Polyelectrolyte Solutions." J. Chem. Phys. **51**: 924-933.

Marinho-Soriano, E. and E. Bourret (2005). "Polysaccharides from the red seaweed Gracilaria dura (Gracilariales, Rhodophyta)." Bioresource Technology **96**(3): 379-382.

Mason, T. G., J. Bibette and D. A. Weitz (1996). "Yielding and Flow of Monodisperse Emulsions." Journal of Colloid and Interface Science **179**(2): 439-448.

Meeker, S. P., R. T. Bonnecaze and M. Cloitre (2004). "Slip and Flow in Soft Particle Pastes." Physical Review Letters **92**(19): 198302-4.

Mela, D. J. (1988). "Sensory assessment of fat content in fluid dairy products." Appetite **10**(1): 37-44.

Metzner, A. B. and R. E. Otto (1957). "Agitation of non-Newtonian fluids." AIChE Journal **3**(1): 3-10.

Mohammed, Z. H., M. W. N. Hember, R. K. Richardson and E. R. Morris (1998). "Kinetic and equilibrium processes in the formation and melting of agarose gels." Carbohydrate Polymers **36**(1): 15-26.

Morris, E. R. (1993). Rheological and organoleptic properties of food hydrocolloids. Food hydrocolloids: structures, properties, and functions. N. Katsuyoshi and D. Etsushiro. New York, Plenum Press**:** 201 - 210.

Morris, E. R. and D. A. Rees (1978). "Principles of Biopolymer Gelation." British Medical Bulletin **34**(1): 49 - 53.

Morris, E. R., D. A. Rees, I. T. Norton and D. M. Goodall (1980). "Calorimetric and chiroptical evidence of aggregate-driven helix formation in carrageenan systems." Carbohydrate Research **80**(2): 317-323.

Morris, E. R., D. A. Rees and G. Robinson (1980). "Cation-specific aggregation of carrageenan helices: Domain model of polymer gel structure." Journal of Molecular Biology **138**(2): 349-362.

Morris, E. R., R. K. Richardson and L. J. Taylor (1984). "Correlation of the perceived texture of random coil polysaccharide solutions with objective parameters." Carbohydrate Polymers **4**(3): 175-191.

Morris, V. J. (1998). Gelation of polysaccharides. Functional Properties of Food Macromolecules. S. E. Hill, D. A. Ledward and J. R. Mitchell, Aspen Publishers.

Narine, S. S. and A. G. Marangoni (1999). "Fractal nature of fat crystal networks." Physical Review E **59**(2): 1908.

Normand, V., D. L. Lootens, E. Amici, K. P. Plucknett and P. Aymard (2000). "New Insight into Agarose Gel Mechanical Properties." Biomacromolecules **1**(4): 730-738.

Norton, I. T., T. J. Foster and C. R. T. Brown (1998). The science and technology of fluid gels. Gums and Stabilisers for the Food Industry. P. A. Williams and G. O. Phillips. Cambridge, UK, RSC. **9:** 259-268.

Norton, I. T. and W. J. Frith (2001). "Microstructure design in mixed biopolymer composites." Food Hydrocolloids **15**(4-6): 543-553.

Norton, I. T., W. J. Frith and S. Ablett (2006). "Fluid gels, mixed fluid gels and satiety." Food Hydrocolloids **20**(2-3): 229-239.

Norton, I. T., D. M. Goodall, K. R. J. Austen, E. R. Morris and D. A. Rees (1986). "Dynamics of molecular organization in agarose sulphate." Biopolymers **25**(6): 1009-1029.

Norton, I. T., D. M. Goodall, E. R. Morris and D. A. Rees (1979). "Kinetic evidence consistent with double helix formation in K-carrageenan solutions." J. Chem. Soc., Chem. Commun.: 988 - 990.

Norton, I. T., D. M. Goodall, E. R. Morris and D. A. Rees (1983). "Role of Cations in the Conformation of Iota and Kappa Carrageenan." J. Chem. Soc.Faraday Trans. I **79**: 2475 - 2488.

Norton, I. T., D. A. Jarvis and T. J. Foster (1999). "A molecular model for the formation and properties of fluid gels." International Journal of Biological Macromolecules **26**(4): 255-261.

Norton, I. T., C. G. Smith, W. J. Frith and F. T.J. (2000). The production, properties and utilisation of fluid gels. Hydrocolloids. G. O. Phillips and P. A. Williams. **2:** 217 – 227.

Onuki, A. (1987). "Viscosity enhancement by domains in phase-separating fluids near the critical point: Proposal of critical rheology." Physical Review A **35**(12): 5149.

Paoletti, S., O. Smidsrød and H. Grasdalen (1984). "Thermodynamic stability of the ordered conformations of carrageenan polyelectrolytes." Biopolymers **23**(9): 1771-1794.

Parker, D. J., C. J. Broadbent, P. Fowles, M. R. Hawkesworth and P. McNeil (1993). "Positron emission particle tracking - a technique for studying flow within engineering equipment." Nuclear Instruments and Methods in Physics Research Section A: Accelerators, Spectrometers, Detectors and Associated Equipment **326**(3): 592-607.

Parker, D. J., R. N. Forster, P. Fowles and P. S. Takhar (2002). "Positron emission particle tracking using the new Birmingham positron camera." Nuclear Instruments and Methods in Physics Research Section A: Accelerators, Spectrometers, Detectors and Associated Equipment **477**(1-3): 540-545.

Paul, E. L., V. A. Atiemo-Obeng and S. M. Kresta (2003). Handbook of Industrial Mixing - Science and Practice.

Penfield, W. and T. Rasmussen (1950). The celebral cortex of man. New York, Macmillian.

Prinz, J. F. and P. W. Lucas (2000). "Saliva tannin interactions." Journal of Oral Rehabilitation **27**(11): 991 - 994.

Rees, D. A. (1963). "The carrageenan system of polysaccharides. Part I. The relation between the - and -components." J. Chem. Soc.(32): 1821 - 1832.

Rees, D. A. (1969). "Structure, conformation and mechanism in the formation of polysaccharide gels and networks." Adv. Carbohydr. Chem. **24**: 267 – 332.

Richardson, N. J., D. A. Booth and N. L. Stanley (1993). "Effect of homogenization and fat content on oral perception of low and high viscosity model creams." Journal of Sensory Studies **8**(2): 133-143.

Richardson, R. K., E. R. Morris, S. B. Ross-Murphy, L. J. Taylor and I. C. M. Dea (1989). "Characterization of the perceived texture of thickened systems by dynamic viscosity measurements." Food Hydrocolloids **3**(3): 175-191.

Rochas, C. and M. Rinaudo (1980). "Activity coefficients of counterions and conformation in kappa-carrageenan systems." Biopolymers **19**(9): 1675-1687.

San Biagio, P. L., D. Bulone, A. Emanuele, M. B. Palma-Vittorelli and M. U. Palma (1996). "Spontaneous symmetry-breaking pathways: time-resolved study of agarose gelation." Food Hydrocolloids **10**(1): 91-97.

San Biagio, P. L., F. Madonia, J. Newman and M. U. Palma (1986). "Sol-sol structural transition of aqueous agarose systems." Biopolymers **25**(12): 2255-2269.

Shama, F. and P. Sherman (1973). "Identification of stimuly controlling the sensory evaluation of viscosity II. Oral Methods." Journal of Texture Studies **4**(1): 111-118.

Sinnott, R. (2005). Coulson & Richardson's Chemical Engineering, Oxford Oxfordshire: Oxford University Press.

Smewing, J. (1999). Hydrocolloids. Food Texture - Measurement and Perception. A. J. Rosenthal. Gaithrsburg, Aspen Publishers.

Smidsrød, O., I.-l. Andresen, H. Grasdalen, B. Larsen and T. Painter (1980). "Evidence for a salt-promoted "freeze-out" of linkage conformations in carrageenans as a prerequisite for gel-formation." Carbohydrate Research **80**(1): C11-C16.

Speetjens, M., M. Rudman and G. Metcalfe (2006). "Flow regime analysis of non-Newtonian duct flows." Physics of Fluids **18**(1): 13101-13114.

Szczesniak, A. S. (1963). "Classification of Textural Characteristicsa." Journal of Food Science **28**(4): 385-389.

Tako, M. and S. Nakamura (1988). "Gelation mechanism of agarose." Carbohydrate Research **180**(2): 277-284.

Thomas, W. R. (1997). Gel Texture of Carrageenan. Thickening and Gelling Agents for Food. A. Imeson. New York, Aspen Publishers.

Tuvikene, R., K. Truus, A. Kollist, O. Volobujeva, E. Mellikov and T. Pehk (2008). "Gel-forming structures and stages of red algal galactans of different sulfation levels." Journal of applied phycology **20**: 9.

Tyle, P. (1993). "Effect of Size, Shape and Hardness of Particles in Suspension on Oral Texture and Palatability." Acta Psychologica **84**(1): 111-118.

Wilkinson, C., G. B. Dijksterhuis and M. Minekus (2000). "From food structure to texture." Trends in Food Science & Technology **11**(12): 442-450.

Wittmer, S., L. Falk, P. Pitiot and H. Vivier (1998). "Characterization of stirred vessel hydrodynamics by three dimensional trajectography." The Canadian Journal of Chemical Engineering **76**(3): 600-610.

Wolf, B., R. Scirocco, W. J. Frith and I. T. Norton (2000). "Shear-induced anisotropic microstructure in phase-separated biopolymer mixtures." Food Hydrocolloids **14**(3): 217-225.

Wu, H. and G. K. Patterson (1989). "Laser-Doppler measurements of turbulent-flow parameters in a stirred mixer." Chemical Engineering Science **44**(10): 2207-2221.

Yakubov, G. E., J. McColl, J. H. H. Bongaerts and J. J. Ramsden (2009). "Viscous Boundary Lubrication of Hydrophobic Surfaces by Mucin." Langmuir **25**(4): 2313-2321.

Yataghene, M., J. Pruvost, F. Fayolle and J. Legrand (2008). "CFD analysis of the flow pattern and local shear rate in a scraped surface heat exchanger." Chemical Engineering and Processing: Process Intensification **47**(9-10): 1550-1561.

Yuguchi, Y., T. T. Thu Thuy, H. Urakawa and K. Kajiwara (2002). "Structural characteristics of carrageenan gels: temperature and concentration dependence." Food Hydrocolloids **16**(6): 515-522.

APPENDIX I.

MATLAB® Scripts

AI.1 PEPT.m

```
clc; clear; warning off; %#ok<WNOFF>
M=[];Utip=900/60*pi*(35.56/1000);
%% Available File in the Folder
File=dir('andrea.a*');

%% Loader and Preliminary plot
F=input('select_working file [1-16 list] or specify array [ a ]: ','s');
if strcmp(F, 'list')== 1
    for i=1:size(File,1)
        fid = fopen(File(i).name, 'r');
        FileF_line= fgetl(fid);
        disp(['[',num2str(i),']',' ',FileF_line]);
    end
    i=input('file number: ');
    A=Pload(File(i).name,'n');
elseif strcmp(F, 'a')== 1
    for i=1:size(File,1)
        fid = fopen(File(i).name, 'r');
        FileF_line= fgetl(fid);
        disp(['[',num2str(i),']',' ',FileF_line]);
    end
    Array_Vect=input('define array of files belonging to subsequent runs
[1,3,... ]:  ');
    home
    [M]=ArrayCreator(Array_Vect);
else
    fid = fopen(File(str2double(F)).name, 'r');
    FileF_line= fgetl(fid);
    A=Pload(File(str2double(F)).name,'n');
end

for i=1:length(MM)
    MM(i).ACc=zeros(size(MM(i).A));
    MM(i).AP=zeros(size(MM(i).A));
    MM(i).V=zeros(size(MM(i).A));
end

for i=1:length(MM)

    [MM(i).ACc
zz]=DigitalClean(MM(i).A(:,1),MM(i).A(:,2),MM(i).A(:,4),MM(i).A(:,3),'no');

    MM(i).AP(:,1)=MM(i).ACc(:,1);
    [MM(i).AP(:,2) MM(i).AP(:,3)
MM(i).AP(:,4)]=cart2pol(MM(i).ACc(:,2),MM(i).ACc(:,3),MM(i).ACc(:,4));
    th=MM(i).AP(:,2);
    th1=zeros(length(th),1);
    th1(1)=th(1);
    tmp=0;
    th=th';
    for k=2:length(th)
        if(th(k)-th(k-1))<-pi
            tmp=tmp+2*pi;
```

```
        elseif (th(k)-th(k-1))>pi
            tmp=tmp-2*pi;
        end
        th1(k)=th(k)+tmp;
    end
    clear tmp;%plot(th1)
    MM(i).AP(:,2)=th1*-1; clear th1
    n=input('Number of points over which interpolate');
    m=input('Order of the polynomial');

    %% Polar

    [Velth_Rad]=InterpPEPT3(MM(i).A(:,1),MM(i).AP(:,2),n,m);
    [velz]=InterpPEPT3(MM(i).A(:,1),MM(i).AP(:,4),n,m);
    [velr]=InterpPEPT3(MM(i).A(:,1),MM(i).AP(:,3),n,m);

    veltheta=((Velth_Rad).*MM(i).AP(:,3));

    MM(i).V(:,1)=veltheta;
    MM(i).V(:,2)=velr;
    MM(i).V(:,3)=velz;
    MM(i).V(:,4)=(veltheta.^2+velr.^2+velz.^2).^(0.5);

end
clear n th velr veltheta velz zz i k ans Velth_Rad


Time=[];Theta=[];Radius=[];Zeta=[];VEL_TH=[];VEL_Z=[];VEL_R=[];VEL=[];
for i=1:length(MM)
    Time=   [Time; MM(i).AP(:,1)];
    Theta=  [Theta; MM(i).AP(:,2)];
    Radius= [Radius; MM(i).AP(:,3)];
    Zeta=    [Zeta; MM(i).AP(:,4)];
    VEL_TH=[VEL_TH; MM(i).V(:,1)];
    VEL_R=[VEL_R; MM(i).V(:,2)];
    VEL_Z=[VEL_Z; MM(i).V(:,3)];
    VEL=[VEL; MM(i).V(:,4)];
end

Theta(find(Theta<0))=Theta(find(Theta<0))*-1;

tic
[E_z Cond_if]=eulo(Time,Theta,Zeta,Radius,VEL_TH,VEL_Z,VEL_R,VEL);
toc

[Gammaf]=shear_calc(E);
```

AI.2. Pload.m

```
function DATA=Pload(File,s)

fid = fopen(File, 'r');
FileN_1= fgetl(fid);
FileName = [FileN_1,'.txt'];
preview=dlmread(File,' ',15,0);
```

```
ss=textscan(fid,'%s %s %s %s %s %s %s %s
',size(preview,1)+15,'MultipleDelimsAsOne',1);
fclose(fid); clear preview fid
a=cell2struct(ss(1:5),'Data',4);
DATA=zeros(length(5:length(a(1,1).Data)),1);

for v=1:5
    D=str2double(a(1,v).Data(5:length(a(1,v).Data)));
    DATA(:,v)=D(:,1);
end

if s == 'y'

%% check for Irregualar characters
F=textscan(FileName, '%1s');
for n=1:length(F 1,1 })
    tmp=char(F 1}(n));
    if tmp == '/'
        F 1}(n)= '_'};
        disp('Irregular Character Found "/"')
        disp('Substituted with "_"')
    else
    end
end
FileName=char(F 1}(1:length(F[1,1})));
intestazione=('Time [s], x [mm], y [mm], z [mm]');
warning off


tmp_OW=dir(FileName);
if size(tmp_OW,1) == 0;

    dlmwrite(FileName,intestazione, 'delimiter', '','precision','%.7f',
'newline', 'pc','-append', 'newline', 'pc')
    dlmwrite(FileName,DATA, 'delimiter', ',','precision','%.7f', 'newline',
'pc','-append', 'newline', 'pc')
    display(['File Saved: ', FileName' ])

else
    Quest=['File "' num2str(FileName') '" already present. Overwrite,
Rename, Cancel [o, r, c]: '];
    tmp_2=input(Quest,'s');
    if tmp_2== 'o'
        delete(FileName)
        dlmwrite(FileName,intestazione, 'delimiter', '','precision','%.7f',
'newline', 'pc','-append', 'newline', 'pc')
        dlmwrite(FileName,DATA, 'delimiter', ',','precision','%.7f',
'newline', 'pc','-append', 'newline', 'pc')
        display(['File Saved: ', FileName' ])

    elseif tmp_2== 'r'
        NFileName=[FileN_1,'_', date,'.txt'];
        tmp_OW_2=dir(NFileName); j=0;
        while size(tmp_OW_2,1) == 1;
            tmp_OW_2=dir(NFileName); j=j+1; NFileName=[FileN_1,'_', date,
'_' ,num2str(j), '.txt'];
        end
        dlmwrite(NFileName,intestazione, 'delimiter',
'','precision','%.7f', 'newline', 'pc','-append', 'newline', 'pc')
```

```
        dlmwrite(NFileName,DATA, 'delimiter', ',','precision','%.7f',
'newline', 'pc','-append', 'newline', 'pc')
        display(['File Saved: ', NFileName ])
    else
    end
end

else
end
```

AI.3. ArrayCreator.m

```
function [M]=ArrayCreator(Array_Vect)
global File
%% this function joins into a single experiment, data divaded over multiple
runs
%1 loads selected file names
%2 centers each file with the standard deviation of the bimodal curve

%% Select files to Load files
k=0;
for g=1:length(Array_Vect)
    G=k+g;
    %load part
        fid = fopen(File(Array_Vect(1,g)).name, 'r');
        FileF_line= fgetl(fid);
        home
        disp(['Loading ',FileF_line,'...']);

    A=Pload(File(Array_Vect(g)).name,'n');

    n=input('How Many Runs/Parts are present? ');
    if n>=2
        for j=G:G+n-1
            B=ManClean(A);
            eval(['M.A',num2str(j),'=Auto_Clean(B);']);
%             eval(['M.A',num2str(g),'_part_',num2str(j),'=A;'])
            k=G; clear B
        end
    else
        A=Auto_Clean(A);
        eval(['M.','A',num2str(G),'=A;'])
    end

end
```

AI.4. ManClean.m

```
function A=ManClean(M)

tmp=input('Location coordinates to plot? [x r theta]: ','s');
```

```
if tmp=='x'
    fig=figure; plot(M(:,2));
elseif tmp=='r'
    fig=figure; plot(M(:,3));
else tmp =~ 'x' | 'r';
    fig=figure; plot(M(:,4));
end

dcm_obj = datacursormode(fig);
set(dcm_obj,'DisplayStyle','datatip',...
    'SnapToDataVertex','off','Enable','on')
hold on
pause
% plot(A(:,4));
cursor_info_start = getCursorInfo(dcm_obj);
dcm_obj = datacursormode(fig);
set(dcm_obj,'DisplayStyle','datatip',...
    'SnapToDataVertex','off','Enable','on');
figure(fig)
pause
cursor_info_end =  getCursorInfo(dcm_obj);
close

tmp_A=M(cursor_info_start.DataIndex:cursor_info_end.DataIndex,1);
tmp_A=[tmp_A M(cursor_info_start.DataIndex:cursor_info_end.DataIndex,2)];
tmp_A=[tmp_A M(cursor_info_start.DataIndex:cursor_info_end.DataIndex,3)];
tmp_A=[tmp_A M(cursor_info_start.DataIndex:cursor_info_end.DataIndex,4)];


A=tmp_A;
```

AI.5. Auto_Clean.m

```
function A_Auto_Clean=Auto_Clean(A)
global File

File=dir('andrea01.a*');

for i=1:size(File,1)
        fid = fopen(File(i).name, 'r');
        FileF_line= fgetl(fid);
        disp(['[',num2str(i),']',' ',FileF_line]);
end

i=input('file number relative to Input Location: ');
LocIn=mean(Pload(File(i).name,'n'),1);
i=input('file number relative to Output Location: ');
LocOut=mean(Pload(File(i).name,'n'),1);
%Automatic Cleaning using Locations
% Finds the closest location of the data (matrix A) to the inlet
% cohordinates LocIn
        IndxIn = find(abs(A(:,2)-LocIn(1,2))+abs(A(:,3)-
LocIn(1,3))+abs(A(:,4)-LocIn(1,4))...
            == min(abs(A(:,2)-LocIn(1,2))+abs(A(:,3)-
LocIn(1,3))+abs(A(:,4)-LocIn(1,4))));
 %Same as above but for Outlet
```

```
        IndxOut = find(abs(A(:,2)-LocOut(1,2))+abs(A(:,3)-
LocOut(1,3))+abs(A(:,4)-LocOut(1,4))...
            == min(abs(A(:,2)-LocOut(1,2))+abs(A(:,3)-
LocOut(1,3))+abs(A(:,4)-LocOut(1,4))));
% figure;hold
on,plot3(A(IndxOut,2),A(IndxOut,3),A(IndxOut,4),'rp');plot3(A(:,2),A(:,3),A
(:,4),'wo');plot3(A(IndxIn,2),A(IndxIn,3),A(IndxIn,4),'rp');
 fclose all;
A_Auto_Clean=A(IndxIn:IndxOut,:);
```

AI.6. DigitalClean.m

```
function [A1C Circ]=DigitalClean(A,tmp)



% Rough Cleaning of the extremes
% plot(A1(floor(0.4*length(A1)):floor(0.70*length(A1)),2))
A1=A(floor(0.4*length(A)):floor(0.70*length(A)),:);
% for i=1:20

[X
Z]=meshgrid(min(A1(:,2)):0.15:max(A1(:,2)),min(A1(:,4)):0.15:max(A1(:,4)));
 Mask=ones(size(X,1),size(X,2));

for i=1:length(A1)
 Mask(find((abs(Z(:,1)-A1(i,4))) == min(abs(Z(:,1)-
A1(i,4)))),find((abs(X(1,:)-A1(i,2))) == min(abs(X(1,:)-A1(i,2)))))=0;
end
Mask = imfill(-1*(Mask-1),'holes');


xm=min(X(find(X==(X.*Mask))));
xM=max(X(find(X==(X.*Mask))));
zm=min(Z(find(Z==(Z.*Mask))));
zM=max(Z(find(Z==(Z.*Mask))));

xMean=(xM+xm)/2;
zMean=(zM+zm)/2;

%Applying centering parameters
A1C(:,1)=A(:,1)-min(A(:,1));
A1C(:,2)=A(:,2)-xMean;
A1C(:,3)=A(:,3)-240;
A1C(:,4)=A(:,4)-zMean;

% maximum radius

[Xo
Zo]=meshgrid(min(A1C(:,2)):0.5:max(A1C(:,2)),min(A1C(:,4)):0.5:max(A1C(:,4)
));
R=max(max((((X-xMean).*Mask).^2+((Z-zMean).*Mask).^2).^0.5)));

% Create circular mask for probable autocorrelation
%creates the parametric circumference
```

```
k=1;xo=0;yo=0;clear x y z
for th=0:0.01:2*pi
    x(k)=R*cos(th)+xo;
    y(k)=R*sin(th)+yo;
    z(k,:)=0:38:152;
    k=k+1;
end

if strcmp(tmp,'yes')
    plot3(x,y,z,'r'); hold;
plot3(A1C(1:10:40000,2),A1C(1:10:40000,4),A1C(1:10:40000,3),'b');
    axis equal

else
end

Circ=[x; y; z'];

end
```

AI.7. Interp3PEPT.m

```
function [A R]=Interp3PEPT(X,Y,n,m)
%% Polynomial Interpolation to give velocities
clear tmp


if n==3
    n=1;
elseif n==5
    n=2;
elseif n>=7
    n=3;
end


switch  m

    case 1

        A=zeros(size(X));
        R=zeros(size(X));

        for i=n+1:length(X)-n
            x=X(i-n:i+n);
            y=Y(i-n:i+n);

            Xx=[ones(length(x),1), x(:,1)];

            B=pinv(Xx)*y;
            B=flipdim(B,1);
            dB=polyder(B);
            A(i)=polyval(dB',x(n+1));

            yfit=polyval(B,x);
            TSS = sum((y-mean(y)).^2);
```

```
            RSS = sum((y-yfit).^2);
            R(i) = 1 - RSS/TSS;

        end

    case 2

        A=zeros(size(X));
        R=zeros(size(X));

        for i=n+1:length(X)-n

            x=X(i-n:i+n);
            y=Y(i-n:i+n);

            Xx=[ones(length(x),1), x(:,1), x(:,1).^2];

            B=pinv(Xx)*y;
            B=flipdim(B,1);
            dB=polyder(B);
            A(i)=polyval(dB',x(n+1));

            yfit=polyval(B,x);
            TSS = sum((y-mean(y)).^2);
            RSS = sum((y-yfit).^2);
            R(i) = 1 - RSS/TSS;

        end

    case 3
        A=zeros(size(X));
        R=zeros(size(X));
        for i=n+1:length(X)-n

            x=X(i-n:i+n);
            y=Y(i-n:i+n);

            Xx=[ones(length(x),1), x(:,1), x(:,1).^2, x(:,1).^3];

            B=pinv(Xx)*y;
            B=flipdim(B,1);
            dB=polyder(B);
            A(i)=polyval(dB',x(n+1));

            yfit=polyval(B,x);
            TSS = sum((y-mean(y)).^2);
            RSS = sum((y-yfit).^2);
            R(i) = 1 - RSS/TSS;

        end

end
```

AI.8. eulo.m

```
function [eul,Cond_if]=eulo(TT,TH,Z,R,VTH,VZ,VR,VV)

clc;
MaxR=30;
MaxZ=150;
R((R(:,1)>MaxR),:)=0;
Z((Z(:,1)>MaxZ),:)=0;

r_bins=80;
r_nodes=sqrt((0:r_bins)/r_bins)*MaxR;
r_centers=(r_nodes(1:length(r_nodes)-1)+...
    r_nodes(2:length(r_nodes)))/2;

th_bins=48;
th_nodes=0:2*pi/th_bins:max(TH);
th_centers=(th_nodes(1:length(th_nodes)-1)+th_nodes(2:length(th_nodes)))/2;
M_th_center=length(th_centers);

th_nodes_1=linspace(0,2*pi,th_bins+1);
th_centers_1=(th_nodes_1(1:length(th_nodes_1)-
1)+th_nodes_1(2:length(th_nodes_1)))/2;


z_bins=250;
z_nodes=linspace(0,1,z_bins+1)*MaxZ;
z_centers=(z_nodes(1:length(z_nodes)-1)+...
    z_nodes(2:length(z_nodes)))/2;

Length_TH=length(TH);

eul=zeros(th_bins,z_bins,r_bins,9); Cond_if=zeros(Length_TH,1);

z=[];r=[];th=[];
for i=1:r_bins
    z=[z; z_centers]; %#ok<AGROW>
end
for i=1:z_bins
    r=[r r_centers']; %#ok<AGROW>
end
for i=1:z_bins
    th=[th; th_centers_1]; %#ok<AGROW>
end
for i=1:r_bins
    eul(:,:,i,1)=th';
end
for i=1:th_bins
    eul(i,:,:,2)=z';
end
for i=1:th_bins
    eul(i,:,:,3)=r';
end

iro=0;itho=0;izo=0;
```

```
T=0;

dVTH=[diff(VTH(:,1)); 0];
dVZ=[diff(VZ(:,1)); 0];
dVR=[diff(VR(:,1)); 0];
dVV=[diff(VV(:,1)); 0];
dTT=[diff(TT(:,1)); 0];

%k_lag=0;
for i_lag=3:Length_TH

    tic

    r_act=R(i_lag,1);
    th_act=TH(i_lag,1);
    z_act=abs(Z(i_lag,1));

    ir=find(r_nodes<=r_act,1,'last');
    ith=round(find(th_nodes<=th_act,1,'last'));
    iz=find(z_nodes<=z_act,1,'last');

    iz(iz>z_bins)=z_bins;
    ir(ir>r_bins)=r_bins;
    ith( ith>M_th_center)=M_th_center;

    Cond_if(i_lag)=max(abs([ir-iro,ith-itho,iz-izo]));

    if Cond_if(i_lag)>4 || Cond_if(i_lag)==0

        ITH= find(th_nodes_1<=mod(th_centers(1,ith),2*pi),1,'last');

        eul(ITH,iz,ir,4)=eul(ITH,iz,ir,4)+VTH(i_lag,1);
        eul(ITH,iz,ir,5)=eul(ITH,iz,ir,5)+VZ(i_lag,1);
        eul(ITH,iz,ir,6)=eul(ITH,iz,ir,6)+VR(i_lag,1);
        eul(ITH,iz,ir,7)=eul(ITH,iz,ir,7)+VV(i_lag,1);
        eul(ITH,iz,ir,8)=eul(ITH,iz,ir,8)+dTT(i_lag,1);
        eul(ITH,iz,ir,9)=eul(ITH,iz,ir,9)+1;

    else

        Cth=(abs(ith-itho))*sign(ith-itho);
        Cz=(abs(iz-izo))*sign(iz-izo);
        Cr=(abs(ir-iro))*sign(ir-iro);

        Lth=round(linspace(0,max(Cth),1+Cond_if(i_lag)));
        Lz=round(linspace(0,max(Cz),1+Cond_if(i_lag)));
        Lr=round(linspace(0,max(Cr),1+Cond_if(i_lag)));

        if ith<itho
            modIndth=flipdim(ith-Lth,2);
            t_rem=num2str(T*(Length_TH/i_lag-1)/3600);
            display([t_rem ' ', num2str(i_lag)]);
        else
            modIndth=flipdim(ith+Lth,2);
        end

        if ir<iro
            modIndr=flipdim((ir-Lr),2);
        else
```

```
            modIndr=flipdim((ir+Lr),2);
        end

        if iz<izo
            modIndz=flipdim((iz-Lz),2);
        else
            modIndz=flipdim((iz+Lz),2);
        end

        LinZation=sqrt(Lth.^2+Lz.^2+Lr.^2)./sqrt((Cth^2+Cr^2+Cz^2));

        LengthLth_1=length(Lth)-1;

        Delta_index=(th_bins*z_bins*r_bins);
        ITH=zeros(LengthLth_1,1); IND4=ITH;
        Lag_=zeros(LengthLth_1,4);
        tmp_index2=2:LengthLth_1+1;

        Br=[ones(2,1), R(i_lag-1:i_lag)];
        Xxr=pinv(Br)*TH(i_lag-1:i_lag,1);     Xxr=flipdim(Xxr,1);
        Bz=[ones(2,1), Z(i_lag-1:i_lag,1)];
        Xxz=pinv(Bz)*R(i_lag-1:i_lag,1,1);     Xxz=flipdim(Xxz,1);
        Bth=[ones(2,1), TH(i_lag-1:i_lag)];
        Xxth=pinv(Bth)*Z(i_lag-1:i_lag,1,1);     Xxth=flipdim(Xxth,1);

        for u=1: LengthLth_1
            Lag_(u,1)=(VTH(i_lag,1)+dVTH(i_lag,1)*LinZation(u+1));
            Lag_(u,2)=(VZ(i_lag,1)+dVZ(i_lag,1)*LinZation(u+1));
            Lag_(u,3)=(VR(i_lag,1)+dVR(i_lag,1)*LinZation(u+1));
            Lag_(u,4)=(VV(i_lag,1)+dVV(i_lag,1)*LinZation(u+1));

            modIndz((modIndz>z_bins))=z_bins;
            modIndr((modIndr>r_bins))=r_bins;
            modIndth((modIndth>M_th_center))=M_th_center;

            TH_CROSS_CELL=polyval(Xxr,r_nodes(modIndr(u:u+1)));
            R_CROSS_CELL=polyval(Xxz,z_nodes(modIndz(u:u+1)));
            Z_CROSS_CELL=polyval(Xxth,th_nodes(modIndth(u:u+1)));


Dist=sqrt(diff(sin(TH_CROSS_CELL).*R_CROSS_CELL)^2+diff(R_CROSS_CELL)^2+dif
f(Z_CROSS_CELL)^2);

            Lag_(u,5)=Dist/Lag_(u,4);
            %   Lag_(u,5)=Lag_(u,4);

            ITH(u)=
find(th_nodes_1<=mod(th_centers(1,fix(modIndth(1,tmp_index2(u))))',2*pi),1,
'last');
            IND4(u) =
sub2ind(size(eul),ITH(u),modIndz(1,tmp_index2(u)),modIndr(1,tmp_index2(u)),
4);


        end

        IND5=  IND4+Delta_index;
        IND6 = IND5+Delta_index;
        IND7 = IND6+Delta_index;
```

```
        IND8 = IND7+Delta_index;
        IND9 = IND8+Delta_index;

        eul(IND4)=eul(IND4)+Lag_(:,1);
        eul(IND5)=eul(IND5)+Lag_(:,2);
        eul(IND6)=eul(IND6)+Lag_(:,3);
        eul(IND7)=eul(IND7)+Lag_(:,4);
        eul(IND8)=eul(IND8)+Lag_(:,5);
        eul(IND9)=eul(IND9)+1;

    end


    t=toc;T=T+t;
    iro=ir;
    itho=ith;
    izo=iz;
end

for i=1:length(eul(:,1,1,1))
    eul(i,:,:,4)=eul(i,:,:,4)./eul(i,:,:,9);
    eul(i,:,:,5)=eul(i,:,:,5)./eul(i,:,:,9);
    eul(i,:,:,6)=eul(i,:,:,6)./eul(i,:,:,9);
    eul(i,:,:,7)=eul(i,:,:,7)./eul(i,:,:,9);
end
```

AI.9. Sher_calc.m

```
function [Gamma]=shear_calc(TO)



Z(:,1)=TO(1,:,1,2)/1000;
TH(:,1)=TO(:,1,1,1);
R(:,1)=TO(1,1,:,3)/1000;
Vth(:,:,:,1)=TO(:,:,:,4);
Vr(:,:,:,1)=TO(:,:,:,5);
Vz(:,:,:,1)=TO(:,:,:,6);
VthR(:,:,:,1)=TO(:,:,:,4).*TO(:,:,:,3)/1000;
R3=TO(:,:,:,3)/1000;

[dUrdZ dUrdTH dUrdR]=gradient(Vr,Z,TH,R); %e13=dUr/dz; e13=dUr/dth;
e13=dUr/dr
[dUzdZ dUzdTH dUzdR]=gradient(Vz,Z,TH,R);
[dUthdZ dUthdTH dUthdR]=gradient(Vth,Z,TH,R); clear dUthdR %#ok<NASGU>
[dUthRdZ dUthRdTH dUthRdR]=gradient(VthR,Z,TH,R);clear dUthRdTH dUthRdZ

e11=dUrdR;                                          %V
e12=0.5*(R3.*dUthRdR+R3.^(-1).*dUrdTH);        %V/V
e13=0.5*(dUzdR+dUrdZ);                       %V/V
e22=R3.^(-1).*dUthdTH+Vr./R3;
e33=dUzdZ;                                   %V
e23=0.5*(dUthdZ+R3.^(-1).*dUzdTH);            %V/V

clear dUrdZ dUrdTH dUrdR dUzdZ dUzdTH dUzdR dUthdZ dUthdTH dUthRdR

Gamma=zeros(size(e11,1),size(e11,2),size(e11,3));
```

```
for i=1:size(e11,1)
    for j=1:size(e11,2)
        for k=1:size(e11,3)
            A=2*[e11(i,j,k) e12(i,j,k) e13(i,j,k);...
                e12(i,j,k) e22(i,j,k) e23(i,j,k);...
                e13(i,j,k) e23(i,j,k) e33(i,j,k)];
            Gamma(i,j,k)=norm(A,'fro');
        end
    end
end
```

APPENDIX II.

Journal Publications

Gabriele, A., F. Spyropoulos and I. T. Norton (2010). "A conceptual model for fluid gel lubrication." Soft Matter **6**(17): 4205-4213.

Gabriele, A., F. Spyropoulos and I. T. Norton (2009). "Kinetic study of fluid gel formation and viscoelastic response with kappa-carrageenan." Food Hydrocolloids **23**(8): 2054-2061.